The Astrophysical Journal, 875:61 (30pp), 2019 April 10 https://doi.org/10.3847/1538-4357/ab0d88

The Close Binary Fraction of Solar-type Stars Is Strongly Anticorrelated with Metallicity

Maxwell Moe[1,3], Kaitlin M. Kratter[1], and Carles Badenes[2]
[1] Steward Observatory, University of Arizona, 933 N. Cherry Ave., Tucson, AZ 85721, USA; moem@email.arizona.edu
[2] Department of Physics and Astronomy and Pittsburgh Particle Physics, Astrophysics and Cosmology Center (PITT PACC), University of Pittsburgh, 3941 O'Hara St., Pittsburgh, PA 15260, USA
Received 2018 July 30; revised 2019 February 8; accepted 2019 March 5; published 2019 April 16

Abstract

There is now strong evidence that the close binary fraction ($P < 10^4$ days; $a < 10$ au) of solar-type stars ($M_1 \approx 0.6$–$1.5\,M_\odot$) decreases significantly with metallicity. Although early surveys showed that the observed spectroscopic binary (SB) fractions in the galactic disk and halo are similar (e.g., Carney–Latham sample), these studies did not correct for incompleteness. In this study, we examine five different surveys and thoroughly account for their underlying selection biases to measure the intrinsic occurrence rate of close solar-type binaries. We reanalyze (1) a volume-limited sample of solar-type stars, (2) the Carney-Latham SB survey of high proper motion stars, (3) various SB samples of metal-poor giants, (4) the APOGEE survey of radial velocity (RV) variables, and (5) eclipsing binaries (EBs) discovered by *Kepler*. The observed APOGEE RV variability fraction and *Kepler* EB fraction both decrease by a factor of ≈4 across $-1.0 < [\mathrm{Fe/H}] < 0.5$ at the 22σ and 9σ confidence levels, respectively. After correcting for incompleteness, all five samples/methods exhibit a quantitatively consistent anticorrelation between the intrinsic close binary fraction ($a < 10$ au) and metallicity: $F_{\mathrm{close}} = 53\% \pm 12\%$, $40\% \pm 6\%$, $24\% \pm 4\%$, and $10\% \pm 3\%$ at $[\mathrm{Fe/H}] = -3.0$, -1.0, -0.2 (mean field metallicity), and $+0.5$, respectively. We present simple fragmentation models that explain why the close binary fraction of solar-type stars strongly decreases with metallicity while the wide binary fraction, close binary fraction of OB stars, and initial mass function are all relatively constant across $-1.5 \lesssim [\mathrm{Fe/H}] < 0.5$. The majority of solar-type stars with $[\mathrm{Fe/H}] \lesssim -1.0$ will interact with a stellar companion, which has profound implications for binary evolution in old and metal-poor environments such as the galactic halo, bulge, thick disk, globular clusters, dwarf galaxies, and high-redshift universe.

Key words: binaries: close – binaries: eclipsing – binaries: spectroscopic – stars: abundances – stars: formation – stars: solar-type

1. Introduction

Variations in the close binary fraction ($a \lesssim 10$ au) with respect to metallicity have been continuously debated over the years (Carney 1983; Latham et al. 2002; Carney et al. 2005; Machida et al. 2009; Raghavan et al. 2010; Rastegaev 2010; Moe & Di Stefano 2013; Bate 2014; Badenes et al. 2018; additional references below). Some observations indicate no dependence on metallicity (Latham et al. 2002; Carney et al. 2005; Moe & Di Stefano 2013), others find that the close binary fraction and metallicity are positively correlated (Carney 1983; Abt & Willmarth 1987; Hettinger et al. 2015), and yet others have found that the close binary fraction decreases with metallicity (Grether & Lineweaver 2007; Raghavan et al. 2010; Gao et al. 2014; Badenes et al. 2018). Studying how the close binary fraction varies with primary mass, metallicity, age, and environment provides significant insight into the processes of protobinary fragmentation, accretion, and orbital migration (Kratter et al. 2008, 2010a; Duchêne & Kraus 2013; Moe & Di Stefano 2017; Moe & Kratter 2018). The close binary fraction is also a crucial input parameter in population synthesis studies of blue stragglers, chemically peculiar stars, cataclysmic variables, SNe Ia and Ib/c, X-ray binaries, mergers of compact objects, short gamma-ray bursts, and sources of gravitational waves (Hurley et al. 2002; Eggleton 2006; Belczynski et al. 2008; Sana et al. 2012; De Marco & Izzard 2017). A substantial change in the close binary fraction with respect to metallicity would have dramatic consequences for the predicted rates and properties of various channels of binary evolution. The apparent discrepancies in the inferred close binary fraction as a function of metallicity must be reconciled in order to more fully understand binary star formation and make reliable predictions for binary evolution.

The primary goal of this study is to reconcile the conflicting results reported in the literature in order to accurately measure the bias-corrected close binary fraction of solar-type stars as a function of metallicity. In Section 2, we overview the methods, results, and potential caveats associated with previous results. In Section 3, we correct for incompleteness within the Carney–Latham sample and other spectroscopic binary (SB) surveys to determine if a large change in the close binary fraction with respect to metallicity is apparent in these earlier data sets. In Section 4, we analyze the Badenes et al. (2018) sample of APOGEE stars to measure precisely how the radial velocity (RV) variability fraction and bias-corrected close binary fraction change as a function of metallicity. We next measure the eclipsing binary (EB) fraction of solar-type dwarfs in the *Kepler* sample, providing a new and independent method for determining how the close binary fraction varies with metallicity (Section 5). We combine and summarize the observational constraints in Section 6, where we show that all five samples/methods investigated in this study exhibit a remarkably consistent anticorrelation between metallicity and close binary fraction. We also discuss the overall binary fraction and period distribution as a function of mass and metallicity and highlight the resulting implications for binary evolution. In Section 7, we investigate fragmentation models to

[3] Einstein Fellow.

explain why the close binary fraction of solar-type stars strongly decreases with metallicity while the wide binary fraction, close binary fraction of massive stars, and initial mass function (IMF) are relatively constant. We conclude in Section 8.

2. Overview of Previous Observations

Carney–Latham sample. For solar-type (FGK) dwarfs, early observations indicated that the SB fraction of metal-poor halo stars was slightly lower than that of metal-rich stars in the galactic disk (Carney 1983; Abt & Willmarth 1987). Subsequent surveys instead found that the SB fraction was relatively independent of metallicity (Stryker et al. 1985; Ryan 1992; Latham et al. 2002; Carney et al. 2005). In particular, Latham et al. (2002) and Carney et al. (2005) investigated a large sample of 1464 FGK stars with high proper motion in the disk and halo. They identified SBs as stars that exhibited larger RV variations compared to their RV measurement uncertainties. They obtained a median of $N_{\rm RV} = 12$ RV measurements per star, so they were able to fit robust orbital parameters for the majority of their SBs. Latham et al. (2002) measured the halo and disk SB fractions to be $14.5\% \pm 1.8\%$ and $15.6\% \pm 1.5\%$, respectively, which are consistent with each other within the uncertainties. They also showed that the observed SB period distributions in the disk and halo are similar (see their Figure 8). Carney et al. (2005) refined the sample by excluding stars with too few RV measurements or large uncertainties in the RVs or metallicities, leaving 994 systems. Carney et al. (2005) measured a slightly larger SB fraction of $24\% \pm 2\%$ for their refined sample but still found that the SB fraction was nearly constant across $-2.5 < [{\rm m/H}] < 0.0$ (see their Figure 2).

However, Latham et al. (2002) and Carney et al. (2005) did not correct for incompleteness. Although the observed SB fraction appears to be independent of metallicity, the true bias-corrected close binary fraction could be substantially different. In fact, to explain the small deficit in the halo SB fraction (14.5%) compared to the disk SB fraction (15.6%), Latham et al. (2002) hinted at the likelihood that their halo measurement was more incomplete. They stated, "This might be the result of an observational bias, because halo binaries have lower metallicity and therefore weaker lines, with a corresponding poorer velocity precision and higher threshold for the detection of binaries." This effect likely explains why the earlier observations by Carney (1983) and Abt & Willmarth (1987) found a smaller SB fraction for metal-poor stars. In Section 3.1, we demonstrate that this selection bias reverses the inferred trends in the Carney–Latham SB samples, and therefore the intrinsic close binary fraction of metal-poor halo stars is actually larger than that of metal-rich disk stars.

Volume-limited samples. Grether & Lineweaver (2007) and Raghavan et al. (2010) provided the earliest statistically significant evidence that the binary fraction of solar-type stars is anticorrelated with metallicity. Raghavan et al. (2010) utilized spectroscopic RV observations, long-baseline and speckle interferometry, adaptive optics, and common proper motion to investigate the multiplicity statistics of 454 FGK dwarfs within 25 pc. In their sample, 411 stars have reliable metallicity measurements across $-0.9 < [{\rm Fe/H}] < 0.4$. As shown in their Figure 19, Raghavan et al. (2010) found that the overall binary fraction decreases from $66\% \pm 7\%$ across $-0.9 < [{\rm Fe/H}] < -0.4$ ($N = 44$ systems) to $39\% \pm 3\%$ across $-0.3 < [{\rm Fe/H}] < 0.4$ ($N = 343$; uncertainties derive from binomial statistics). The overall binary fraction decreases with metallicity by a factor of 1.7 ± 0.2, statistically significant at the 3.8σ level. Although the Raghavan et al. (2010) survey is slightly incomplete (Chini et al. 2014; Moe & Di Stefano 2017), it is difficult to explain how selection biases alone could cause the observed anticorrelation between binary fraction and metallicity.

Close versus wide solar-type binaries. The anticorrelation between metallicity and binary fraction appears to be limited to shorter orbital separations. Of the 44 systems in the Raghavan et al. (2010) sample with $-0.9 < [{\rm Fe/H}] < -0.4$, 22 ($50\% \pm 8\%$) have companions with $\log P({\rm days}) < 6$ ($a \lesssim 200$ au), and seven ($16\% \pm 5\%$) are wide binaries with $\log P({\rm days}) > 6$ ($a \gtrsim 200$ au). Meanwhile, of the 343 systems with $-0.3 < [{\rm Fe/H}] < 0.4$, 87 ($25\% \pm 2\%$) and 47 ($14\% \pm 2\%$) have companions below and above $a \approx 200$ au, respectively. Hence, the very wide binary fraction ($a \gtrsim 200$ au) remains constant within the uncertainties. Common proper motion and CCD imaging surveys also demonstrate that the wide binary fraction of solar-type stars is independent of metallicity (Chanamé & Gould 2004; Zapatero Osorio & Martín 2004). Meanwhile, the binary fraction below $a \lesssim 200$ au in the Raghavan et al. (2010) sample decreases by a factor of 2.0 ± 0.3 between [Fe/H] ≈ -0.6 and 0.0, statistically significant at the 3.2σ level.

Rastegaev (2010) combined spectroscopy, speckle interferometry, and visual observations to measure the full multiplicity properties of metal-poor FGK stars ($[{\rm m/H}] < -1$). After correcting for incompleteness, they measured an overall binary fraction of ≈40%, which is consistent with the binary fraction of $46\% \pm 2\%$ measured by Raghavan et al. (2010) for solar-type stars within 25 pc. Compared to metal-rich systems, however, Rastegaev (2010) showed that metal-poor binaries are significantly skewed toward close to intermediate separations, exhibiting a factor of ≈2–3 excess across $\log P({\rm days}) = 1$–4 ($a \approx 0.1$–10 au; see their Figure 10). Their combined spectroscopic and speckle interferometric survey is relatively complete across this parameter space, so the factor of ≈2–3 excess observed across $a \approx 0.1$–10 au for metal-poor FGK binaries is likely a real effect.

Motivated by the initial preprint of this study, El-Badry & Rix (2019) have since investigated a volume-limited *Gaia* sample of common proper motion binaries in which the metallicities were measured by various spectroscopic surveys. They found that the wide binary fraction ($a \gtrsim 250$ au) of solar-type stars is independent of metallicity, varying by less than $\Delta F_{\rm wide}/F_{\rm wide} < 20\%$ across $-1.0 < [{\rm Fe/H}] < 0.5$. Meanwhile, they showed that an anticorrelation between metallicity and binary fraction begins to emerge below $a \lesssim 200$ au, becoming more significant with decreasing separation. For $a \approx 50$ au, El-Badry & Rix (2019) estimated that the solar-type binary fraction at $[{\rm Fe/H}] = -1.0$ is ≈3 times larger than their metal-rich counterparts with $[{\rm Fe/H}] = 0.5$.

Wide companions to KM subdwarfs. Speckle, *HST*, and adaptive optics imaging of metal-poor KM subdwarfs all indicate a lower wide binary fraction compared to their solar-metallicity counterparts (Riaz et al. 2008; Jao et al. 2009; Lodieu et al. 2009; Ziegler et al. 2015). However, these surveys specifically targeted metal-poor stars based on their photometric colors and absolute magnitudes, i.e., KM subdwarfs in the H-R diagram that lie well below the main-sequence (MS)

relation of solar-metallicity dwarfs. A metal-poor subdwarf with an equally bright companion would appear photometrically as a normal metal-rich dwarf and so would not have been included in their samples. Late K- and M-type binaries are weighted toward equal-mass companions (Dieterich et al. 2012; Janson et al. 2012; Duchêne & Kraus 2013). A bias against equally bright companions would dramatically reduce the inferred binary fraction of metal-poor KM subdwarfs. In their adaptive optics survey of metal-poor KM subdwarfs, Ziegler et al. (2015) specifically noted a substantial shortage of low-contrast companions with $\Delta i < 2$ mag compared to metal-rich KM dwarfs (see their Figure 10). A deficit of binaries with nearly equal brightnesses is naturally explained by their subdwarf photometric selection criteria. These surveys are heavily influenced by this selection bias, and we conclude that there is little or no change in the wide binary fraction of KM stars as a function of metallicity.

Recent wide-field surveys. Over the past few years, there have been several wide-field spectroscopic surveys that measured the chemical abundances and RVs of hundreds of thousands of stars. Some of these spectroscopic surveys obtained multiple epochs of individual stars, allowing for a statistical measurement of the RV variability fraction as a function of metallicity. Utilizing multi-epoch SDSS spectra of F-type dwarfs (resolution $R \approx 2000$), Hettinger et al. (2015) measured the RV variability fraction increases by ≈30% between [Fe/H] = −1.7 and −0.5 (see their Figure 5). Based on SEGUE and LAMOST spectra of FGK dwarfs ($R \approx 2000$), Gao et al. (2014, 2017) and Tian et al. (2018) instead found that the RV variability fraction decreases by a factor of ≈2 between their metal-poor ([Fe/H] < −1.1) and metal-rich ([Fe/H] > −0.6) samples. They also determined that the RV variability fraction increases by a factor of ≈2 between K- and F-type dwarfs, consistent with other studies that show that the close binary fraction strongly increases above $M_1 \gtrsim 1\,M_\odot$ (Abt et al. 1990; Raghavan et al. 2010; Sana et al. 2012; Duchêne & Kraus 2013; Moe & Di Stefano 2017; Murphy et al. 2018). Utilizing SEGUE spectra of extremely metal-poor stars with [Fe/H] $\lesssim -3.0$, Aoki et al. (2015) estimated that the binary fraction below $P < 1000$ days is ≈20%, nearly double that of their metal-rich counterparts.

Most recently, Badenes et al. (2018) analyzed multi-epoch APOGEE spectra of ≈90,000 FGK stars that had a superior spectral resolution, $R \approx 22{,}500$, and higher signal-to-noise ratios, S/N > 40. They searched for RV variables that exhibited large enough amplitudes, $\Delta RV_{max} > 10\,km\,s^{-1}$, between epochs to be nearly 100% certain they were real binary stars. Badenes et al. (2018) demonstrated that the RV variability fraction decreases by a factor of ≈2–3 between their low-metallicity tercile ([Fe/H] $\lesssim -0.3$) and high-metallicity tercile ([Fe/H] $\gtrsim 0.0$). They observed this factor of ≈2–3 metallicity effect for stars of varying surface gravities $0.0 \lesssim \log g(cm\,s^{-2}) \lesssim 5.0$ (see their Figure 13). This suggests that the anticorrelation between binary fraction and metallicity occurs for both close companions orbiting small MS stars and slightly wider companions orbiting large giants. We investigate a subset of the APOGEE data in Section 4 to quantify more precisely how the RV variability fraction and close binary fraction change as a continuous function of metallicity.

Other observational methods corroborate that the binary fraction of FGK stars decreases with metallicity, but to a lesser extent than the factor of ≈2–3 effect determined by Badenes et al. (2018). For example, Yuan et al. (2015) analyzed the properties of binaries discovered through the stellar locus outlier method. These are unresolved binaries in which the companions are bright enough to sufficiently shift the combined photometric colors to be inconsistent with single stars. They found that the unresolved binary fraction decreases by a factor of ≈1.4 between [Fe/H] ≈ −1.7 and −0.3. Similarly, El-Badry et al. (2018) identified double-lined SBs (SB2s) with luminous secondaries in the APOGEE data set. For SB2s that exhibited significant orbital motion between epochs, i.e., $\Delta RV_{max} > 10\,km\,s^{-1}$ as adopted in Badenes et al. (2018), El-Badry et al. (2018) confirmed that the close binary fraction decreases by a factor of ≈1.6 between their low-metallicity tercile ([Fe/H] < −0.2) and high-metallicity tercile ([Fe/H] > 0.0). However, for their larger population of wider SB2s that did not show RV variability, El-Badry et al. (2018) found that the binary fraction was consistent with being constant with respect to metallicity. Taken as a whole, these recent observations suggest that the close binary fraction of solar-type stars is strongly anticorrelated with metallicity, while the wide binary fraction is independent of metallicity. Photometric binaries (Yuan et al. 2015) and SB2s (El-Badry et al. 2018), which include both close and wide binaries, exhibit a weaker trend with metallicity compared to close binaries exclusively.

Close massive binaries. Meanwhile, the close binary fraction of massive stars does not vary significantly with metallicity (Moe & Di Stefano 2013; Dunstall et al. 2015; Almeida et al. 2017). Moe & Di Stefano (2013) measured the EB fraction of early-B stars ($M_1 \approx 6$–$16\,M_\odot$) based on OGLE observations of the Small ([Fe/H] ≈ −0.7) and Large ([Fe/H] ≈ −0.4) Magellanic Clouds (SMC/LMC) and *Hipparcos* observations of nearby systems in the Milky Way (MW; [Fe/H] ≈ 0.0). They found that the fraction of early-B stars that have eclipsing companions across orbital periods $P = 2$–20 days and eclipse depths $\Delta m = 0.25$–0.65 mag is 0.70% ± 0.06%, 0.69% ± 0.03%, and 1.00% ± 0.25% for the SMC, LMC, and MW, respectively (see their Table 1). Although EB observations are less complete due to geometrical selection effects, they are not affected by the spectroscopic selection bias discussed above and are therefore more robust in detecting variations in the close binary fraction with respect to metallicity. Nevertheless, after correcting for incompleteness in their spectroscopic RV observations, the close binary fraction of O stars (Almeida et al. 2017) and early-B stars (Dunstall et al. 2015) in the LMC is consistent with their solar-metallicity counterparts in the MW. For massive stars ($M_1 \gtrsim 6\,M_\odot$), the close binary fraction is relatively independent of metallicity, at least within the $\delta F_{close}/F_{close} \approx 30\%$ measurement uncertainties and across the range of metallicities $-0.7 \lesssim$ [Fe/H] $\lesssim 0.1$ probed by the observations.

IMF. Similarly, the IMF is fairly universal across two orders of magnitude in metallicity, $-1.5 \lesssim$ [Fe/H] $\lesssim 0.5$ (Bastian et al. 2010; Kroupa et al. 2013 and references therein). Young metal-poor associations and clusters in the LMC ([Fe/H] ≈ −0.4; Da Rio et al. 2009), SMC ([Fe/H] ≈ −0.7; Sirianni et al. 2002; Schmalzl et al. 2008), and outer regions of the MW ([Fe/H] ≈ −0.8; Yasui et al. 2016a, 2016b) all have IMFs consistent with the canonical IMF. The low-mass end of the IMF ($M_1 \approx 0.1$–$0.9\,M_\odot$) is invariant across galactic open clusters and globular clusters that span a wide range of metallicities, $-2.3 \lesssim$ [Fe/H] $\lesssim 0.3$ (von Hippel et al. 1996; Bastian et al. 2010; De Marchi et al. 2010). Although some

observations indicate that the IMF becomes top-heavy toward lower metallicities (Marks et al. 2012; Geha et al. 2013; Kroupa et al. 2013), this trend is not statistically significant until the metallicity falls below at least [Fe/H] $\lesssim -1.5$.

3. Spectroscopic versus Intrinsic Close Binary Fraction

3.1. Carney–Latham Sample

3.1.1. Description of Observations

Of the 1464 stars with high proper motion in the Carney–Latham sample, Latham et al. (2002) cataloged detailed information for 1359 single-lined stars. They listed the stellar properties, e.g., metallicity [m/H], effective temperature $T_{\rm eff}$, and rotational velocity $v_{\rm rot}$, of the template spectrum that most closely matched the observed spectra. The full temperature range is $T_{\rm eff} \approx 3800$–7700 K, but 1301 of the systems (96%) have $T_{\rm eff} \approx 4500$–6300 K, corresponding approximately to F7–K4 spectral types. The template spectra are in large metallicity increments of Δ[m/H] = 0.5, but 1349 of their 1359 single-lined stars span a large range of $-3.0 \leqslant$ [m/H] $\leqslant 0.5$ to provide sufficient leverage for investigating metallicity effects. Latham et al. (2002) derived robust orbital solutions for 156 SB1s (all with $P < 7000$ days) and presented preliminary orbits for an additional 15 SB1s (mostly with $P = 5000$–$10{,}000$ days). They also cataloged 17 large-amplitude RV variables that likely have wide stellar companions but lack the necessary phase coverage to measure orbital elements (see their Figure 6). In a separate study, Goldberg et al. (2002) measured stellar parameters and orbital solutions for 34 SB2s from the Carney–Latham sample, all of which have $P < 5000$ days and $-2.5 \leqslant$ [m/H] $\leqslant 0.0$. Neither Latham et al. (2002) nor Goldberg et al. (2002) fitted the surface gravities $\log g$ directly; they instead adopted $\log g = 4.5$ for cooler stars ($T_{\rm eff} \lesssim 6000$ K) and $\log g = 4.0$ for hotter stars ($T_{\rm eff} \gtrsim 6000$ K). About 10% of the high proper motion stars in the Carney–Latham sample are likely subgiants or giants (Laird et al. 1988; Carney et al. 1994), and the fraction is probably larger for systematically older halo stars.

Latham et al. (2002) listed the Julian dates, RVs, and RV uncertainties $\sigma_{\rm RV}$ for each of the $N_{\rm RV}$ observations of each single-lined star. We compile their data and compute the mean RV uncertainty $\langle\sigma_{\rm RV}\rangle$ for each system. In Figure 1, we show the average of and 1σ spread in $\langle\sigma_{\rm RV}\rangle$ as a function of metallicity [m/H]. As indicated in Latham et al. (2002), the metal-poor stars in their sample have systematically larger RV uncertainties due to their weaker absorption lines. The mean uncertainties double from $\langle\sigma_{\rm RV}\rangle = 0.5$ km s^{-1} for solar metallicity to $\langle\sigma_{\rm RV}\rangle = 1.0$ km s^{-1} for metal-poor stars with [m/H] $\leqslant -2.0$.

Latham et al. (2002) observed their single-lined stars with varying cadence (see their Figure 3). For their full sample, the median number of RV measurements is $N_{\rm RV} = 12$, and the 10th–90th percentile range spans $N_{\rm RV} = 8$–39. Similarly, the median time span is $\Delta t = 9$ yr between the first and final visits, and the 10th–90th percentile interval is $\Delta t = 8$–14 yr. There is no trend in the number or time span of RV measurements as a function of metallicity. The median number of RV observations is $N_{\rm RV} = 13$ for the 544 metal-poor single-lined stars with $-3.0 \leqslant$ [m/H] $\leqslant -0.8$ and $N_{\rm RV} = 11$ for the 805 metal-rich stars with $-0.8 <$ [m/H] $\leqslant 0.5$. The median time span, which is the most important parameter for estimating completeness rates (see below and Section 4), is $\Delta t = 9$ yr for both the metal-poor and metal-rich subsamples.

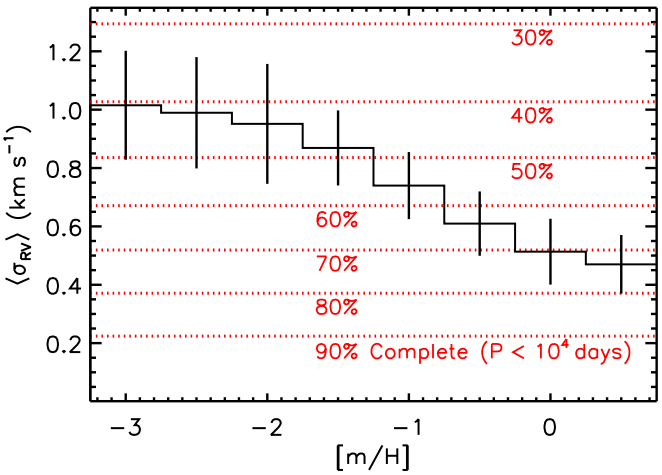

Figure 1. Mean RV uncertainty $\langle\sigma_{\rm RV}\rangle$ as a function of metallicity [m/H] in the Latham et al. (2002) sample (black). We simulate the completeness rates for a population of binaries with $P < 10^4$ days (dotted red). As the RV uncertainties decrease from $\langle\sigma_{\rm RV}\rangle = 1.0$ to 0.5 km s^{-1} between metal-poor and metal-rich stars, the completeness fractions increase from ≈40% to ≈70%.

3.1.2. Corrections for Incompleteness

We next perform Monte Carlo simulations to determine the probability of detecting SBs as a function of $\langle\sigma_{\rm RV}\rangle$. In our simulations, we fix the mass of the primary to be $M_1 = 1.0\,M_\odot$ and draw period, mass-ratio, and eccentricity distributions consistent with solar-type binaries in the field (Duquennoy & Mayor 1991; Raghavan et al. 2010; Tokovinin 2014; Moe & Di Stefano 2017). Specifically, we adopt a lognormal period distribution with a peak at $\log P$(days) = 4.9 and dispersion of $\sigma_{\log P} = 2.3$, but only generate binaries within the short-period tail across the interval of $0.0 <$ log P (days) < 4.0 ($a \lesssim 10$ au) that we are investigating. We assume a uniform mass-ratio distribution across $q = M_2/M_1 = 0.1$–1.0 and that very close binaries with $P < P_{\rm circ} = 10$ days are tidally circularized. Toward longer periods, $P > P_{\rm circ}$, we adopt a uniform eccentricity distribution across the interval, $0.0 < e < e_{\rm max}(P)$, where the upper envelope of the eccentricity-versus-period distribution derives from conservation of orbital angular momentum during tidal evolution (Badenes et al. 2018):

$$e_{\rm max} = \left(1 - \left(\frac{P}{P_{\rm circ}}\right)^{-2/3}\right)^{1/2}. \quad (1)$$

We assume random orientations, which have an inclination probability distribution of $p = \sin i$ and a uniform distribution for arguments of periastron. Reasonable variations in the period, mass-ratio, or eccentricity distributions yield only minor changes in the simulated detection efficiencies.

For each binary, we generate RVs at $N_{\rm RV} = 12$ epochs randomly distributed across a time span of $\Delta t = 9$ yr, matching the median cadence and baseline of the Latham et al. (2002) observations. For each RV measurement, we add Gaussian random noise according to $\langle\sigma_{\rm RV}\rangle$. A large-amplitude RV variable will exhibit a larger variance of RVs compared to the variance implied by its measurement uncertainties. We therefore use an F-variance test to measure the probability p

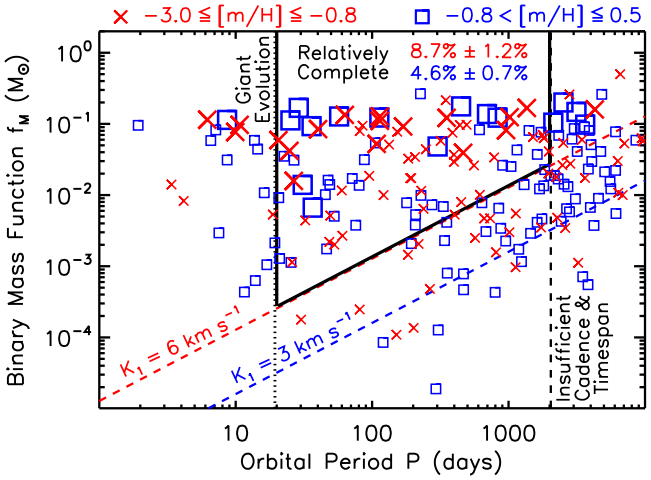

Figure 2. Measured binary mass functions and orbital periods for the 169 SB1s with $P < 10^4$ days from Latham et al. (2002; smaller symbols) and 34 SB2s from Goldberg et al. (2002; larger symbols) divided into metal-poor ($-3.0 \leqslant$ [m/H] $\leqslant -0.8$; red crosses) and metal-rich ($-0.8 <$ [m/H] $\leqslant 0.5$; blue squares) subsets. The samples are biased against very close binaries with $P < 20$ days (left of dotted black line) due to contamination by subgiants and giants, while wide binaries beyond $P > 2000$ days (right of dashed black line) are incomplete given the median number $N_{\rm RV} = 12$ and time span $\Delta t = 9$ yr of the RV observations. The SBs with small velocity semi-amplitudes $K_1 < 6$ $\langle\sigma_{\rm RV}\rangle$ are also incomplete, corresponding to $K_1 < 3$ km s^{-1} for metal-rich systems (dashed blue) and $K_1 < 6$ km s^{-1} for metal-poor systems (dashed red). Within the relatively complete and unbiased parameter space (solid black lines), the SB fraction decreases by a factor of 1.9 ± 0.4 from $8.7\% \pm 1.2\%$ for the metal-poor subsample to $4.6\% \pm 0.7\%$ for the metal-rich subsample at the 3.0σ significance level.

that each generated system has a constant RV. In the Latham et al. (2002) catalog, the majority of constant RV stars have $p > 5 \times 10^{-7}$, while nearly all systems with $p < 5 \times 10^{-7}$ are cataloged as SBs, the majority of which have measured orbital parameters. We adopt the criterion that $p < 5 \times 10^{-7}$ for a simulated binary to be considered an RV variable, corresponding to a 5.0σ level of significance.

We show the results of our Monte Carlo simulations in Figure 1. Given a small RV uncertainty of $\langle\sigma_{\rm RV}\rangle = 0.2$ km s^{-1}, ≈90% of the binaries with $P < 10^4$ days would appear as spectroscopic RV variables with $p < 5 \times 10^{-7}$. The remaining ≈10% of the binaries are generally in wide orbits ($P \approx$ 5000–10,000 days) with low-mass companions ($q \approx$ 0.1–0.3). Meanwhile, given a mean uncertainty of $\langle\sigma_{\rm RV}\rangle = 1.3$ km s^{-1} and 12 random epochs across 9 yr, only ≈30% of binaries with $P < 10^4$ days would appear as RV variables. Across the interval of interest, the completeness rate increases from ≈40% for metal-poor halo stars ([m/H] $\leqslant -2.0$; $\langle\sigma_{\rm RV}\rangle \approx 1.0$ km s^{-1}) to ≈70% for metal-rich disk stars ([m/H] $\geqslant$ 0.0; $\langle\sigma_{\rm RV}\rangle \approx 0.5$ km s^{-1}). The Latham et al. (2002) spectroscopic survey is ≈1.8 times more complete in detecting close binary companions to metal-rich disk stars compared to metal-poor halo stars.

3.1.3. Binary Mass Functions

The observed distribution of binary mass functions $f_{\rm M} = (M_2 \sin i)^3/(M_1 + M_2)^2 = P K_1^3 (1 - e^2)^{3/2}/(2\pi G)$ also demonstrates that metal-poor SBs are less complete. In Figure 2, we show the measured binary mass functions versus orbital periods for the 169 SB1s with $P < 10^4$ days in the Latham et al. (2002) sample. We also display with slightly larger symbols the 34 SB2s from Goldberg et al. (2002), which concentrate toward larger binary mass functions $f_{\rm M} = 0.007$–$0.2\,M_\odot$, as expected. We divide the sample into a metal-poor subset with $-3.0 \leqslant$ [m/H] $\leqslant -0.8$ (red crosses; $N_{\rm SB} = 91$ SBs with measured orbital elements; $N = 562$ stars) and a metal-rich subset with $-0.8 <$ [m/H] $\leqslant 0.5$ (blue squares; $N_{\rm SB} = 114$, $N = 821$). Both subsamples are measurably incomplete toward wide separations and small mass ratios. However, the metal-rich SB1s, which have systematically smaller RV uncertainties, extend toward smaller binary mass functions and longer orbital periods. A two-sample Kolmogorov–Smirnov (K-S) test demonstrates that the observed 71 SBs with $P > 100$ days in our metal-rich subset are weighted toward smaller velocity semi-amplitudes compared to the 57 metal-poor SBs with $P > 100$ days at the 2.7σ confidence level ($p_{\rm K\text{-}S} = 0.004$). A two-sample Anderson–Darling (AD) test is slightly more stringent, yielding a 3.0σ discrepancy. For reference, we also show $f_{\rm M}$ as a function of P for a fixed eccentricity of $e = 0.5$ and a velocity semi-amplitude of $K_1 = 6$ $\langle\sigma_{\rm RV}\rangle$, corresponding to $K_1 = 3$ km s^{-1} for metal-rich stars (dashed blue line in Figure 2) and $K_1 = 6$ km s^{-1} for metal-poor stars (dashed red line). The Latham et al. (2002) SB1 sample is measurably incomplete below these relations.

The samples of SB1s and SB2s with measured orbital solutions are relatively complete across $P =$ 20–2000 days and above binary mass functions $f_{\rm M}$ corresponding to $K_1 = 6$ km s^{-1} and $e = 0.5$. We display this relatively complete parameter space with solid black lines in Figure 2. Enclosed within this area, the SB fraction is $49/554 = 8.7\% \pm 1.2\%$ for our metal-poor subsample ($-3.0 \leqslant$ [m/H] $\leqslant -0.8$). Meanwhile, the SB fraction within the same region of P and $f_{\rm M}$ is only $38/821 = 4.6\% \pm 0.7\%$ for our metal-rich subsample ($-0.8 <$ [m/H] $\leqslant 0.5$). By focusing on this relatively complete parameter space, we demonstrate that the close binary fraction decreases by a factor of 1.9 ± 0.4 at the 3.0σ significance level between our metal-poor and metal-rich subsamples.

The sample of SBs with measured orbital solutions is incomplete beyond $P > 2000$ days (right of black dashed line in Figure 2). The handful of systems in this part of the parameter space required substantially more RV measurements and longer time spans to fit the orbits. For example, the median number and time span of RV measurements for the 15 long-period SB1s with preliminary orbits are $N_{\rm RV} = 57$ and $\Delta t = 18$ yr, respectively, which are considerably larger than the median values of $N_{\rm RV} = 12$ and $\Delta t = 9$ yr for the Latham et al. (2002) sample as a whole. In addition, the 17 SB1s without orbital solutions in the Latham et al. (2002) catalog likely have $P > 2000$ days but simply lack the number of observations and/or time span to fit the RVs (see their Figure 6).

The Carney–Latham SB sample is also slightly biased against very close binaries with $P < 20$ days due to contamination by subgiants and giants. As stars in very close binaries expand beyond the MS, they undergo Roche-lobe overflow, thereby preventing evolution toward the giant stage. Badenes et al. (2018) thoroughly discussed this effect of giant evolution truncating the short-period tail of the binary period distribution as a function of giant surface gravity, an indicator of radius. In volume-limited samples of solar-type dwarfs, the very close binary fraction below $P < 20$ days is $4\% \pm 1\%$ (Duquennoy & Mayor 1991; Raghavan et al. 2010; Tokovinin 2014; Moe & Di Stefano 2017). In our metal-rich subsample with

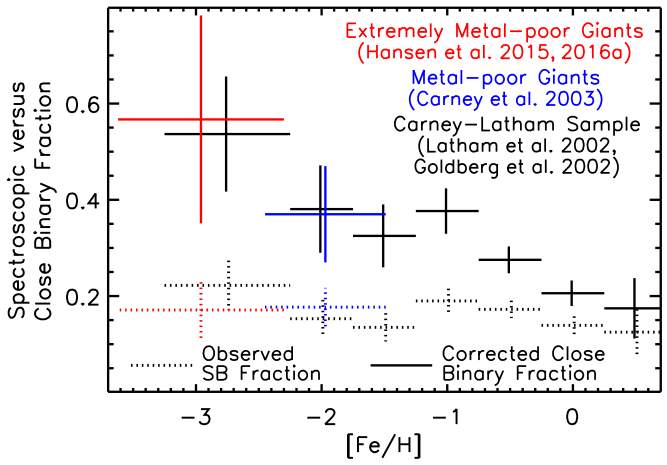

Figure 3. As a function of metallicity, the observed SB fraction (dotted) vs. the intrinsic close binary fraction ($P < 10^4$ days; $a \lesssim 10$ au) after correcting for incompleteness and the removal of very close binaries due to giant evolution (solid). We compare the samples of extremely metal-poor giants (red; Hansen et al. 2015, 2016a), metal-poor giants (blue; Carney et al. 2003), and solar-type stars (mostly dwarfs) with high proper motion in the Carney–Latham survey (black; Goldberg et al. 2002; Latham et al. 2002). Although the observed SB fraction of ≈15%–20% is relatively independent of metallicity, the true bias-corrected close binary fraction decreases from $F_{\rm close} \approx 35\%$–$55\%$ across $-3.5 < [{\rm Fe/H}] < -1.0$ to $F_{\rm close} \approx 20\%$ at $[{\rm Fe/H}] = 0.0$.

$-0.8 < [{\rm m/H}] \leqslant 0.5$, however, the observed very close binary fraction is only $13/821 = 1.6\% \pm 0.4\%$ (see systems left of the dotted black line in Figure 2). The very close binary fraction in our metal-poor subsample with $-3.0 \leqslant [{\rm m/H}] \leqslant -0.8$ is lower still at $6/562 = 1.1\% \pm 0.4\%$, likely due to a larger contamination by giants for systematically older halo stars. We estimate that the close binary fraction should increase by 1% and 2% for our metal-rich and metal-poor subsamples, respectively, in order to correct for this selection bias.

3.1.4. Intrinsic Close Binary Fraction

In Figure 3, we show the observed SB fraction as a function of metallicity for the combined Latham et al. (2002) and Goldberg et al. (2002) samples (dotted black data points). The observations are consistent with a constant ≈15%–20% SB fraction across the full metallicity range $-3.0 \leqslant [{\rm m/H}] \leqslant 0.5$, as reported in Latham et al. (2002) and Carney et al. (2005). We correct the observed distribution according to our simulated completeness rates displayed in Figure 1. For example, the observed SB fraction for $[{\rm m/H}] = 0.0$ is $14\% \pm 2\%$. For this metallicity, we estimate that ≈70% of binaries with $P < 10^4$ days are detectable as SBs (Figure 1), implying a corrected close binary fraction of $(0.14 \pm 0.02)/0.70 = 20\% \pm 3\%$. We add the 1% of very close metal-rich binaries ($P < 20$ days) that were excluded due to contamination by subgiants and giants, resulting in our final value of $F_{\rm close} = 21\% \pm 3\%$ for $[{\rm m/H}] = 0.0$. We repeat this procedure for each of the metallicity intervals but add 2% to the close binary fraction of metal-poor stars ($[{\rm m/H}] \leqslant -1$) to account for the increased contamination by evolved giants in the older metal-poor populations.

We display in Figure 3 our bias-corrected close binary fraction as a function of metallicity based on the Carney–Latham sample (solid black). The corrected close binary fraction decreases by a factor of $3.2^{+1.9}_{-0.9}$ from $F_{\rm close} = 54\% \pm 12\%$ at $[{\rm m/H}] \approx -2.7$ to $F_{\rm close} = 17\% \pm 6\%$ at $[{\rm m/H}] \approx 0.5$. Attempting to fit a constant close binary fraction to the seven black data points in Figure 3 results in a reduced $\chi^2/\nu = 3.5$ with $\nu = 6$ degrees of freedom. The probability of exceeding this value is $p = 0.0016$, i.e., the bias-corrected close binary fraction decreases with metallicity at the 3.0σ significance level. This is identical to the level of significance determined by comparing the metal-poor and metal-rich SB fractions across the parameter space in Figure 2 that was relatively complete.

Focusing on a narrower metallicity interval, the close binary fraction decreases by a factor of $2.2^{+1.2}_{-0.6}$ between $[{\rm m/H}] = -1.0$ and $+0.5$ in Figure 3. A factor of ≈2–4 decrease in the close binary fraction across this metallicity interval, as indicated in Badenes et al. (2018) and measured by us in Section 4, is fully consistent with the Carney–Latham observations. We conclude that once corrections for incompleteness and selection biases are considered, the Carney–Latham sample is not only consistent with a large anticorrelation between metallicity and the close binary fraction but actually supports such a trend at the 3.0σ significance level.

3.2. Metal-poor Giants

The SB fractions of metal-poor giants (Carney et al. 2003) and extremely metal-poor giants enriched with *r*-process elements or carbon (Hansen et al. 2015, 2016a) are ≈15%–20%. These values are consistent with the observed SB fractions of metal-poor dwarfs in the halo (Latham et al. 2002; Carney et al. 2005). We reemphasize that the observed SB fractions are lower limits to the true close binary fractions, especially for metal-poor stars that have weaker absorption lines. In the following, we account for incompleteness within these additional samples of metal-poor stars in order to compute their intrinsic close binary fractions.

3.2.1. Carney et al. (2003) Sample

Carney et al. (2003) obtained a median of $N_{\rm RV} = 13$ RV measurements of 91 metal-poor field giants with an average precision of $\langle \sigma_{\rm RV} \rangle = 0.65\,{\rm km\,s^{-1}}$ and a median time span of $\Delta t = 13.8$ yr. This is similar in frequency but has improved sensitivity and duration compared to the Latham et al. (2002) survey of metal-poor dwarfs in the halo. The metallicities of the giants span $-4.0 < [{\rm Fe/H}] < -0.9$, resulting in a mean and 1σ spread of $[{\rm Fe/H}] = -2.0 \pm 0.5$. These metal-poor giants are some of the oldest stars in the galaxy and therefore have masses $M_1 \approx 0.8$–$1.1\,M_\odot$ corresponding to MS-turnoff ages of $\tau \approx 7$–13 Gyr. Carney et al. (2003) identified 16 SB1s in their sample and measured robust orbital periods spanning $P \approx 40$–5200 days for 14 of them. As shown in Figure 3, the observed SB fraction is $16/91 = 18\% \pm 4\%$.

The most luminous giants in the Carney et al. (2003) sample exhibit significant RV jitter due to radial pulsations, convective instabilities in the tenuous upper layers, or intermittent star spots modulated by rotation. They found that ≈40% of giants with absolute magnitudes $M_{\rm V} < -1.4$ display detectable RV jitter $\sigma_{\rm RV,jitter} \gtrsim 1\,{\rm km\,s^{-1}}$. Hekker et al. (2008) later showed that nonperiodic RV jitter occurs in smaller, less luminous giants, but the magnitude simply increases from $\sigma_{\rm RV,jitter} = 0.03\,{\rm km\,s^{-1}}$ at $\log g \approx 3.0$ to $\sigma_{\rm RV,jitter} = 0.3\,{\rm km\,s^{-1}}$ at $\log g \approx 1.5$. Stochastic variations in the RVs due to intrinsic fluctuations in the atmospheres inhibit the detection of SBs with small velocity semi-amplitudes. We therefore remove the nine giants in the

Carney et al. (2003) sample that exhibit significant RV jitter (dark systems in their Figure 8). One of these objects, HD 218732, is also an SB in which the velocity semi-amplitude $K_1 = 2.9\,\mathrm{km\,s^{-1}}$ induced by the companion is larger than the RV jitter $\sigma_{\mathrm{RV,jitter}} \approx 1\,\mathrm{km\,s^{-1}}$. The observed SB fraction for our refined subsample remains unchanged at $15/82 = 18\% \pm 4\%$.

The metal-poor giants in the Carney et al. (2003) sample also span a broad range of radii, $R_1 = 4.3$–$112\,R_\odot$, providing a mean of $\langle R_1 \rangle = 23\,R_\odot$. Adopting the typical parameters $M_1 \approx 1.0\,M_\odot$ and $q = 0.5$, the very close binaries with $P \lesssim 35$ days would have already filled their Roche lobes by the time the primaries evolved to $R_1 = 23\,R_\odot$ (Eggleton 1983). The Carney et al. (2003) sample is therefore significantly biased against very close binaries with $P \lesssim 35$ days. Their closet binary, i.e., BD +13°3683 with $P \approx 40$ days, happens to contain the smallest giant ($R_1 = 4.3\,R_\odot$) in their sample. We correct for incompleteness and this selection bias using two different methods described below.

First, we perform a Monte Carlo simulation, as done in Section 3.1.2, to measure the completeness rate but adopt $N_{\mathrm{RV}} = 13$, $\Delta t = 13.8$ yr, and $\langle \sigma_{\mathrm{RV}} \rangle = 0.65\,\mathrm{km\,s^{-1}}$ to match the median cadence and sensitivity of the Carney et al. (2003) observations. We increase the circularization period to $P_{\mathrm{circ}} = 100$ days in Equation (1) to account for the larger tidal radius of the giants. We also generate close binaries across the interval $P = 35$–10^4 days because very close binaries with $P < 35$ days have effectively been removed from the Carney et al. (2003) sample of giants. Of all the metal-poor giants with companions across $P = 35$–10^4 days, we calculate that 55% would have been detected as SBs by Carney et al. (2003) at the $>5\sigma$ significance level. This is slightly lower than the completeness rate of 62% for $\langle \sigma_{\mathrm{RV}} \rangle = 0.65\,\mathrm{km\,s^{-1}}$ inferred from Figure 1. Despite the increased time span of the Carney et al. (2003) observations, the removal of very close binaries with $P < 35$ days, which are easier to detect, causes the overall completeness rate to decrease. The details of tidal circularization during the giant phase have a negligible effect on our corrections for incompleteness; we repeat our Monte Carlo simulation with $P_{\mathrm{circ}} = 20$ and 500 days and calculate completeness rates of 54% and 56%, respectively. The corrected binary fraction of metal-poor giants in the Carney et al. (2003) sample is $(0.18 \pm 0.04)/0.55 = 33\% \pm 7\%$ across $P = 35$–10^4 days. According to our adopted lognormal period distribution for solar-type binaries, 17% of close binaries with $\log P(\mathrm{days}) = 0$–4 have very short periods, $P = 1$–35 days. The close binary fraction ($\log P = 0$–4; $a \lesssim 10$ au) of metal-poor dwarfs is therefore $F_{\mathrm{close}} = (0.33 \pm 0.07)/0.83 = 40\% \pm 8\%$ after accounting for the bias against very close binaries in giant systems.

Second, we examine in Figure 4 the binary mass functions and periods of the 13 SBs with measured orbital elements and no significant RV jitter in Carney et al. (2003), similar to our analysis of the Carney–Latham SBs (see Figure 2). We also show in Figure 4 a random subset of 1000 binaries spanning $P = 35$–10^4 days from our Monte Carlo simulation with $P_{\mathrm{circ}} = 100$ days, indicating those that were detectable above the $>5\sigma$ level with darker, thicker symbols. The observed density of SBs in the P-versus-f_M parameter space follows our simulated detections quite well. Our analysis confirms that the Carney et al. (2003) SB survey is incomplete toward long periods and small binary mass functions. In our Monte Carlo model, 37% of binaries have $P = 35$–3000 days and binary

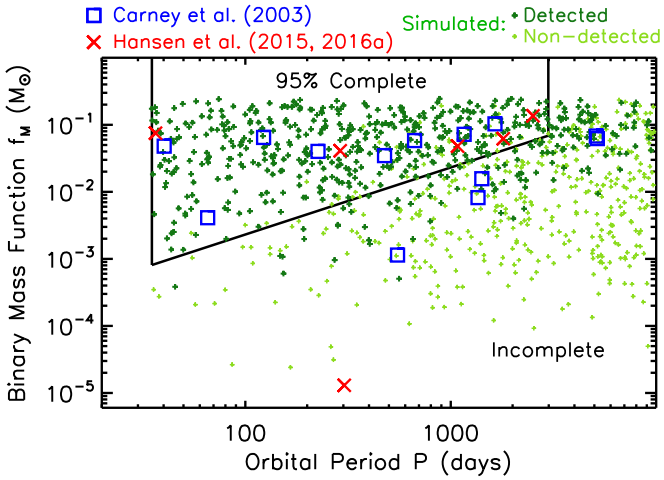

Figure 4. Similar to Figure 2 but for the 13 SBs with orbital solutions and no significant RV jitter in the Carney et al. (2003) sample of metal-poor giants (blue squares) and six SBs with orbital solutions in the Hansen et al. (2015, 2016a) samples of extremely metal-poor giants chemically enriched with r-process elements or carbon (red crosses). We also display a random subset of 1000 binaries from our Monte Carlo simulations (green plus signs) that match the cadence and sensitivity of the Carney et al. (2003) observations. The simulated binaries that exhibit RV variability above a $>5\sigma$ significance level are indicated with darker, larger symbols. The observations are ≈95% complete across $P = 35$–3000 days and above binary mass functions f_{M} corresponding to $K_1 = 7\,\mathrm{km\,s^{-1}}$ and $e = 0.5$ (black lines).

mass functions f_M greater than that corresponding to $K_1 = 7\,\mathrm{km\,s^{-1}}$ and $e = 0.5$. We indicate this parameter space, which is ≈95% complete, in Figure 4. We find that eight of the SBs from the Carney et al. (2003) sample are located within this relatively complete region, indicating a corrected binary fraction of $8/82/0.37/0.95 = 28\% \pm 10\%$. After accounting for the bias against very close binaries with $P < 35$ days, the close binary fraction of metal-poor dwarfs is $F_{\mathrm{close}} = (0.28 \pm 0.10)/0.83 = 34\% \pm 12\%$.

The bias-corrected close binary fraction determined from our forward-modeling method ($F_{\mathrm{close}} = 40\% \pm 8\%$) is consistent with our inversion technique ($F_{\mathrm{close}} = 34\% \pm 12\%$). We adopt an average of $F_{\mathrm{close}} = 37\% \pm 10\%$ and present the result in Figure 3. The bias-corrected close binary fraction measured for the Carney et al. (2003) sample of metal-poor giants matches the close binary fraction determined for metal-poor halo stars with high proper motion in the Carney–Latham sample.

3.2.2. Hansen et al. (2015, 2016a) Samples

We next combine the samples of extremely metal-poor giants enriched with r-process elements (Hansen et al. 2015) and carbon (Hansen et al. 2016a). We do not include extremely metal-poor giants enriched with s-process elements, e.g., barium, which exhibit a very large SB fraction of ≈80% and are clearly the result of post-MS binary mass transfer (Jorissen et al. 1998; Lucatello et al. 2005; Hansen et al. 2016b). Hansen et al. (2015, 2016a) concluded that the abundances of extremely metal-poor giants enriched with r-process elements and carbon are primordial; i.e., the enhanced elements were imprinted on their natal molecular clouds. Our combined sample contains 41 extremely metal-poor giants that span $-5.8 < [\mathrm{Fe/H}] < -1.6$, providing a mean and 1σ spread of $[\mathrm{Fe/H}] = -3.0 \pm 0.7$. Within this sample, Hansen et al. (2015, 2016a) found seven SBs, six of which have orbital

solutions. We display the observed SB fraction of $7/41 = 17\% \pm 6\%$ in Figure 3.

Hansen et al. (2015, 2016a) observed their 41 targets with varying cadence. In particular, 11 of their extremely metal-poor giants were observed only $N_{\rm RV} = 2$–7 times. For comparison, both Latham et al. (2002) and Carney et al. (2003) obtained at least $N_{\rm RV} \geqslant 7$ measurements for each of their targets, ≈90% of which were observed $N_{\rm RV} \geqslant 9$ times. A small number of RV measurements reduces the probability of detecting RV variability and makes it nearly impossible to fit robust orbital solutions. We therefore remove the 11 objects with $N_{\rm RV} = 2$–7, none of which were identified as SBs, leaving 30 extremely metal-poor giants in our culled sample.

The mean RV precision of the extremely metal-poor giants in the Hansen et al. (2015, 2016a) samples ranged significantly from $\langle\sigma_{\rm RV}\rangle = 0.012$ to 2.5 km s^{-1}. With such a large variance in $\langle\sigma_{\rm RV}\rangle$, a Monte Carlo simulation with a single value of $\langle\sigma_{\rm RV}\rangle$ is no longer valid. We instead rely on the measured binary mass functions f_M and periods P of the six SBs with orbital solutions, which are displayed in Figure 4. One of the SBs, HE 15230901, has an extremely small binary mass function of $f_{\rm M} = 1.3 \times 10^{-5}\,M_\odot$ (Hansen et al. 2015). This object was observed with superior precision $\langle\sigma_{\rm RV}\rangle = 0.016$ km s^{-1} and more times ($N_{\rm RV} = 34$) than any other targets in the Hansen et al. (2015, 2016a) samples. If the other targets were SBs with such small binary mass functions, they would not be detected.

Meanwhile, the other five SBs with orbital solutions in the Hansen et al. (2015, 2016a) survey extend across the upper middle region in Figure 4, spanning $f_{\rm M} \approx 0.04$–$0.14\,M_\odot$ and $P \approx 37$–2500 days. The fact that five of the 30 extremely metal-poor giants with $N_{\rm RV} \geqslant 8$ are SBs with such large binary mass functions strongly suggests that the intrinsic close binary fraction is particularly large. These five SBs occupy the same parameter space that is ≈95% complete according to our Monte Carlo model that simulates the cadence and sensitivity of the Carney et al. (2003) observations. Although the Hansen et al. (2015, 2016a) surveys had variable precision, we also expect this parameter space to be ≈95% complete. We therefore use the same inversion technique to correct for incompleteness, resulting in an intrinsic binary fraction of $5/30/0.37/0.95 = 47\% \pm 19\%$ across $P = 35$–10^4 days. After accounting for the bias against very close binaries with $P < 35$ days, the primordial close binary fraction of extremely metal-poor dwarfs is $F_{\rm close} = (0.47 \pm 0.19)/0.83 = 57\% \pm 22\%$. We display our result in Figure 3, which is consistent with our measurement of $F_{\rm close} = 54\% \pm 12\%$ for extremely metal-poor stars with $[{\rm m/H}] = -2.7 \pm 0.7$ selected from the Carney–Latham sample. The close binary fraction of metal-poor dwarfs, metal-poor giants, and extremely metal-poor giants are all $F_{\rm close} \approx 35\%$–55%, substantially larger than the close binary fraction $F_{\rm close} \approx 20\%$ of solar-metallicity FGK dwarfs in the disk.

4. APOGEE RV Variables

4.1. Sample Selection and Description

The SDSS-IV/APOGEE near-infrared spectroscopic survey (data release 13) measured the effective temperatures, surface gravities, metallicities, and RVs of ≈164,000 stars in various environments, including the galactic disk, bulge, and halo (Zasowski et al. 2013; Holtzman et al. 2015; Nidever et al. 2015; Albareti et al. 2017). After calibrating their observations

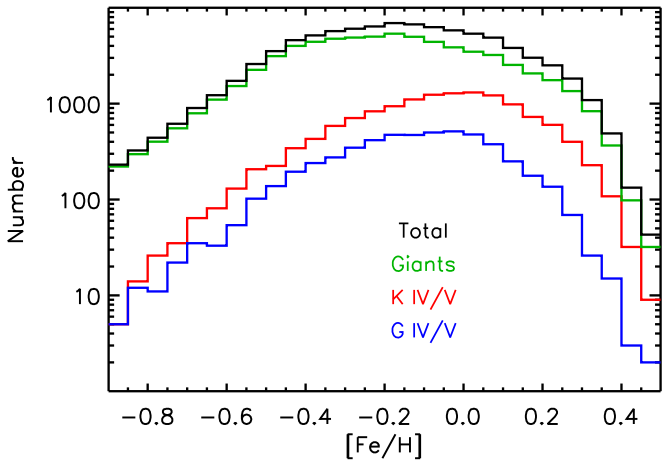

Figure 5. Metallicity distribution of APOGEE stars in our selected total sample (black) and the giant (green), K IV/V (red), and G IV/V (blue) subsamples.

to both synthetic spectra and empirical relations, APOGEE measured the stellar parameters to high precision, e.g., $\delta T_{\rm eff} \approx 90$ K, $\delta \log g \approx 0.11$ dex, and $\delta[{\rm Fe/H}] \approx 0.15$ dex (Holtzman et al. 2015). In their study, Badenes et al. (2018) removed targets in open clusters and stars with effective temperatures or surface gravities that were inadequately measured, leaving 122,141 objects. They then examined the spectra and RV measurements for each star, keeping only the individual visits with spectral S/N > 40. A total of 91,246 stars with $N_{\rm RV} \geqslant 2$ high-quality RV measurements (78% of which have $N_{\rm RV} \geqslant 3$ epochs) were included in the Badenes et al. (2018) analysis. We further remove the 2893 stars (mostly giants) with $[{\rm Fe/H}] < -0.9$ and seven systems with $[{\rm Fe/H}] > 0.5$, leaving 88,346 stars across the interval $-0.9 \leqslant [{\rm Fe/H}] \leqslant 0.5$ in our final sample. The metallicity distribution is adequately modeled by a Gaussian with a mean of $\langle[{\rm Fe/H}]\rangle = -0.16$ and dispersion of $\sigma_{\rm [Fe/H]} = 0.26$ dex (see Figure 5).

We divide our sample according to the measured surface gravities and effective temperatures. Of the 88,346 stars in our full sample, 20,649 are MS dwarfs or Hertzsprung gap (HG) subgiants with $3.2 \leqslant \log g < 5.0$, while the remaining 67,697 are giants with $0.1 < \log g < 3.2$. The giants mostly have primary masses $M_1 \approx 1.1$–$2.0\,M_\odot$ with an average of $M_1 \approx 1.5\,M_\odot$ (see Figures 2 and 4 in Badenes et al. 2018). Our giant subsample includes both normal and red clump giants. APOGEE red clump giants were targeted differently (Zasowski et al. 2013) and, as a result, are slightly biased against close binaries (Badenes et al. 2018). Fortunately, only ≈20% of the APOGEE giants occupy the red clump (Badenes et al. 2018), so the bias in the RV variability fraction can be at most 20% for our overall giant subsample. For our MS/HG stars, a majority (13,864 objects; 67%) have effective temperatures $T_{\rm eff} = 4000$–5000 K, corresponding roughly to K IV/V stars with primary masses $M_1 \approx 0.6$–$1.1\,M_\odot$. Another 5375 MS/HG stars (26%) have $T_{\rm eff} = 5000$–6000 K, corresponding approximately to G IV/V stars with $M_1 \approx 0.9$–$1.4\,M_\odot$. The remaining 1410 MS/HG stars (7%) are either cool early-M dwarfs ($T_{\rm eff} = 3500$–4000 K) or hot late-F stars ($T_{\rm eff} = 6000$–6500 K). In the following, we separately analyze our three main subsamples: giants ($N = 67{,}697$), K IV/V stars ($N = 13{,}864$), and G IV/V stars ($N = 5375$). As shown in Figure 5, giants dominate the total sample and peak at $[{\rm Fe/H}] \approx -0.2$. Meanwhile, K IV/V and G IV/V stars are systematically younger and peak at slightly larger metallicities, $[{\rm Fe/H}] \approx 0.0$.

The resolution $R \approx 22{,}500$ ($13\,\mathrm{km\,s^{-1}}$) of the APOGEE spectra is similar to the Latham et al. (2002) and Carney et al. (2005) observations ($R \approx 35{,}000$; $9\,\mathrm{km\,s^{-1}}$). However, our selected subsample of high-quality APOGEE spectra has an average $\langle \mathrm{S/N} \rangle \approx 110$, which is a factor of six times larger than the mean $\langle \mathrm{S/N} \rangle \approx 15$–$20$ of the Carney–Latham observations. The average RV measurement uncertainties are $\langle \sigma_{\mathrm{RV,meas}} \rangle = 0.02$, 0.04, and $0.05\,\mathrm{km\,s^{-1}}$ for our giant, K IV/V, and G IV/V subsamples, respectively. For our K IV/V subsample, the 1st–99th percentile range in the RV measurement uncertainties is $\sigma_{\mathrm{RV,meas}} = 0.006$–$0.152\,\mathrm{km\,s^{-1}}$. The APOGEE RVs are substantially more precise than the mean RV uncertainties of $\langle \sigma_{\mathrm{RV}} \rangle = 0.5$–$1.0\,\mathrm{km\,s^{-1}}$ in the Latham et al. (2002) sample (see Figure 1).

The number and time span of the APOGEE RV observations are comparatively smaller, but fortunately, they do not vary significantly with metallicity. For metal-poor ($-0.9 < [\mathrm{Fe/H}] < -0.7$) and metal-rich ($0.3 < [\mathrm{Fe/H}] < 0.5$) K IV/V stars, the mean numbers of RV measurements are $\langle N_{\mathrm{RV}} \rangle = 2.93$ and 3.04, respectively, and the median time spans are $\Delta t = 33$ and 37 days, respectively. We find similar results for the giant and G IV/V subsamples. The APOGEE sample is incomplete toward SBs with longer periods due to the limited time span, but the superior RV precision helps significantly to offset this effect. The time spans of the APOGEE observations vary substantially from system to system. For K IV/V stars, the 15th–85th percentile range in the time span is $\Delta t = 23$–305 days. When correcting for incompleteness (see below), we assume that the cadence is independent of metallicity but account for the small number of observations and wide distribution in the time spans.

The RV uncertainties in our APOGEE sample decrease with metallicity, similar to the trend in the Carney–Latham sample. In particular, the mean RV measurement uncertainty for K IV/V stars decreases by a factor of ≈ 2.9 from $\langle \sigma_{\mathrm{RV,meas}} \rangle = 0.08\,\mathrm{km\,s^{-1}}$ across $-0.9 < [\mathrm{Fe/H}] < -0.7$ to $\langle \sigma_{\mathrm{RV,meas}} \rangle = 0.03\,\mathrm{km\,s^{-1}}$ across $0.3 < [\mathrm{Fe/H}] < 0.5$. It is therefore crucial that we do not follow Latham et al. (2002) and Carney et al. (2005) by defining the SB fraction according to those systems that exhibit RV variability above some statistical significance.

Another reason to avoid this definition is because a substantial fraction of our giants are RV variables due to RV jitter. The mean surface gravity of giants in our sample is $\log g = 2.4$, and such giants exhibit and average RV jitter of $\sigma_{\mathrm{RV,jitter}} = 0.07\,\mathrm{km\,s^{-1}}$ according to Figure 3 in Hekker et al. (2008). In addition, we find that the APOGEE pipeline underestimates the true RV uncertainties for systems with very small measurement uncertainties, e.g., $\sigma_{\mathrm{RV,meas}} \lesssim 0.1\,\mathrm{km\,s^{-1}}$. Many RV variables with very small amplitudes are actually spurious. To account for both RV jitter and systematic effects in the APOGEE pipeline, we add a systematic uncertainty of $\sigma_{\mathrm{RV,sys}}$ in quadrature with each of the measurement uncertainties. As shown in Figure 6, the fraction of systems that exhibit RV variability above the 5σ significance level decreases as the assumed value for $\sigma_{\mathrm{RV,sys}}$ increases. The curves in Figure 6 rapidly decline and then begin to flatten beyond $\sigma_{\mathrm{RV,sys}} \gtrsim 0.08\,\mathrm{km\,s^{-1}}$. We therefore adopt a systematic uncertainty of $\sigma_{\mathrm{RV,sys}} = 0.08\,\mathrm{km\,s^{-1}}$ for all three subsamples. Systems that exhibit statistically significant RV variability well above the total RV uncertainty $\sigma_{\mathrm{RV,tot}} = (\sigma^2_{\mathrm{RV,meas}} + \sigma^2_{\mathrm{RV,sys}})^{1/2}$ are real SBs.

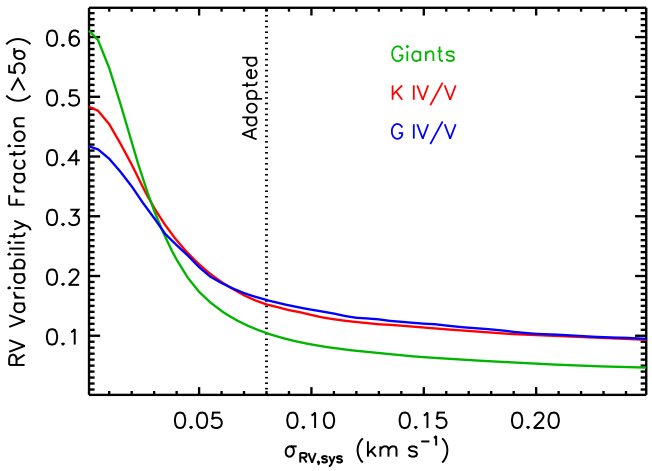

Figure 6. Fraction of APOGEE stars that exhibit RV variability above the 5σ significance level as a function of an assumed value of systematic uncertainty $\sigma_{\mathrm{RV,sys}}$ for our giant (green), K IV/V (red), and G IV/V (blue) subsamples. Assuming no systematic uncertainty, a significant fraction of APOGEE stars are spurious RV variables due to either RV jitter and/or the APOGEE pipeline underestimating the true RV uncertainties. The curves begin to significantly flatten beyond $\sigma_{\mathrm{RV,sys}} \gtrsim 0.08\,\mathrm{km\,s^{-1}}$, so we add a systematic uncertainty of $\sigma_{\mathrm{RV,sys}} = 0.08\,\mathrm{km\,s^{-1}}$ (dotted line) in quadrature with all of the measurement uncertainties.

4.2. RV Variability Fractions

As advocated in Badenes et al. (2018), we instead measure the RV variability fraction according to the fraction of stars that exhibit a maximum difference in RVs, $\Delta \mathrm{RV_{max}}$, between any two epochs above a certain threshold, $\Delta \mathrm{RV_{threshold}}$. Based on this definition, the close binary fraction is directly proportional to the observed RV variability fraction; i.e., corrections for incompleteness are independent of metallicity. In Figure 7, we show the RV variability fraction as a function of $\Delta \mathrm{RV_{threshold}}$ for our giant, K IV/V, and G IV/V subsamples. For the K IV/V and G IV/V subsamples, the RV variability fraction increases from $\approx 4.4\%$ for $\Delta \mathrm{RV_{max}} > 10\,\mathrm{km\,s^{-1}}$ to $\approx 12\%$–13% for $\Delta \mathrm{RV_{max}} > 1\,\mathrm{km\,s^{-1}}$. The similarity in their RV variability distributions, in terms of both functional form and normalization, suggests that K IV/V and G IV/V stars have the same close binary fraction and period distribution. The relative change in the close binary fraction between these two subsamples can be at most $\Delta F_{\mathrm{close}}/F_{\mathrm{close}} < 20\%$ (2σ confidence level). This is consistent with previous studies that show that the close binary fraction changes only slightly between early-M and G dwarfs (Fischer & Marcy 1992; Raghavan et al. 2010; Clark et al. 2012; Duchêne & Kraus 2013; Murphy et al. 2018). The RV variability fraction for our giant subsample is considerably lower, increasing from $\approx 1.3\%$ for $\Delta \mathrm{RV_{max}} > 10\,\mathrm{km\,s^{-1}}$ to $\approx 6.9\%$ for $\Delta \mathrm{RV_{max}} > 1\,\mathrm{km\,s^{-1}}$. As discussed in Section 3 and Badenes et al. (2018), giant evolution truncates the short-period tail of the binary period distribution, thereby removing SBs with large RV amplitudes.

We display the false-positive rate in Figure 7, i.e., the fraction of systems that have both $\Delta \mathrm{RV_{max}} > \Delta \mathrm{RV_{threshold}}$ and a difference in RVs that are discrepant with each other by less than 5σ. We also display the difference between the RV variability fraction and false-positive rate, which provides the

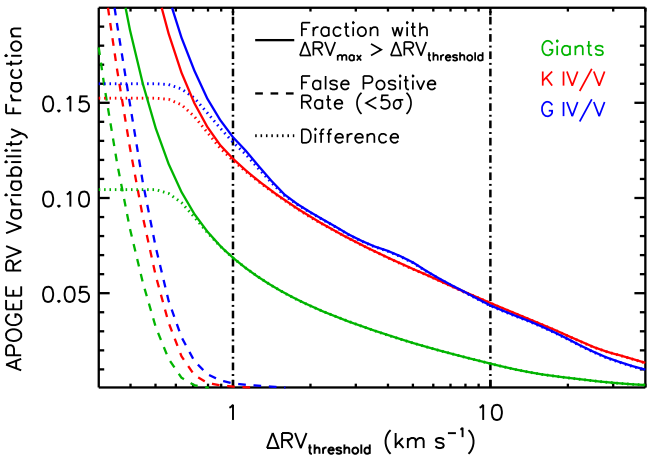

Figure 7. Fraction of APOGEE stars that exhibit RV variability above $\Delta RV_{max} > \Delta RV_{threshold}$ (solid lines), fraction of systems that have $\Delta RV_{max} > \Delta RV_{threshold}$ but are consistent with a constant RV within the 5σ tolerance level (dashed lines), and difference between these two distributions (dotted lines) for our giant (green), K IV/V (red), and G IV/V (blue) subsamples. Badenes et al. (2018) adopted a conservative threshold of $\Delta RV_{threshold} = 10\,km\,s^{-1}$ (right dash-dotted line) to be 100% certain that all RV variables were real SBs. We adopt a threshold of $\Delta RV_{threshold} = 1\,km\,s^{-1}$ (left dash-dotted line) in order to retain a significant majority of real SBs while simultaneously keeping the false-positive rate below <1% for all three subsamples and across all metallicities.

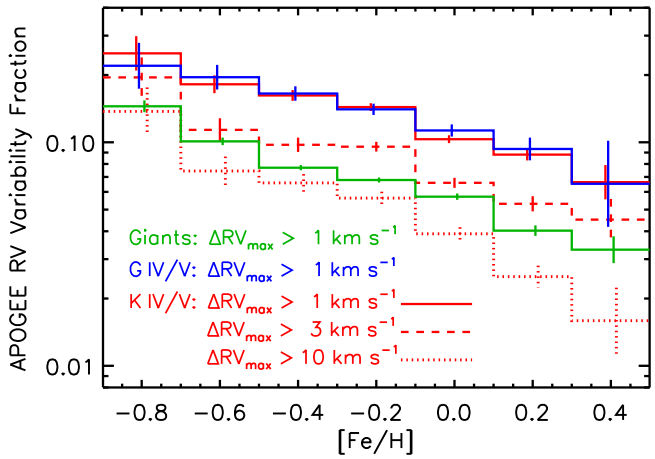

Figure 8. Fraction of APOGEE stars that exhibit RV variability above $\Delta RV_{max} > 1\,km\,s^{-1}$ (solid lines) for our giant (green), G IV/V (blue), and K IV/V (red) subsamples. We also display the fraction of K IV/V stars with $\Delta RV_{max} > 3\,km\,s^{-1}$ (dashed red lines) and $\Delta RV_{max} > 10\,km\,s^{-1}$ (dotted red lines). The RV variability fraction decreases with metallicity at a similar rate for all three subsamples and RV thresholds. Combining the giant, G IV/V, and K IV/V subsamples, the RV variability fraction decreases by a factor of 4.0 ± 0.5 across $-0.9 < [Fe/H] < 0.5$ at the 22σ confidence level.

real SB fraction. Badenes et al. (2018) chose a very conservative threshold of $\Delta RV_{threshold} = 10\,km\,s^{-1}$ in order to be certain that all of their RV variables were real binaries (see their Figure 9). Indeed, we find that 100% of RV variables with $\Delta RV_{max} > 10\,km\,s^{-1}$ are real; i.e., the false-positive rate is zero for all three subsamples (see Figure 7). The false-positive rate remains zero down to $\Delta RV_{threshold} = 2\,km\,s^{-1}$ and then steadily increases below $\Delta RV_{threshold} \lesssim 1\,km\,s^{-1}$. Systems with $\Delta RV_{max} \lesssim 0.4\,km\,s^{-1}$ are consistent with constant RV or exhibit RV jitter.

We adopt a threshold of $\Delta RV_{threshold} = 1\,km\,s^{-1}$ (Figure 7), but we also keep track of large-amplitude RV variables with $\Delta RV_{max} > 3$ and $10\,km\,s^{-1}$ to perform consistency checks (see below). A significant majority (≈70%–80%) of the real SBs have $\Delta RV_{max} > 1\,km\,s^{-1}$. The false-positive rate is also negligible above $\Delta RV_{max} > 1\,km\,s^{-1}$, e.g., 0.0%, 0.1%, and 0.3% for our giant, K IV/V, and G IV/V subsamples, respectively. Our threshold of $\Delta RV_{threshold} = 1\,km\,s^{-1}$ is well above the systematic uncertainty $\sigma_{RV,sys} \approx 0.08\,km\,s^{-1}$. The few false positives with $\Delta RV_{max} \approx 1.0$–$1.5\,km\,s^{-1}$ simply have larger measurement uncertainties, $\sigma_{RV,meas} \approx 0.2\,km\,s^{-1}$, compared to the average. The false-positive rate increases slightly toward lower metallicities for our adopted threshold. Nonetheless, the false-positive rate is extremely small across all metallicities, especially compared to the RV variability fraction. For instance, the false-positive rate for metal-poor K IV/V stars with $-0.9 < [Fe/H] < -0.5$ is 0.8% above $\Delta RV_{max} > 1\,km\,s^{-1}$. For this same metal-poor subset, the ratio of the false-positive rate to the RV variability fraction is only 4.3%. In other words, ≈96% of metal-poor K IV/V RV variables with $\Delta RV_{max} > 1\,km\,s^{-1}$ are real SBs. A systematic uncertainty of $\delta F_{close}/F_{close} \approx 4\%$ in the inferred close binary fraction due to spurious RV variables is much smaller than the measurement uncertainties and other sources of systematic error (see below).

4.3. Variations with Metallicity

As displayed in Figure 8, the fraction of APOGEE stars that exhibit RV variability above $\Delta RV_{max} > 1\,km\,s^{-1}$ decreases dramatically with metallicity for all three subsamples. For K IV/V stars, the RV variability fraction decreases by a factor of $3.8^{+1.2}_{-0.9}$ from $25\% \pm 5\%$ across $-0.9 < [Fe/H] < -0.7$ to $6.6\% \pm 1.3\%$ across $0.3 < [Fe/H] < 0.5$. Attempting to fit a uniform RV variability fraction for K IV/V stars across the seven metallicity bins in Figure 8 results in a reduced $\chi^2/\nu = 19.7$ with $\nu = 6$ degrees of freedom. The probability of exceeding this value is $p = 4 \times 10^{-23}$; i.e., the RV variability fraction of K IV/V stars decreases with metallicity at the 9.9σ significance level.[4] The G IV/V histogram in Figure 8 is consistent with the K IV/V histogram but has larger uncertainties due to the smaller sample size. The RV variability fraction of giants is measurably smaller due to the effective removal of very close binaries but nonetheless exhibits the same metallicity trend. The giant RV variability fraction decreases by a factor of $4.4^{+0.8}_{-0.6}$ from $14.5\% \pm 0.9\%$ at $[Fe/H] \approx -0.8$ to $3.3\% \pm 0.5\%$ at $[Fe/H] \approx 0.4$. A model of a uniform RV variability fraction for giants results in an even larger reduced $\chi^2/\nu = 62.1$ that can be rejected at the 18.6σ confidence level ($p = 2 \times 10^{-77}$). By combining the results from our three independent subsamples, the RV variability fraction decreases by a factor of 4.0 ± 0.5 across $-0.9 < [Fe/H] < 0.5$ at the 21.9σ significance level.

The relative decrease in the RV variability fraction as a function of metallicity is consistent among our K IV/V, G IV/V, and giant subsamples. This indicates that the slope of the anticorrelation between the close binary fraction and metallicity is similar across primary masses $M_1 \approx 0.6$–$1.5\,M_\odot$. The consistency also suggests that the binary fraction decreases with metallicity at a similar rate for both very close companions

[4] Mapping between such a low probability and large confidence level is not well defined in the extreme tail of a probability distribution. Nevertheless, the result is quite statistically significant, so we report the calculated confidence levels and probabilities throughout our study in order to enable reproducibility and convey that the measured metallicity trend is robust.

orbiting small MS/HG stars and slightly wider companions orbiting larger giants.

We also display in Figure 8 the fraction of K IV/V stars with $\Delta RV_{max} > 3$ and 10 km s^{-1}, which both exhibit the same metallicity trend as K IV/V binaries with smaller RV amplitudes. Utilizing the K IV/V histogram with $\Delta RV_{max} > 1$ km s^{-1} as a template, we multiply this distribution by a reduction factor R to fit the other K IV/V histograms. We measure $R_{3\,to\,1} = N(\Delta RV_{max} > 3\,km\,s^{-1})/N(\Delta RV_{max} > 1\,km\,s^{-1}) = 0.65 \pm 0.03$ with goodness-of-fit parameter $\chi^2/\nu = 0.43$ ($p = 0.86$). Similarly, we fit $R_{10\,to\,1} = N(\Delta RV_{max} > 10\,km\,s^{-1})/N(\Delta RV_{max} > 1\,km\,s^{-1}) = 0.38 \pm 0.02$ with $\chi^2/\nu = 1.9$ ($p = 0.08$). If spurious RV variables with $\Delta RV_{max} = 1$–3 km s^{-1} had significantly contaminated metal-poor systems, we would have expected the $\Delta RV_{max} > 1$ km s^{-1} distribution to be steeper than the $\Delta RV_{max} > 3$ km s^{-1} distribution. Instead, all three K IV/V histograms in Figure 8 have the same slope, which further demonstrates that false positives negligibly affect the distribution with $\Delta RV_{max} > 1$ km s^{-1}. The consistency also suggests that the frequency of very close binaries, which dominate the large-amplitude RV tail with $\Delta RV_{max} > 10$ km s^{-1}, decreases with metallicity at a similar rate as slightly wider binaries.

As discussed in Badenes et al. (2018), systematic uncertainties can potentially bias the measured relation between the RV variability fraction and metallicity, but to a substantially smaller degree than the observed anticorrelation. For example, metal-poor stars are systematically older and therefore have a larger fraction of close white dwarf (WD) companions. In the field, ≈20% of close companions to solar-type stars are WDs (Moe & Di Stefano 2017; Murphy et al. 2018). The close binary fraction therefore increases by $\Delta F_{close}/F_{close} \approx$ 5%–10% between metal-rich field stars and slightly older metal-poor field stars due to the larger frequency of close WDs. Similarly, older metal-poor binaries have had more time for tidal friction and magnetic braking to harden the orbit, thereby boosting the RV variability fraction. However, only ≈2% of solar-type stars in volume-limited samples have $P < 10$ days (Duquennoy & Mayor 1991; Raghavan et al. 2010; Tokovinin 2014; Moe & Di Stefano 2017), so tidal friction and magnetic braking alone cannot explain the observed RV variability fraction of 25% ± 5% for metal-poor K IV/V stars. Finally, we selected our giant, K IV/V, and G IV/V subsamples according to fixed intervals of surface gravity and temperature, not mass. By interpolating the Dartmouth stellar evolutionary tracks (Dotter et al. 2008), we find that an $M_1 = 0.9\,M_\odot$ star with [Fe/H] = 0.4 and age $\tau = 5$ Gyr has $\log g \approx 4.53$ and $T_{eff} \approx 5100$ K. Meanwhile, a metal-poor star with [Fe/H] = −0.8 of the same mass and age is substantially smaller ($\log g = 4.43$) and hotter ($T_{eff} = 6300$ K) due to the decreased opacities. To extend down to $T_{eff} \approx 5100$ K, a metal-poor dwarf with [Fe/H] = −0.8 must be $M_1 \approx 0.67\,M_\odot$. Given the same cuts in $\log g$ and T_{eff}, the metal-poor stars in our APOGEE subsamples are $\Delta M_1 \approx 0.2\,M_\odot$ less massive than their metal-rich counterparts. The close binary fraction increases slightly with primary mass across $M_1 \approx 0.5$–$1.5\,M_\odot$. Our selection criteria therefore lead to an ≈10% bias in the metallicity-versus-binary relation in the positive direction. This effect is the opposite of the observed anticorrelation; i.e., consideration of this particular selection bias strengthens our overall conclusion. In any case, the systematic uncertainty $\delta F_{close}/F_{close} \approx 10\%$ in the inferred close binary fraction is insignificant compared to the observed factor of 4.0 ± 0.5 decrease across −0.9 < [Fe/H] < 0.5. We confirm the conclusion of Badenes et al. (2018) that the RV variability fraction, and thus the intrinsic close binary fraction, strongly decreases with metallicity.

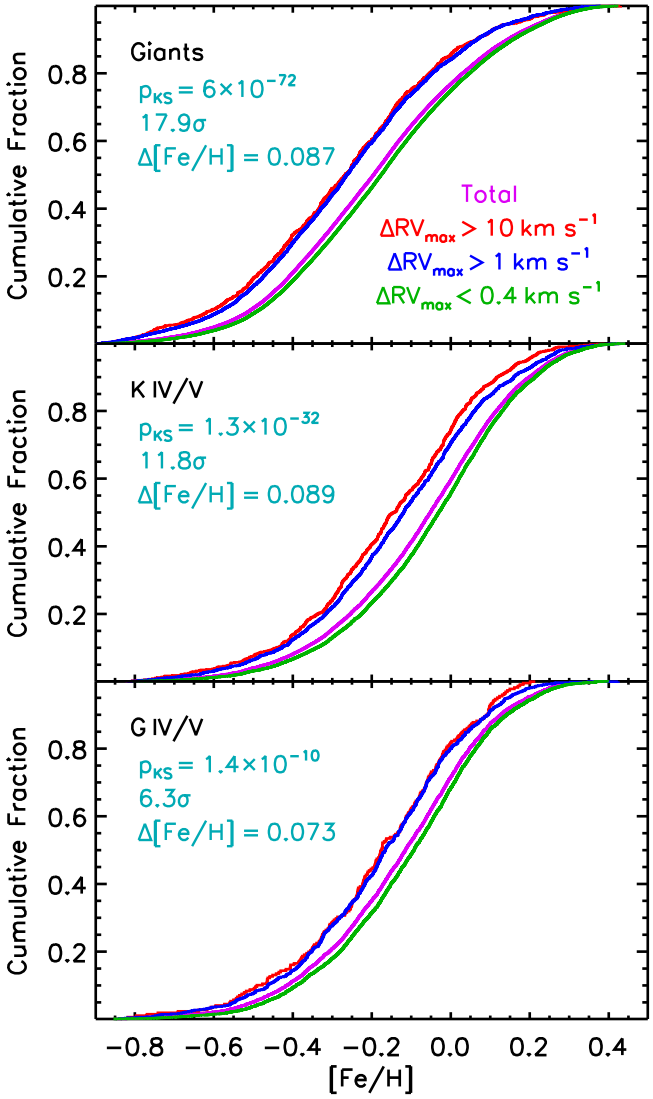

Figure 9. Cumulative metallicity distributions of giants (top), K IV/V stars (middle), and G IV/V stars (bottom) for the total populations (magenta), RV variables with $\Delta RV_{max} > 10$ km s^{-1} (red), RV variables with $\Delta RV_{max} > 1$ km s^{-1} (blue), and constant RV stars with $\Delta RV_{max} < 0.4$ km s^{-1} (green). We indicate in cyan the probability that the blue and green distributions are drawn from the same parent distribution according to a K-S test, the corresponding level of significance, and the difference in their median metallicities. After correcting for incompleteness, the median metallicities of close binaries are Δ[Fe/H] = 0.13 ± 0.03 smaller than single stars.

4.4. Cumulative Metallicity Distributions

In Figure 9, we display the cumulative distribution of metallicities for our giant, K IV/V, and G IV subsamples. For each subsample, we show the metallicity distributions for large-amplitude RV variables with $\Delta RV_{max} > 10$ km s^{-1},

small-amplitude RV variables with $\Delta RV_{max} > 1\,km\,s^{-1}$, and constant RV stars with $\Delta RV_{max} < 0.4\,km\,s^{-1}$. The distributions of small- and large-amplitude RV variables are consistent with each other. For K IV/V stars, a K-S test shows that the probability the $\Delta RV_{max} > 1$ and $10\,km\,s^{-1}$ histograms are drawn from the same parent distribution is $p_{K\text{-}S} = 0.20$. For giants and G IV/V stars, the RV variability distributions are even closer, resulting in $p_{K\text{-}S} = 0.71$ and 0.99, respectively. This further demonstrates that false positives negligibly affect RV variables with $\Delta RV_{max} = 1.0$–$2.0\,km\,s^{-1}$ and that very close binaries that produce large-amplitude RV variations follow the same metallicity trend as slightly wider binaries.

Meanwhile, RV variables are noticeably shifted toward smaller metallicities compared to both the total population and especially the constant RV stars. The K-S tests demonstrate that the $\Delta RV_{max} > 1$ and $<0.4\,km\,s^{-1}$ distributions are discrepant with each other at the 17.9σ ($p_{K\text{-}S} = 6 \times 10^{-72}$), 11.8σ ($p_{K\text{-}S} = 1.3 \times 10^{-32}$), and 6.3σ ($p_{K\text{-}S} = 1.4 \times 10^{-10}$) confidence levels for the giant, K IV/V, and G IV/V subsamples, respectively. These levels of statistical significance are similar to those found above but are based on the discrete metallicity distributions instead of the binned RV variability fractions. Both the χ^2 and K-S tests confirm that the close binary fraction decreases with metallicity at the $\approx 20\sigma$ confidence level.

Close binaries have systematically smaller metallicities compared to single stars and wide binaries. We measure the differences between the median metallicities of the $\Delta RV_{max} > 1\,km\,s^{-1}$ and total populations to be $\Delta[Fe/H] = 0.068$, 0.067, and 0.051 for the giant, K IV/V, and G IV/V subsamples, respectively. The metallicity differences between the $\Delta RV_{max} > 1$ and $<0.4\,km\,s^{-1}$ distributions are slightly larger at $\Delta[Fe/H] = 0.087$, 0.089, and 0.073. Constant RV stars mainly consist of single stars and wide binaries but also include close binaries that have small velocity amplitudes or were observed with an unfavorable cadence to detect RV variations. As we calculate in Section 4.5, the fraction of close binaries ($P < 10^4$; $a \lesssim 10\,au$) that are detectable as APOGEE RV variables with $\Delta RV_{max} > 1\,km\,s^{-1}$ is $\approx 60\%$. The median metallicities of close binaries are therefore $\Delta[Fe/H] = 0.11 \pm 0.02$ smaller than single stars and wide binaries with $a \gtrsim 10\,au$. Very wide binaries with $a \gtrsim 200\,au$ do not depend significantly on metallicity, while solar-type binaries with intermediate separations $a \approx 10$–$200\,au$ likely exhibit a weak metallicity anticorrelation (see Sections 2 and 6). We estimate that the median metallicities of close binaries are $\Delta[Fe/H] = 0.13 \pm 0.03$ smaller than single stars and very wide binaries with $a \gtrsim 200\,au$. This difference may seem relatively small compared to the broad metallicity distribution of solar-type stars. However, the mean metallicities of large stellar populations, such as the APOGEE sample, are measured to extremely high precision: $\delta\langle[Fe/H]\rangle \approx 0.02$ dex. A metallicity difference of $\Delta[Fe/H] = 0.13 \pm 0.03$ between close binaries and single stars therefore represents a relatively substantial offset.

4.5. Corrections for Incompleteness

We next correct for incompleteness to recover the intrinsic close binary fraction from the observed RV variability fraction. Accounting for the distribution of giant surface gravities, how close binaries evolve during giant expansion, the larger RV jitter associated with very luminous giants, and the differences in target selection of red clump versus normal giants is beyond the scope of this paper (see Badenes et al. 2018). A more detailed analysis of RV variability in APOGEE giants utilizing the more recent data release 14 is the subject of a future study (C. Mazzola et al. 2019, in preparation). In the present study, we combine our K IV/V and G IV/V subsamples, and we account only for incompleteness to measure the close binary fraction.

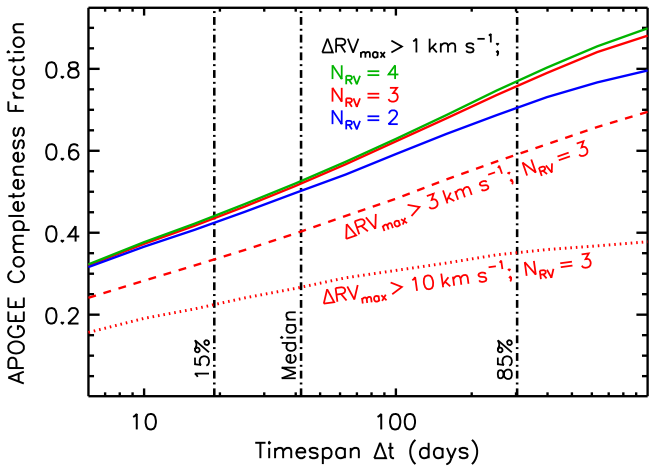

Figure 10. Simulated fraction of close binaries below $P < 10^4$ days ($a \lesssim 10$ au) that exhibit RV variability above $\Delta RV_{max} > 1$ (solid line), 3 (dashed line), and $10\,km\,s^{-1}$ (dotted line) given $N_{RV} = 2$ (blue), 3 (red), and 4 (green) RV measurements as a function of time span Δt between the first and final visits. APOGEE observed the 19,239 GK IV/V stars in our sample with varying cadence, and we indicate the 15th percentile, median, and 85th percentile in time spans with vertical dash-dotted lines.

We modify our Monte Carlo model in Section 3.1.2 to compute the completeness fraction C of close binaries with $P = 1$–10^4 days that are detectable as APOGEE RV variables. We adopt a primary mass of $M_1 = 0.9\,M_\odot$ appropriate for the combined GK IV/V subsample. We calculate the probability of detecting RV variations as a continuous function of time span Δt. We generate RVs at $N_{RV} = 2$, 3 (average), and 4 epochs. For $N_{RV} = 2$, the two epochs span Δt, while for $N_{RV} = 3$ and 4, the additional epochs are randomly distributed across Δt. We do not add noise to the simulated RVs because the RV uncertainties are below our adopted RV thresholds. We simply calculate the fraction of close binaries that have $\Delta RV_{max} > \Delta RV_{threshold}$ for $\Delta RV_{threshold} = 1$, 3, and $10\,km\,s^{-1}$.

We display in Figure 10 the simulated completeness fractions C as a function of Δt for the different values of N_{RV} and $\Delta RV_{threshold}$. The fraction of close binaries that are detectable as RV variables increases nearly linearly with respect to $\log \Delta t$. Given $N_{RV} = 3$, the fraction of close binaries that have $\Delta RV_{max} > 1\,km\,s^{-1}$ increases from $C = 37\%$ for $\Delta t = 10$ days to $C = 88\%$ for $\Delta t = 1000$ days. The number N_{RV} of RV observations only slightly affects the detection rates. In particular, a fourth RV measurement negligibly increases the completeness fraction unless it also extends the time span between the first and final visits. The completeness curves for $\Delta RV_{max} > 3\,km\,s^{-1}$ and $\Delta RV_{max} > 10\,km\,s^{-1}$ are substantially smaller, and the latter is also flatter with respect to Δt. Even with an infinite number and time span of RV observations, only $C \approx 45\%$ of close binaries with $P = 1$–10^4 days produce large-amplitude RV variations above $\Delta RV_{max} > 10\,km\,s^{-1}$.

For our combined GK IV/V subsample, the 15th percentile, median, and 85th percentile in time spans are $\Delta t = 19$, 42, and

303 days, respectively, which we indicate in Figure 10. Given the wide spread in time spans, we do not adopt the median but instead weight our Monte Carlo models according to the actual cadence of the APOGEE observations. We calculate weighted completeness fractions of $C = 0.57$, 0.40, and 0.24 for $\Delta RV_{max} > 1$, 3, and 10 km s^{-1}, respectively.

The underlying eccentricity and mass-ratio distributions do not significantly affect the simulated completeness rates. We consider thermal (Heggie 1975) and Gaussian ($\mu_e = 0.4$; $\sigma_e = 0.2$) eccentricity distributions and find that the completeness fractions change by less than $\Delta C/C < 3\%$ compared to our adopted uniform eccentricity distribution. In addition to a pure uniform mass-ratio distribution, we also consider a small excess fraction of twins with $q = 0.95$–1.00 that decreases from $F_{twin} = 30\%$ at $\log P(\text{days}) = 0$ to $F_{twin} = 10\%$ at $\log P = 4$, consistent with observations of close solar-type binaries (Tokovinin 2000; Moe & Di Stefano 2017). The simulated completeness fractions increase marginally to $C = 0.58$, 0.41, and 0.26 for $\Delta RV_{max} > 1$, 3, and 10 km s^{-1}, respectively. However, in the magnitude-limited APOGEE survey, twin binaries are overrepresented due to Malmquist bias, sometimes referred to as Branch (1976) bias in the context of binary stars. An overall twin fraction of $F_{twin} \approx 15\%$ inside of $a < 10$ au would artificially increase the inferred close binary fraction by $\Delta F_{close}/F_{close} \approx 25\%$–35% due to Malmquist bias (see Section 5). Conversely, it is sometimes difficult to detect twins as RV variables, especially if they have long orbital periods. The absorption lines of short-period twins can be resolved as SB2s, but the spectroscopic features of long-period twins with small velocity semi-amplitudes are blended together. The APOGEE spectroscopic pipeline was not designed to fit absorption features from two or more stars, so the measured RV amplitudes of blended SB2s are systematically below their true RV amplitudes. Given the resolution $R \approx 22{,}500$ of APOGEE, we expect binaries with $a \gtrsim 0.5$ au and $q \gtrsim 0.8$ to have measured $\Delta RV_{max} < 1$ km s^{-1} below our adopted threshold. In a magnitude-limited sample, ≈20%–30% of binaries below $a < 10$ au have $a = 0.5$–10 au and $q > 0.8$. The effects of Malmquist bias and the inability to detect long-period binaries with $q \gtrsim 0.8$ as RV variables therefore nearly cancel, contributing an ≈5% net bias. We adopt our baseline completeness fractions of $C = 0.57$, 0.40, and 0.24 for $\Delta RV_{max} > 1$, 3, and 10 km s^{-1}, respectively, and propagate the systematic uncertainty associated with twin binaries.

Our Monte Carlo model, which incorporates the short-period tail of a lognormal period distribution (see Section 3.1.2), accurately reproduces the observed distribution of RV amplitudes. For example, the modeled ratio $R_{3\text{ to }1} = C(\Delta RV_{max} > 3\text{ km s}^{-1})/C(\Delta RV_{max} > 1\text{ km s}^{-1}) = 0.40/0.57 = 0.70$ between the completeness fractions is consistent with the observed ratio $R_{3\text{ to }1} = 0.65 \pm 0.03$ between the corresponding number of RV variables (see Section 4.3 and Figure 8). Similarly, the simulated ratio $R_{10\text{ to }1} = 0.24/0.57 = 0.42$ is slightly larger than but still consistent with the observed ratio $R_{10\text{ to }1} = 0.38 \pm 0.02$ between the number of large- and small-amplitude RV variables. If we instead adopt a uniform distribution in $\log P$, i.e., Opik's law, then we simulate larger completeness fractions of $C = 0.75$, 0.63, and 0.47 for $\Delta RV_{max} > 1$, 3, and 10 km s^{-1}, respectively, because more of the close binaries are weighted toward shorter periods. However, Opik's law predicts ratios of $R_{3\text{ to }1} = 0.63/0.75 = 0.84$ and $R_{10\text{ to }1} = 0.47/0.75 = 0.63$ that are clearly discrepant with the observed ratios of 0.65 ± 0.03 and 0.38 ± 0.02, respectively. Both metal-poor and metal-rich solar-type binaries therefore follow the same short-period tail of a lognormal period distribution. Metal-poor solar-type stars simply have a larger close binary fraction.

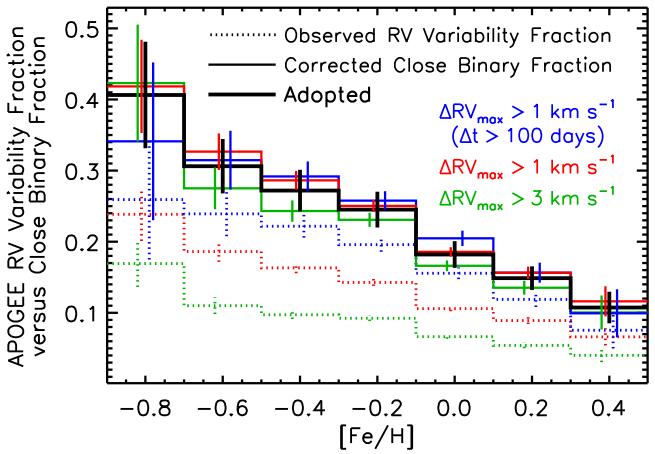

Figure 11. As a function of metallicity, the observed fraction of all GK IV/V APOGEE stars in our sample that exhibit RV variability above $\Delta RV_{max} > 3$ (dotted green) and 1 (dotted red) km s^{-1} and the observed fraction of GK IV/V APOGEE stars monitored during a time span of at least $\Delta t > 100$ days that exhibit RV variability above $\Delta RV_{max} > 1$ km s^{-1} (dotted blue). We divide these three histograms by their respective completeness fractions of $C = 0.40$, 0.57, and 0.76, resulting in the bias-corrected close binary fractions (thin colored lines). We adopt a weighted average and a systematic uncertainty of $\delta F_{close}/F_{close} = 10\%$, providing an intrinsic close binary fraction that decreases from $F_{close} = 41\% \pm 7\%$ at [Fe/H] = −0.8 to $F_{close} = 11\% \pm 2\%$ at [Fe/H] = +0.4 (thick black line).

Similar to Figure 8, we display in Figure 11 the fraction of GK IV/V stars with $\Delta RV_{max} > 1$ and 3 km s^{-1} as a function of metallicity. Of the 19,239 GK IV/V stars in our combined sample, 5394 (28%) were observed by APOGEE during a time span of at least $\Delta t > 100$ days. As shown in Figure 11, this subset exhibits a noticeably higher fraction of RV variables with $\Delta RV_{max} > 1$ km s^{-1} compared to the total GK IV/V sample. By fitting across all metallicities, we find that the RV variability fraction of GK IV/V stars observed with longer time spans is $R_{long/total} = 1.37 \pm 0.05$ times larger than the total GK IV/V population ($\chi^2/\nu = 0.49$, $p = 0.82$). With increased time spans, the APOGEE observations become more complete toward detecting SBs with longer periods (see Figure 10). We weight our Monte Carlo model according to the cadence of RV observations for the 5394 GK IV/V stars with $\Delta t > 100$ days. The resulting completeness fraction of $C = 0.76$ is $R_{long/total} = 0.76/0.57 = 1.33$ times larger than the completeness fraction for the total GK IV/V population. The simulated ratio nearly matches the observed ratio, providing another confirmation our Monte Carlo model accurately describes close solar-type binaries.

In Figure 11, we divide the observed RV variability fractions by their corresponding completeness fractions. The three resulting completeness-corrected close binary fractions are all consistent with each other. We adopt a weighted average of the three histograms and the measurement uncertainties from the distribution based on all GK IV/V RV variables with $\Delta RV_{max} > 1$ km s^{-1}. For each metallicity bin, we add a systematic uncertainty of $\delta F_{close}/F_{close} = 10\%$ in quadrature with the measurement uncertainties to account for the small selection biases discussed above.

We present our final completeness-corrected close binary fraction of GK IV/V stars as the thick black line in Figure 11. The intrinsic close binary fraction ($P < 10^4$ days; $a \lesssim 10$ au) decreases from $F_{\rm close} = 41\% \pm 7\%$ at [Fe/H] $= -0.8$ to $F_{\rm close} = 11\% \pm 2\%$ at [Fe/H] $= +0.4$. The metallicity-dependent close binary fraction inferred from the APOGEE RV variables and Carney–Latham SB samples (see Figure 3) are consistent with each other. Our APOGEE RV sample of 19,239 GK IV/V stars is a factor of 14 times larger than the Latham et al. (2002) sample. Moreover, APOGEE measured the RVs and metallicities of their targets to substantially higher precision. The anticorrelation between the close binary fraction and metallicity is therefore even more pronounced and measured to much higher statistical significance with the APOGEE data set.

5. *Kepler* EBs

5.1. Sample Selection and Description

The primary *Kepler* mission monitored nearly 200,000 solar-type stars for 4 yr with exquisite photometric precision. Designed to discover transiting exoplanets, *Kepler* also identified and characterized 2878 EBs and non-EB ellipsoidal variables (Prša et al. 2011; Kirk et al. 2016). About a third of the systems in the *Kepler* EB catalog have very short periods, $P < 1$ day, the majority of which are evolved contact or ellipsoidal binaries. Most of the *Kepler* EBs with longer periods are in pre-mass-transfer detached configurations. A few EBs have especially long periods, $P = 1000$–1100 days, but geometrical selection effects and the 4 yr lifetime of the main *Kepler* mission severely limited the discovery of such wide binaries. We initially select the 1924 EBs with $P = 1$–1000 days in the third revision of the *Kepler* EB catalog (Kirk et al. 2016).

5.1.1. Sample with Photometric Metallicities

Brown et al. (2011) utilized photometry, stellar isochrones, and a Bayesian model of the galactic stellar population to estimate $T_{\rm eff}$, $\log g$, and [Fe/H] for all stars in the *Kepler* input catalog. Specifically, they measured the spectral energy distribution (SED) of each *Kepler* star based on broadband optical photometry (*griz*), 2MASS near-infrared photometry (*JHK*), and an intermediate-band filter (D51) centered on the Fraunhofer b absorption lines near 515 nm that are associated with Mg and Fe. Brown et al. (2011) then fitted the measured SEDs to synthetic colors from ATLAS9 model atmospheres (Castelli & Kurucz 2004), assuming the dust extinction varied as a simple function of distance and galactic latitude. They also incorporated Bayesian priors in $T_{\rm eff}$, $\log g$, and [Fe/H] according to the observed distributions in the solar neighborhood. Huber et al. (2014) revised and significantly improved the measured parameters of 196,468 *Kepler* stars. They updated the photometry with recent observations, calibrated $T_{\rm eff}$ according to empirical relations, incorporated more accurate stellar isochrones from the Dartmouth evolutionary tracks (Dotter et al. 2008), and treated dust extinction in a more realistic manner. Huber et al. (2014) adopted Bayesian priors in $\log g$ and [Fe/H] similar to those in Brown et al. (2011) but developed a slightly more sophisticated method for sampling the distributions.

Brown et al. (2011) and Huber et al. (2014) stressed that the measured surface gravities and metallicities in their catalogs are highly uncertain and should not be used on a star-by-star basis. Nevertheless, they argued that the distributions of surface gravities and metallicities are statistically accurate and can therefore be utilized to study broad trends across these parameters. Brown et al. (2011) and Huber et al. (2014) also identified regions in the H-R diagram where the photometric solutions for $\log g$ and [Fe/H] are highly degenerate and most uncertain, notably for subgiants and cool late K- and M-type dwarfs. We therefore select the $N_{\rm phot} = 142{,}951$ solar-type dwarfs in the Huber et al. (2014) catalog with photometric parameters $T_{\rm eff} = 4800$–6800 K, $\log g = 4.0$–5.0, and $-1.7 <$ [Fe/H] < 0.5, corresponding approximately to F3V–K3V stars.

Berger et al. (2018) recently utilized *Gaia* parallactic distances to measure the stellar radii of *Kepler* stars and found that ≈65%, 23%, and 12% are MS stars, subgiants, and giants, respectively. They concluded that contamination by subgiants in the *Kepler* sample is smaller than previously thought. Moreover, a non-negligible fraction of the Berger et al. (2018) subgiants, which were identified because they lie slightly above the MS relation in the H-R diagram, are actually twin binaries with MS components of comparable luminosity. Thus, a significant majority of the solar-type dwarfs in our photometric sample are truly MS stars.

The metallicity distribution of our photometric sample of *Kepler* solar-type dwarfs follows a Gaussian with a mean of $\langle$[Fe/H]$\rangle = -0.17$ and dispersion of $\sigma_{\rm [Fe/H]} = 0.26$ dex. Huber et al. (2014) estimated that the uncertainties in the photometric metallicities of *Kepler* stars is δ[Fe/H] ≈ 0.3 dex. We can therefore examine metallicity trends across the much broader interval $-1.7 <$ [Fe/H] < 0.5. Of the 1924 *Kepler* EBs with $P = 1$–1000 days, $N_{\rm EB,phot} = 1292$ systems satisfy our selection criteria of $T_{\rm eff} = 4800$–6800 K, $\log g = 4.0$–5.0, and $-1.7 <$ [Fe/H] < 0.5, according to the Huber et al. (2014) photometric catalog. The observed EB fraction in our photometric sample of *Kepler* solar-type dwarfs is $F_{\rm EB,phot} = 1291/142{,}951 = 0.90\% \pm 0.03\%$.

The presence of a binary companion can potentially bias the metallicities inferred from fitting single-star isochrones to the measured photometry. The photometric metallicities of EBs in particular may be substantially inaccurate if the observations in the different filters correspond to different orbital phases, e.g., during versus outside of eclipse. In addition, the majority of very close binaries with $P \lesssim 7$ days have tertiary companions (Tokovinin et al. 2006), so most EBs also have third-light contamination.

We assess the significance of these potential biases by fitting isochrones to the simulated photometry of solar-type binaries. We download a dense grid of Dartmouth stellar evolutionary tracks (Dotter et al. 2008) spanning masses $M = 0.15$–$1.7\,M_\odot$, ages $\tau_* = 1$–13 Gyr, and metallicities $-2.4 <$ [Fe/H] < 0.5. We simulate binaries with metallicities [Fe/H] $= -1.3$, -0.8, -0.3, and $+0.2$ at representative ages of $\tau_* = 11$, 8, 5, and 2 Gyr, respectively. We select G8V primaries with $T_1 = 5500$ K, corresponding to primary masses $M_1 = 0.65$, 0.71, 0.82, and $0.98\,M_\odot$ for the four combinations of metallicities and ages. We also consider hotter F8V primaries with $T_1 = 6200$ K, corresponding to slightly higher masses of $M_1 = 0.75$, 0.84, 0.99, and $1.22\,M_\odot$. For different combinations of mass ratios $q = M_2/M_1$, we add the fluxes of both binary components for all eight filters (D51*grizJHK*) utilized in Brown et al. (2011) and Huber et al. (2014). We add a dust

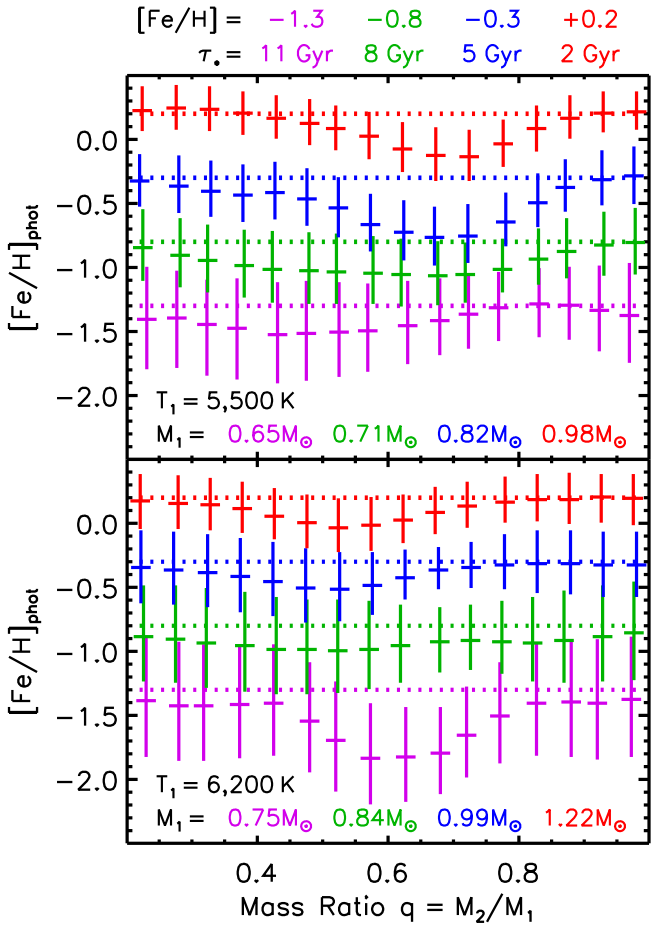

Figure 12. Photometric metallicities $[Fe/H]_{phot}$ determined by fitting single-star isochrones to simulated broadband photometry of binaries as a function of mass ratio q. We consider binaries with cooler ($T_1 = 5500$ K; top) and hotter ($T_1 = 6500$ K; bottom) primaries for four different metallicities, [Fe/H] = −1.3 (magenta), −0.8 (green), −0.3 (blue), and +0.2 (red), where we list the corresponding ages τ_* and primary masses M_1. For some combinations (e.g., $q \approx 0.6$), the fitted photometric metallicities underestimate the true metallicities (dotted lines) by as much as ≈0.5 dex. In general, however, the measurement uncertainties simply increase from ≈0.25 dex near $[Fe/H]_{phot} = 0.2$ to ≈0.45 dex near $[Fe/H]_{phot} = -1.3$, with negligible bias between the true and photometric metallicities.

extinction of $A_r = 0.2$ mag and adopt a dust reddening law from Schlafly & Finkbeiner (2011) such that $A_b/A_r = 1.45$, 1.31, 0.74, 0.55, 0.31, 0.20, and 0.13 for bands $b = g$, D51, i, z, J, H, and K, respectively. We do not fit the distances to our simulated binaries, so we consider only the seven unique color combinations. Brown et al. (2011) measured the bright *Kepler* stars to a precision of ≈0.02 mag in the D51*griz* filters, so we adopt uncertainties of 0.03 mag in all colors. We measure the photometric masses M_{phot}, ages τ_{phot}, metallicities $[Fe/H]_{phot}$, and dust extinctions $A_{r,phot}$ by minimizing the χ^2 statistic between the seven colors of our simulated binaries and the isochrones of single stars. We assume uniform priors in our four photometric parameters. In this manner, our fits are not dominated by short-lived phases of stellar evolution that provide only marginally smaller χ^2 values.

We measure the mean and 1σ uncertainties in the photometric metallicities $[Fe/H]_{phot}$ by marginalizing across the other parameters. We display the measured values of $[Fe/H]_{phot}$ in Figure 12 for the various combinations of [Fe/H], M_1, and q. The measurement uncertainties increase from $\delta[Fe/H] = 0.25$ dex near $[Fe/H] = +0.2$ to $\delta[Fe/H] = 0.45$ dex near $[Fe/H] = -1.3$, consistent with the average uncertainty of $\delta[Fe/H] = 0.3$ dex reported in Huber et al. (2014). Compared to their primaries, low-mass companions with $q < 0.4$ contribute negligible flux across the optical and near-infrared bands. For such extreme mass-ratio binaries, the photometric metallicities $[Fe/H]_{phot}$ determined by fitting single-star isochrones are close to the true metallicities [Fe/H]. Similarly, companions with $q > 0.8$ have SEDs similar to their primaries, so the photometric metallicities of twin binaries are consistent with their actual values. For $q \approx 0.4$–0.8, however, there are certain combinations of [Fe/H] and M_1 for which the photometric metallicities underestimate the true metallicities. In particular, Figure 12 shows that binaries with $T_1 = 5500$ K, $[Fe/H] \approx 0.0$, and $q \approx 0.6$–0.8 and $T_1 = 6200$ K, $[Fe/H] \approx -1.3$, and $q \approx 0.5$–0.7 are biased by $\Delta[Fe/H] \approx -0.5$ dex toward smaller metallicities. Fortunately, only ≈20% of close solar-type binaries have mass ratios spanning an interval of $\Delta q = 0.2$ near $q \approx 0.6$ (Raghavan et al. 2010; Tokovinin 2014; Moe & Di Stefano 2017). The photometric metallicities inferred from single-star isochrones are therefore slightly biased for only a small fraction of the close binary population.

The biases in the photometric metallicities due to eclipses and tertiary companions are even smaller. For most *Kepler* stars, Brown et al. (2011) rapidly cycled through all of the optical filters (D51*griz*) during a single pointing. The 2MASS near-infrared photometry was obtained at earlier epochs and likely coincides with different orbital phases. Fortunately, the optical bands, especially the D51 filter, provide the most leverage in constraining the metallicities. Moreover, the majority of *Kepler* EBs with $P = 1$–1000 days have shallow eclipses, e.g., 67% with $\Delta m < 0.1$ mag and 81% with $\Delta m < 0.2$ mag (Kirk et al. 2016). The listed optical–to–near-infrared colors of *Kepler* EBs differ from their true out-of-eclipse colors by $\lesssim$0.05 mag, on average. For *Kepler* EBs with longer periods, $P \gtrsim 20$ days, the durations of the eclipses are substantially shorter than their orbital periods. The photometric colors of long-period EBs are therefore much more likely to correspond to their out-of-eclipse values. Most importantly, the optical–to–near-infrared colors of EBs are randomly shifted toward either smaller or larger values relative to their out-of-eclipse colors; i.e., there is no net bias. Regarding triple stars, the majority of tertiary companions to very close binaries are weighted toward small mass ratios $q = M_3/M_1 < 0.5$ (Tokovinin et al. 2006; Moe & Di Stefano 2017). As demonstrated in Figure 12, low-mass companions negligibly affect the measured photometric metallicities. Although the majority of very close binaries have outer tertiaries, only ≈30% of binaries with $P > 20$ days are in triple systems (Tokovinin et al. 2006). We conclude that the biases in the photometric metallicities of *Kepler* EBs, especially those with $P > 20$ days, are negligible compared to the measurement uncertainties and other sources of systematic uncertainties that equally affect both EBs and single stars in the *Kepler* sample.

5.1.2. Sample with Spectroscopic Metallicities

The metallicities measured from stellar spectra are generally more precise and less biased than photometric metallicities derived from fitting stellar isochrones. Mathur et al. (2017) compiled dozens of follow-up surveys and provided spectroscopic metallicities $[Fe/H]_{spec}$ for 16,289 *Kepler* stars.

Unfortunately, their sample of *Kepler* stars with spectroscopic metallicities is a heterogenous, nonrandom subset and therefore cannot be utilized to investigate the EB fraction as a function of metallicity. For example, many *Kepler* stars received follow-up spectroscopic observations because their light curves exhibited transiting exoplanets. Other *Kepler* stars were observed spectroscopically because they displayed clean variability from pulsations that provide stringent tests for asteroseismic models. Such subsets are significantly biased against EBs. Nevertheless, the spectroscopic metallicities $[Fe/H]_{spec}$ in Mathur et al. (2017) provide insight into the accuracy of the photometric metallicities. We find that 15,801 of the *Kepler* stars with listed spectroscopic metallicities in Mathur et al. (2017) have photometric metallicities $-1.5 < [Fe/H]_{phot} < 0.5$ in Huber et al. (2014). We measure a significant degree of correlation between $[Fe/H]_{phot}$ and $[Fe/H]_{spec}$; e.g., the Pearson correlation coefficient is $r_P = 0.52$. The photometric metallicities can therefore be used to reliably measure trends between the EB fraction and metallicity.

The LAMOST spectroscopic survey ($R \approx 1800$) recently measured the metallicities of tens of thousands of *Kepler* stars (Dong et al. 2014; De Cat et al. 2015; Frasca et al. 2016; Ren et al. 2016). Unlike the compilation presented in Mathur et al. (2017), the LAMOST-*Kepler* project obtained spectra for a random subset of *Kepler* stars and is therefore not biased with respect to EBs. The metallicities of several hundred stars in the LAMOST-*Kepler* field were previously measured with high-resolution spectra and other robust techniques. Dong et al. (2014) and Ren et al. (2016) demonstrated that the metallicities derived from their low-resolution LAMOST spectra are consistent with these previous measurements. For dwarf stars, Ren et al. (2016) reported that the bias between the LAMOST and high-resolution spectroscopic metallicities is only δ[Fe/H] = 0.01 dex and that the measurement uncertainties in the LAMOST metallicities are typically $\sigma_{[Fe/H]} \approx 0.1$ dex.

Dong et al. (2014) and Ren et al. (2016) then compared their LAMOST spectroscopic metallicities to the photometric metallicities listed in the *Kepler* index catalog (Brown et al. 2011). They both found good agreement near subsolar metallicities $[Fe/H]_{phot} \approx [Fe/H]_{spec} \approx -0.4$ (see Figure 1 in Dong et al. 2014 and Figure 9 in Ren et al. 2016). For metal-rich dwarf stars, however, Dong et al. (2014) and Ren et al. (2016) showed that the photometric metallicities systematically underestimate the true metallicities by δ[Fe/H] = 0.4 dex. *Kepler* dwarfs with $[Fe/H]_{phot} \approx 0.0$ actually have true metallicities $[Fe/H]_{spec} \approx 0.4$. The shift is likely due to the Bayesian prior metallicity distribution adopted in Brown et al. (2011) and Huber et al. (2014), which peaks near $[Fe/H] \approx -0.2$ and is consistent with the distribution in the solar neighborhood. Meanwhile, Dong et al. (2014) and Ren et al. (2016) found that the true metallicity distribution of more distant *Kepler* stars peaks at [Fe/H] ≈ 0.0. Nonetheless, Dong et al. (2014) and Ren et al. (2016) both confirmed that $[Fe/H]_{phot}$ and $[Fe/H]_{spec}$ are significantly correlated. This reaffirms our conclusion that the photometric metallicities reported in Huber et al. (2014) provide leverage in measuring how the EB properties vary with metallicity.

For our *Kepler* sample with spectroscopic metallicities, we choose stars in the LAMOST-*Kepler* survey according to the same selection criteria as our photometric sample. Specifically, we select the $N_{spec} = 23{,}886$ solar-type *Kepler* dwarfs with LAMOST spectroscopic parameters $T_{eff} = 4800$–6800, $\log g = 4.0$–5.0, and $-1.7 < [Fe/H] < +0.5$ from Ren et al. (2016). The metallicity distribution is accurately modeled by a Gaussian with a mean of $\langle[Fe/H]\rangle = -0.05$ and dispersion of $\sigma_{[Fe/H]} = 0.21$, which is slightly more metal-rich than our photometric sample, as described above. We find that $N_{EB,spec} = 244$ of our *Kepler* solar-type dwarfs with spectroscopic metallicities are EBs with $P = 1$–1000 days (Kirk et al. 2016). The resulting EB fraction of $F_{EB,spec} = 244/23{,}866 = 1.02\% \pm 0.07\%$ is consistent with the fraction $F_{EB,phot} = 0.90\% \pm 0.03\%$ measured for our *Kepler* sample with photometric metallicities. This confirms that the LAMOST-*Kepler* survey was not biased against EBs. Although our *Kepler* sample of solar-type dwarfs with spectroscopic metallicities is six times smaller than our photometric sample, it is a representative subset, and the stellar metallicities are measured to much higher accuracy and precision.

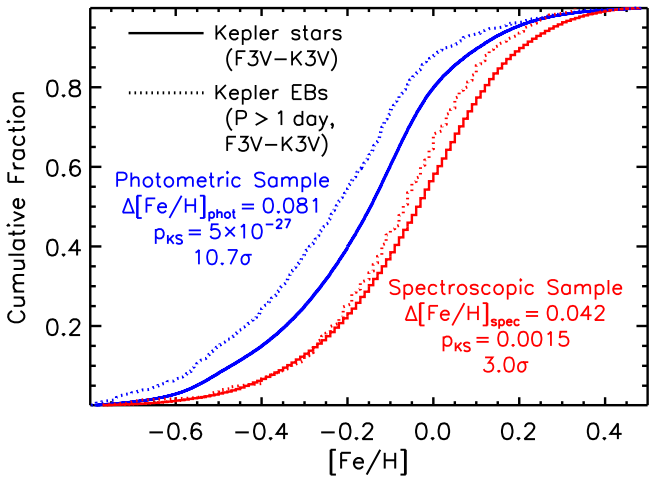

Figure 13. Cumulative metallicity distributions for our *Kepler* samples of solar-type dwarfs with photometric (solid blue line) and spectroscopic (solid red line) metallicities and the corresponding subsets that are EBs with $P = 1$–1000 days (dotted lines). For both the photometric and spectroscopic samples, the EBs are weighted toward smaller metallicities compared to their parent distributions at statistically significant levels.

5.2. Variations with Metallicity

In Figure 13, we investigate the cumulative metallicity distributions of our *Kepler* EBs. For visual clarity, we truncate the distributions in Figure 13 to the interval $-0.8 < [Fe/H] < 0.5$ but perform our statistical analysis across the full range, $-1.7 < [Fe/H] < 0.5$. For both our photometric and spectroscopic samples, the EBs in Figure 13 are noticeably weighted toward smaller metallicities compared to their respective parent distributions. For our *Kepler* sample of solar-type dwarfs with photometric metallicities, a K-S test demonstrates that the EBs are discrepant with the total population at the 10.7σ significance level ($p_{K\text{-}S} = 5 \times 10^{-27}$). We also find that the median metallicity of the EBs is shifted downward by $\Delta[Fe/H]_{phot} = 0.081$ dex compared to their parent distribution. This shift is slightly larger than but consistent with the differences $\Delta[Fe/H] \approx 0.05$–$0.07$ dex between APOGEE RV variables and their total populations, as reported in Section 4.4. The *Kepler* solar-type dwarfs with measured spectroscopic metallicities are weighted toward larger metallicities compared to the photometric sample due to the biases discussed above and in Dong et al. (2014) and Ren et al. (2016). Nevertheless, the EBs in the more precise spectroscopic sample also have

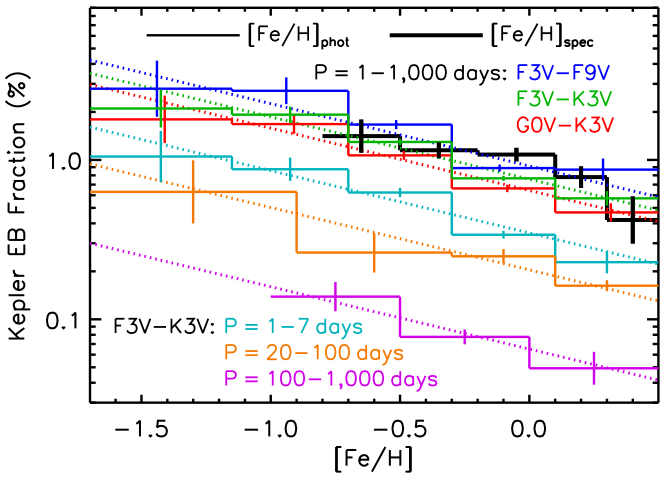

Figure 14. Fraction of *Kepler* solar-type dwarfs that are EBs with $P = 1$–1000 days within our full photometric sample (thin green line) and spectroscopic sample (thick black line). We divide the photometric sample according to spectral type: F3V–F9V (blue) and G0V–K3V (red). We also compare the EB fraction within our photometric sample across different periods: $P = 1$–7 (cyan), 20–100 (orange), and 100–1000 (magenta) days. All samples show a statistically significant decrease in the EB fraction with respect to metallicity. We show the fit $\log F_{\rm EB} \propto -0.39[{\rm Fe/H}]$ (dotted lines) to the overall photometric sample scaled to the various subsamples.

systematically lower metallicities ($\Delta[{\rm Fe/H}]_{\rm spec} = 0.042$ dex) than their parent distribution at the 3.0σ confidence level ($p_{\rm K\text{-}S} = 0.0015$). A two-sample Anderson–Darling test provides a slightly larger 3.4σ discrepancy. Despite the smaller sample size, *Kepler* EBs with measured spectroscopic metallicities confirm that close binaries are weighted toward lower metallicities at a statistically significant level.

In Figure 14, we next examine the *Kepler* EB fraction as a function of metallicity, spectral type, and orbital period. For our full photometric sample of *Kepler* F3V–K3V primaries, the EB fraction across $P = 1$–1000 days decreases by a factor of 3.4 ± 0.5 between $F_{\rm EB} = 1.9\% \pm 0.2\%$ near $[{\rm Fe/H}] = -0.9$ and $F_{\rm EB} = 0.57\% \pm 0.06\%$ at $[{\rm Fe/H}] = 0.3$ (green histogram in Figure 14). Attempting to fit a constant EB fraction to the five green metallicity bins in Figure 14 results in a reduced $\chi^2/\nu = 25.7$ with $\nu = 4$ degrees of freedom. A constant EB fraction with respect to metallicity can be rejected at the 9.4σ confidence level ($p = 2.6 \times 10^{-21}$), which is similar to the level of significance inferred from the cumulative metallicity distributions (see above). We instead find that the *Kepler* EB fraction is sufficiently modeled by a power law such that $\log F_{\rm EB} \propto (-0.39 \pm 0.05)[{\rm Fe/H}]$, which is displayed as the dotted green line in Figure 14.

We then divide the photometric sample into hot ($T_{\rm eff} = 6000$–6800 K) and cool ($T_{\rm eff} = 4800$–6000 K) dwarfs, corresponding to F3V–F9V and G0V–K3V spectral types, respectively. Both the hot and cool subsamples follow the same metallicity trend (blue and red histograms in Figure 14, respectively). This suggests that the close binary fraction and metallicity are anticorrelated to a similar degree across the primary mass interval $M_1 = 0.6$–$1.3\,M_\odot$. For all metallicities, the *Kepler* EB fraction of F3V–F9V stars is ≈40% larger than that of G0V–K3V stars for two reasons. First, F dwarfs are larger than G/early-K dwarfs, so their corresponding eclipse probabilities are ≈20%–30% larger (see Section 5.3). Second, the intrinsic close binary fraction of F dwarfs is ≈10%–20% larger than that of G/early-K dwarfs (Raghavan et al. 2010; Tokovinin 2014; Moe & Di Stefano 2017).

We next compare the EB fraction as a function of metallicity for different period intervals. Nearly half of our *Kepler* EBs have very short periods of $P = 1$–7 days (cyan histogram in Figure 14). As discussed in Section 5.1.1, such very close EBs have wide eclipses, and most have tertiary companions, so their photometric metallicities are most uncertain. Nevertheless, EBs with $P = 20$–100 days (orange histogram), which have narrow eclipses and are unlikely to be in triples, exhibit the same metallicity trend as the full sample. For visual clarity, we scale the power-law fit $\log F_{\rm EB} \propto -0.39[{\rm Fe/H}]$ to the various subsamples in Figure 14. Very wide EBs with $P = 100$–1000 days also display the same anticorrelation between metallicity and EB fraction (magenta histogram). The fraction of F3V–K3V *Kepler* stars that are EBs with $P = 100$–1000 days decreases from $0.14\% \pm 0.03\%$ across $-1.0 < [{\rm Fe/H}] < -0.5$ to $0.05\% \pm 0.01\%$ across $0.0 < [{\rm Fe/H}] < +0.5$ at the 2.9σ significance level. The consistency in the metallicity trends suggests that the fractions of very close binaries ($P < 7$ days) and binaries with intermediate periods ($P = 100$–1000 days) decrease with metallicity at the same rate. In other words, the overall close binary fraction of solar-type stars strongly decreases with metallicity, but the underlying period distribution below $P \lesssim 1000$ days is metallicity invariant.

In Figure 14, we also display the EB fraction for our *Kepler* sample of F3V–K3V stars with measured spectroscopic metallicities (thick black histogram). For this sample, the EB fraction decreases by a factor of ≈3.5 from $1.4\% \pm 0.4\%$ near $[{\rm Fe/H}] = -0.6$ to $0.4\% \pm 0.2\%$ at $[{\rm Fe/H}] = +0.4$. Attempting to fit a constant EB fraction to the five black metallicity bins in Figure 14 results in a reduced $\chi^2/\nu = 4.2$ with $\nu = 4$ degrees of freedom, which can be rejected with 2.9σ confidence ($p = 0.0019$). The *Kepler* sample of solar-type dwarfs with measured spectroscopic metallicities is fully consistent with the relation $\log F_{\rm EB} \propto -0.39[{\rm Fe/H}]$ inferred from our photometric sample. The EB fractions based on our photometric and spectroscopic samples are nearly identical for both subsolar metallicities $[{\rm Fe/H}] = -0.5$ ($F_{\rm EB} \approx 1.3\%$) and supersolar metallicities $[{\rm Fe/H}] = +0.3$ ($F_{\rm EB} \approx 0.6\%$). Our *Kepler* sample with spectroscopic metallicities is unfortunately too small to further divide according to spectral type or period. Nevertheless, the consistency between our overall photometric and spectroscopic EB fractions suggests that the trends in period and spectral type found within our photometric sample are statistically accurate.

We perform additional K-S tests to determine if the period and mass-ratio distributions of EBs within our photometric sample vary with metallicity. We compare the 226 solar-type EBs with photometric metallicities $-1.7 < [{\rm Fe/H}] < -0.5$ to the 154 EBs with $0.0 < [{\rm Fe/H}] < 0.5$. The EB fraction of our metal-poor sample ($F_{\rm EB} = 1.60\% \pm 0.11\%$) is ≈3.0 times the EB fraction of the metal-rich sample ($F_{\rm EB} = 0.54\% \pm 0.04\%$) at the 9.2σ significance level, consistent with the green histogram in Figure 14. In Figure 15, we plot the measured primary eclipse depths $d_{\rm p}$ as a function of orbital period P for both our metal-poor and metal-rich photometric samples.

Across the full period interval $P = 1$–1000 days, the metal-poor and metal-rich EBs have marginally consistent period distributions at the 1.8σ level ($p_{\rm K\text{-}S} = 0.065$). Metal-poor systems with $[{\rm Fe/H}] < -1.0$, which are likely to be old halo or

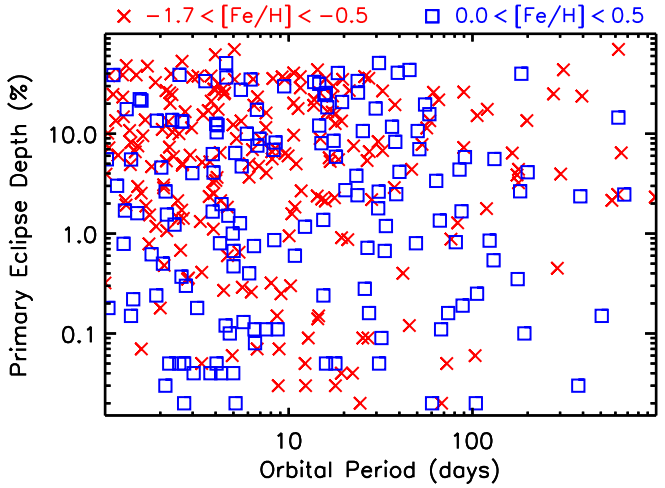

Figure 15. Measured eclipse depths vs. orbital periods for the 226 metal-poor EBs ($-1.7 < [\mathrm{Fe/H}] < -0.5$; red crosses) and 154 metal-rich EBs ($0.0 < [\mathrm{Fe/H}] < 0.5$; blue squares) within our photometric sample of solar-type dwarfs. Our younger, metal-rich sample exhibits a statistically significant excess of eccentric heartbeat binaries and contamination by transiting planets toward short periods $P < 10$ days and small amplitudes $d_\mathrm{p} < 0.2\%$. Outside this parameter space, the two samples have consistent period and eclipse depth distributions. Although the close binary fraction is anticorrelated with metallicity, the period and mass-ratio distributions of close solar-type binaries are metallicity invariant.

thick-disk stars, may exhibit a slight deficit of long-period EBs with $P = 100$–1000 days. In Section 5.3, we attribute this to tidal evolution toward smaller eccentricities and hence a smaller probability of producing eclipses, rather than a shift in the period distribution. In any case, it is only a 1.8σ effect. The 188 metal-poor EBs and 112 metal-rich EBs with $P = 1$–30 days, which all have small enough eccentricities to negligibly affect the eclipse probabilities, exhibit nearly the same period distribution ($p_\mathrm{K\text{-}S} = 0.72$).

The primary eclipse depth distribution maps to the mass-ratio distribution (Moe & Di Stefano 2013). For MS components, EBs with deep eclipses, $d_\mathrm{p} > 25\%$, must have large mass ratios, $q \gtrsim 0.7$. The EBs with shallower eclipses, $d_\mathrm{p} = 1\%$–25%, may have large companions in grazing, inclined orbits but more likely contain small, low-mass companions. In general, systems with $d_\mathrm{p} < 1\%$ include not only true EBs but also ellipsoidal binaries, transiting planets, and heartbeat stars, which are eccentric binaries that induce tidal distortions and dynamical oscillations near periastron (Thompson et al. 2012).

A K-S test demonstrates that the eclipse depth distributions of our metal-poor and metal-rich subsamples are inconsistent with each other at the 3.7σ significance level ($p_\mathrm{K\text{-}S} = 1.3 \times 10^{-4}$). As shown in Figure 15, our metal-rich subsample exhibits an excess of EBs with short periods $P < 10$ days and shallow eclipses $d_\mathrm{p} < 0.2\%$. We inspected the individual light curves of these 22 systems and found that most were not true EBs. Three were ellipsoidal binaries showing sinusoidal light curves. Eight exhibited peculiar nonsinusoidal variability, six of which were flagged as heartbeat stars by Kirk et al. (2016). An additional six did not have definitive secondary eclipses indicative of a transiting planet, four of which were flagged by Kirk et al. (2016) as also having flat-bottomed primary eclipses. Flat-bottomed eclipses further suggest that they are transiting planets as opposed to grazing EBs. Only five of the metal-rich systems with short periods and small amplitudes appear to be genuine EBs. Heartbeat binaries with $P < 10$ days are likely to be relatively young, and therefore metal-rich, to still be eccentric enough to induce strong tidal distortions at periastron (Shporer et al. 2016). Hot Jupiters, Neptunes, and super-Earths with $P < 10$ days are all significantly weighted toward metal-rich hosts with $[\mathrm{Fe/H}] > 0.0$ (Fischer & Valenti 2005; Mulders et al. 2016; Owen & Murray-Clay 2018; Petigura et al. 2018). It is therefore not surprising that our metal-rich EB sample is contaminated more by both heartbeat stars and transiting planets. This provides further confirmation that the photometric metallicities from Huber et al. (2014) can reliably distinguish metal-poor from metal-rich systems.

We therefore restrict our eclipse depth analysis to the 171 metal-poor and 91 metal-rich systems with $d_\mathrm{p} > 1.0\%$ that are most likely genuine EBs. For $d_\mathrm{p} > 1.0\%$, the EB fraction of our metal-poor sample ($F_\mathrm{EB} = 1.20\% \pm 0.09\%$) is $\approx$3.6 times the EB fraction of the metal-rich sample ($F_\mathrm{EB} = 0.33\% \pm 0.03\%$) at the 8.8σ level. Focusing on genuine EBs with deeper eclipses accentuates the anticorrelation between the EB fraction and metallicity. The metal-poor and metal-rich EBs have eclipse depth distributions above $d_\mathrm{p} > 1.0\%$ that are fully consistent with each other ($p_\mathrm{K\text{-}S} = 0.52$). Although the close binary fraction decreases significantly with metallicity, both the period and mass-ratio distributions of close solar-type binaries are metallicity invariant.

5.3. Corrections for Selection Effects

We calculate the eclipse probabilities p_EB to recover the intrinsic close binary fraction from the observed EB fraction. For the full *Kepler* EB sample, Kirk et al. (2016) utilized the stellar radii reported in the *Kepler* input catalog (Brown et al. 2011) to calculate p_EB as a function of period (see their Figure 11). Across $P \approx 3$–20 days, Kirk et al. (2016) found that the eclipse probabilities decrease from $p_\mathrm{EB} \approx 0.17$ to 0.05, as expected from the geometry of circular orbits, i.e., $p_\mathrm{EB} = (R_1+R_2)/a$. Toward very short periods, $P < 3$ days, noneclipsing ellipsoidal binaries are detected across a wider range of inclinations compared to true EBs.

Toward longer periods, $P > 20$ days, three additional effects modify the eclipse probabilities. First, the majority of solar-type binaries with $P > 20$ days are in eccentric orbits with $e > 0.3$ (Meibom & Mathieu 2005; Raghavan et al. 2010; Tokovinin 2014; Moe & Di Stefano 2017). For an eccentric binary, there are certain combinations of inclination and argument of periastron such that there is only one eclipse per orbit (Moe & Di Stefano 2015). In these cases, the projected separation at the conjunction closest to periastron is small enough to produce an eclipse, while the projected separation at the conjunction nearest apastron is too wide. Kirk et al. (2016) included EBs with only one eclipse per orbit in their catalog, so the probability of detecting eccentric EBs is larger than that of their circular counterparts. Second, the main *Kepler* mission observed continuously for 17 $\approx$90 day quarters, with small gaps between the quarters to roll the spacecraft. A nonnegligible fraction of *Kepler* stars fell in the chip gaps or on bad pixels during one or multiple quarters. Some EBs with long periods were therefore missed due to the duty cycle of the *Kepler* observations. Finally, EBs with especially long periods, $P \gtrsim 500$ days, were difficult to detect given the 4 yr time span of the main *Kepler* mission. Kirk et al. (2016) estimated that

only ≈20% of *Kepler* EBs with $P \approx 1000$ days were actually identified.

Kirk et al. (2016) measured $p_{\rm EB}(P)$ for the full *Kepler* sample by averaging across various stellar and orbital properties. Our culled *Kepler* sample contains exclusively solar-type dwarfs, which are, on average, smaller than the mean radii of *Kepler* stars as a whole. Most importantly, stellar radii depend on metallicity, so we must account for the eclipse probabilities as a continuous function of metallicity. We therefore utilize a Monte Carlo technique to calculate $p_{\rm EB}(P, T_{\rm eff}, {\rm [Fe/H]})$ for our *Kepler* sample of solar-type dwarfs. For a given combination of $T_{\rm eff}$ and [Fe/H], we estimate the primary mass M_1 and radius R_1 from the Dartmouth stellar evolutionary tracks (Dotter et al. 2008). We adopt an age–metallicity relation, as done in Section 5.1.1 and Figure 12. Specifically, stars with [Fe/H] > 0.2 have ages $\tau_* = 2$ Gyr, stars with [Fe/H] < −1.3 are $\tau_* = 11$ Gyr old, and we linearly interpolate between these two regimes.

In the previous sections, we adopted a uniform mass-ratio distribution, which adequately describes the overall population of close solar-type binaries with $a \lesssim 10$ au. However, the majority of *Kepler* EBs have very short periods, $P < 10$ days ($a \lesssim 0.1$ au). Very close solar-type binaries exhibit an excess fraction of twins with $q = 0.95$–1.00 (Tokovinin 2000; Moe & Di Stefano 2017). We therefore adopt a twin fraction that decreases linearly with respect to $\log P$ from $F_{\rm twin} = 0.30$ at $\log P({\rm days}) = 0$ to $F_{\rm twin} = 0.15$ at $\log P = 3$. We generate a fraction $F_{\rm twin}$ of binaries to be uniformly distributed across $q = 0.95$–1.00, while the remaining fraction $1 - F_{\rm twin}$ of binaries are uniformly distributed across $q = 0.10$–0.95. We then select M_2 and R_2 from the Dartmouth tracks accordingly.

We adopt circular orbits below $P < P_{\rm circ} = 10$ days and a uniform eccentricity distribution across $0 < e < e_{\rm max}(P)$ toward longer periods (see Equation (1)). We assume random orientations so that the arguments of periastron ω follow a uniform distribution. The eclipse probability at superior and inferior conjunction is $p_{\rm sup,inf} = (R_1+R_2)(1 \pm e\sin\omega)/[a(1-e^2)]$ (Kirk et al. 2016). By requiring only one eclipse per orbit, we adopt the larger of the two eclipse probabilities. According to our Monte Carlo model, a population of wide binaries with $P = 1000$ days that are evenly distributed across $0 < e < e_{\rm max} = 0.98$ are ≈3.3 times more likely to produce eclipses than binaries in circular orbits.

Due to the $(1-e^2)$ term in the denominator of the eclipse probability, the frequency of highly eccentric, long-period binaries with $e > 0.9$ and $P > 100$ days strongly affects the inferred close binary fraction. In Section 5.2, we noticed a small 1.8σ discrepancy whereby our metal-poor sample exhibited a slight deficit of long-period EBs, possibly due to tidal evolution. The population of solar-type binaries in the old, metal-poor halo indeed has a slightly longer circularization period of $P_{\rm circ} \approx 15$ days (Meibom & Mathieu 2005). Adopting a longer circularization period for our metal-poor simulations would reduce the eclipse probabilities and increase the inferred close binary fraction, thereby strengthening our main conclusion. However, tidal evolution of binaries with long periods and large eccentricities is highly uncertain (Moe & Kratter 2018). We therefore adopt $P_{\rm circ} = 10$ days for all metallicities and compare the corrected close binary fractions inferred from the population of EBs with $P < 1000$ and 100 days (see below).

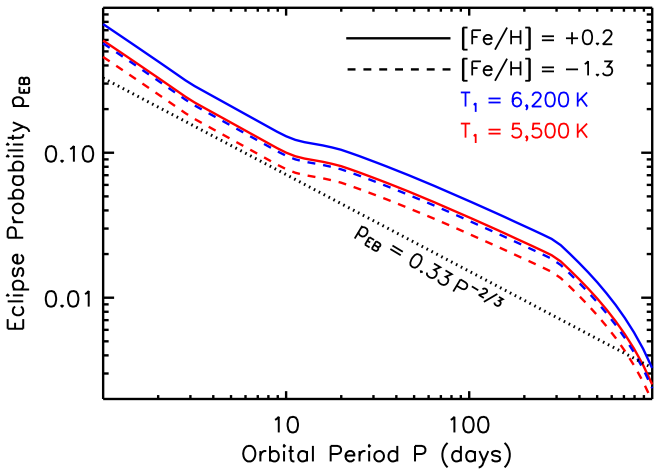

Figure 16. Eclipse probabilities $p_{\rm EB}$ of solar-type binaries as a function of orbital period for metallicities [Fe/H] = −1.3 (dashed lines) and +0.2 (solid lines) and primary temperatures $T_{\rm eff} = 5500$ K (red) and 6200 K (blue). We also show the eclipse probability $p_{\rm EB} = 0.33(P/{\rm day})^{-2/3}$ based solely on geometrical selection effects for a solar-metallicity binary with $M_1 = 1\,M_\odot$, $M_2 = 0.5\,M_\odot$, and $e = 0.0$ (dotted line). Compared to this simple power-law approximation, ellipsoidal variability and Malmquist bias increase $p_{\rm EB}$ at short periods, eccentric orbits further increase $p_{\rm EB}$ across intermediate periods, and the duty cycle and 4 yr time span of the *Kepler* observations reduce $p_{\rm EB}$ toward long periods.

For $P = 3$–20 days, the eclipse probabilities $p_{\rm EB}$ are completely described by the geometry of the orbits. Toward shorter periods, we account for the enhanced probability of detecting ellipsoidal binaries, whereby $p_{\rm EB}$ reaches 1.2 times the pure eclipse probability at $P = 1$ day. Toward longer periods, we assume that the probabilities are suppressed by a reduction factor of 80% at $P = 300$ days and 20% at $P = 1000$ days to correct for the duty cycle and 4 yr time span of the *Kepler* observations (see Figure 11 in Kirk et al. 2016). We linearly interpolate these correction factors with respect to $\log P$.

Because a significant fraction of very close EBs are twins, we must also account for Malmquist bias. Given the same magnitude limit, twin binaries are observed up to $\sqrt{2} \approx 1.4$ times the distance and therefore overrepresented by a factor of $2^{\frac{3}{2}} \approx 2.8$ compared to a volume-limited sample. We weight $p_{\rm EB}$ according to the combined luminosities L_1+L_2 so that twin binaries have 2.8 times the probability of single stars and binaries with faint companions.

We present our results for $p_{\rm EB}(P, T_{\rm eff}, {\rm [Fe/H]})$ in Figure 16 for the same combinations of primary temperatures $T_{\rm eff} = 5500$ and 6200 K and metallicities [Fe/H] = −1.3 and +0.2 investigated in Section 5.1.1 and Figure 12. The eclipse probabilities dramatically decrease with orbital period as expected, but there are also noticeable variations with respect to metallicity and primary temperature. Given the same metallicity, F dwarfs are larger than G dwarfs, so the eclipse probabilities of binaries containing $T_{\rm eff} = 6200$ K primaries are ≈20%–30% larger than those with $T_{\rm eff} = 5500$ K. Similarly, metal-rich dwarfs are larger, given the same effective temperatures, so the eclipse probabilities of metal-rich binaries with [Fe/H] = 0.2 are ≈25%–30% larger than those of metal-poor binaries with [Fe/H] = −1.3.

For comparison, we also display in Figure 16 the eclipse probabilities $p_{\rm EB}(P)$ for a solar-metallicity binary with

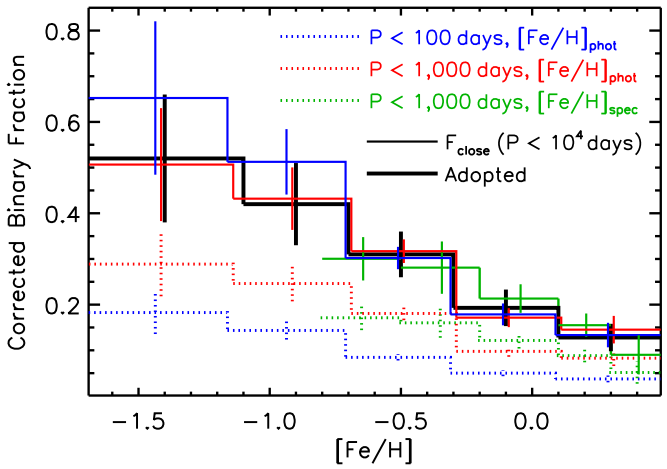

Figure 17. As a function of metallicity, the corrected binary fraction $F_{P<1000\ \mathrm{days}}$ below $P < 1000$ days for our photometric (dotted red line) and spectroscopic (dotted green line) samples of *Kepler* solar-type dwarfs and the corrected binary fraction $F_{P<100\ \mathrm{days}}$ below $P < 100$ days for the photometric sample (dotted blue line). We divide $F_{P<1000\ \mathrm{days}}$ and $F_{P<100\ \mathrm{days}}$ by 0.57 and 0.27, respectively, to recover the intrinsic close binary fraction F_{close} below $P < 10^4$ days (solid colored histograms). All three histograms for F_{close} are consistent with each other, so we adopt a moving weighted average (thick black line) that decreases from $F_{\mathrm{close}} = 52\% \pm 14\%$ across $-1.7 < [\mathrm{Fe/H}] < -1.1$ to $F_{\mathrm{close}} = 13\% \pm 3\%$ across $0.1 < [\mathrm{Fe/H}] < 0.5$.

$M_1 = 1.0\,M_\odot$, $M_2 = 0.5\,M_\odot$, and $e = 0.0$. In this case, we do not account for ellipsoidal variability, Malmquist bias, or the duty cycle of the *Kepler* observations; therefore, the eclipse probabilities follow $p_{\mathrm{EB}} = 0.33(P\,[\mathrm{day}])^{-2/3}$. Toward very short periods, $P < 10$ days, the Malmquist bias associated with the excess twin population substantially elevates the true eclipse probabilities above the simple model. Across intermediate periods, $P \approx 10$–300 days, eccentric EBs further increase p_{EB}. Only toward the longest periods do the duty cycle and time span of the *Kepler* observations reduce p_{EB} below the simple power-law approximation.

For each EB, we compute the eclipse probability $p_{\mathrm{EB}}(P, T_{\mathrm{eff}}, [\mathrm{Fe/H}])$ based on its measured period, primary temperature, and metallicity. We calculate the corrected binary fraction below $P < 1000$ days by summing the inverse of the eclipse probabilities p_{EB} for both our photometric and spectroscopic samples according to the metallicity intervals investigated in Figure 14. Specifically, we measure

$$F_{P<1000\ \mathrm{days}}([\mathrm{Fe/H}]) = \frac{1}{N([\mathrm{Fe/H}])} \times \sum_{i}^{N_{\mathrm{EB}}([\mathrm{Fe/H}])} \frac{1}{p_{\mathrm{EB},i}(P_i,\, T_{\mathrm{eff},i},\, [\mathrm{Fe/H}]_i)}, \quad (2)$$

where $N([\mathrm{Fe/H}])$ is the total number of solar-type dwarfs in a specific metallicity interval and $N_{\mathrm{EB}}([\mathrm{Fe/H}])$ is the number of those stars that have eclipsing companions across $P = 1$–1000 days. We perform jackknife resamplings of our systems to measure the uncertainties in $F_{P<1000\ \mathrm{days}}([\mathrm{Fe/H}])$.

We present $F_{P<1000\ \mathrm{days}}([\mathrm{Fe/H}])$ for both our photometric and spectroscopic samples of *Kepler* solar-type dwarfs in Figure 17 (dotted red and green histograms, respectively). According to our sample with photometric metallicities, the corrected binary fraction below $P < 1000$ days decreases from $F_{P<1000\ \mathrm{days}} = 0.29 \pm 0.07$ near $[\mathrm{Fe/H}] = -1.4$ to $F_{P<1000\ \mathrm{days}} = 0.08 \pm 0.02$ at $[\mathrm{Fe/H}] = 0.3$. The *Kepler* sample with spectroscopic metallicities exhibits a consistent trend, whereby the corrected binary fraction decreases from $F_{P<1000\ \mathrm{days}} = 0.17 \pm 0.03$ near $[\mathrm{Fe/H}] = -0.6$ to $F_{P<1000\ \mathrm{days}} = 0.05 \pm 0.02$ at $[\mathrm{Fe/H}] = 0.4$. The *Kepler* sample of EBs with $P = 100$–1000 days is relatively small, and the uncertainties in their eclipse probabilities may be relatively large (see above). For our *Kepler* sample with photometric metallicities, we therefore also compute $F_{P<100\ \mathrm{days}}([\mathrm{Fe/H}])$ by summing p_{EB}^{-1} for only those EBs with $P = 1$–100 days. The resulting corrected binary fraction below $P < 100$ days decreases from $F_{P<100\ \mathrm{days}} = 0.18 \pm 0.05$ near $[\mathrm{Fe/H}] = -1.4$ to $F_{P<100\ \mathrm{days}} = 0.04 \pm 0.01$ at $[\mathrm{Fe/H}] = 0.3$ (dotted blue histogram in Figure 17).

According to our adopted short-end tail of a lognormal period distribution, 57% of close solar-type binaries with $P < 10^4$ days have $P < 1000$ days. We therefore divide $F_{P<1000\ \mathrm{days}}$ by 0.57 to recover the intrinsic close binary fraction F_{close}. Similarly, 27% of close solar-type binaries have short periods, $P < 100$ days, so we divide $F_{P<100\ \mathrm{days}}$ by 0.27 to measure F_{close}. The three methods for measuring F_{close} from the *Kepler* sample of solar-type EBs are all consistent with each other (see thin colored histograms in Figure 17). The consistency between our photometric and spectroscopic samples further demonstrates that the metallicities of our *Kepler* solar-type dwarfs are sufficiently calibrated to reliably measure $F_{\mathrm{close}}([\mathrm{Fe/H}])$. In addition, the similarity in F_{close} inferred from $F_{P<1000\ \mathrm{days}}$ and $F_{P<100\ \mathrm{days}}$ confirms that both metal-poor and metal-rich solar-type binaries follow the same short-end tail of a lognormal period distribution.

We calculate a moving weighted average utilizing the three histograms for $F_{\mathrm{close}}([\mathrm{Fe/H}])$ in Figure 17. We adopt the measurement uncertainties according to the photometric sample of EBs with $P = 1$–1000 days. Given the model uncertainties in the eclipse probabilities p_{EB} and the extension of the period distribution beyond $P > 1000$ days, we also add a systematic uncertainty of $\delta F_{\mathrm{close}}/F_{\mathrm{close}} = 15\%$ in quadrature with the measurement uncertainties. We show our final $F_{\mathrm{close}}([\mathrm{Fe/H}])$ based on *Kepler* EBs as the thick black histogram in Figure 17. The corrected close binary fraction decreases from $F_{\mathrm{close}} = 0.52 \pm 0.14$ for $[\mathrm{Fe/H}] = -1.4 \pm 0.3$ to $F_{\mathrm{close}} = 0.13 \pm 0.03$ for $[\mathrm{Fe/H}] = 0.3 \pm 0.2$. The relative decrease in the corrected close binary fraction ($0.52/0.13 = 4.0$) is slightly larger than the decrease in the observed EB fraction (factor of 3.4 across the same metallicity interval; see Section 5.2). This is because the eclipse probabilities of metal-poor binaries are smaller (see above and Figure 16), so their intrinsic close binary fractions are even larger. Correcting for incompleteness further strengthens our conclusion that the close binary fraction of solar-type stars decreases with metallicity.

6. Summary of Observational Constraints

6.1. Close Binary Fraction of Solar-type Stars

A variety of observational techniques all confirm that the close binary fraction of solar-type stars dramatically decreases with metallicity. In Figure 18, we display the bias-corrected close binary fraction F_{close} across $\log P(\mathrm{days}) = 0$–$4$ ($a \lesssim 10$ au) as a function of metallicity determined from SBs in the Carney–Latham survey of high proper motion stars (Section 3.1), SBs in samples of metal-poor giants (Section 3.2), RV variables in the APOGEE survey of

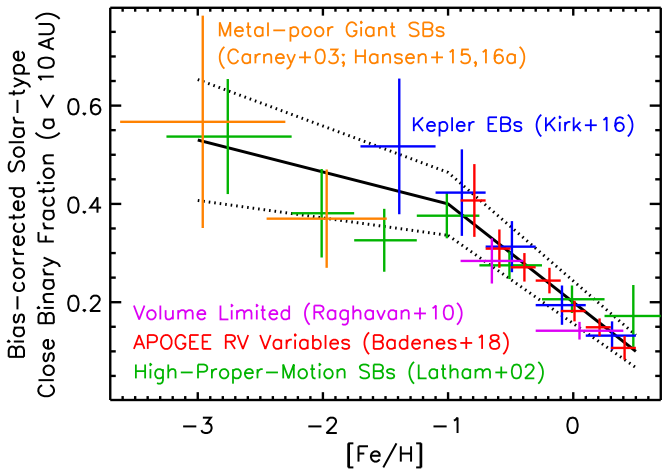

Figure 18. Intrinsic close binary fraction ($P < 10^4$ days; $a < 10$ au) of $M_1 \approx 1\,M_\odot$ primaries as a function of metallicity after correcting for incompleteness and other selection biases. We compare the measurements from (1) SBs in samples of metal-poor giants (orange), (2) *Kepler* EBs with solar-type dwarf primaries (blue), (3) a volume-limited sample of solar-type primaries (magenta), (4) RV variables in the APOGEE survey of GK IV/V stars (red), and (5) SBs in the Carney–Latham survey of high proper motion stars (green). All five samples/methods show a consistent metallicity trend that can be fitted by two line segments (black) in which the close binary fraction decreases from $F_{\rm close} = 53\% \pm 12\%$ at [Fe/H] $= -3.0$ to $F_{\rm close} = 40\% \pm 6\%$ at [Fe/H] $= -1.0$ and then to $F_{\rm close} = 10\% \pm 3\%$ at [Fe/H] $= +0.5$. Even after accounting for systematic uncertainties, the close binary fraction of solar-type stars is anticorrelated with metallicity at the $\approx 9\sigma$ significance level.

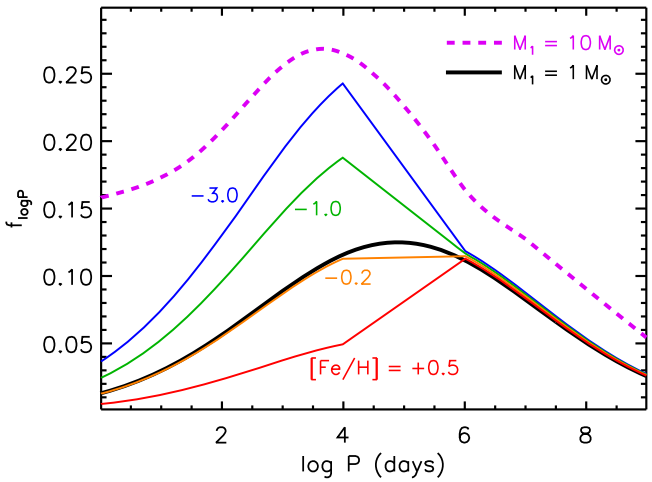

Figure 19. Frequency $f_{\log P}$ of stellar companions per decade of orbital period. We compare the canonical lognormal period distribution of solar-type multiples in the solar neighborhood (black line) to the companion distribution of early-B stars (dashed magenta line). We also show the metallicity-dependent period distributions for solar-type primaries with [Fe/H] $= -3.0$ (blue), -1.0 (green), -0.2 (orange), and $+0.5$ (red). The close binary fraction ($\log P < 4$; $a < 10$ au) of solar-type stars is significantly anticorrelated with metallicity, while the frequency of wide companions ($\log P > 6$; $a > 200$ au) is metallicity invariant. As solar-type stars decrease in metallicity, both their binary fraction and binary period distribution approach that of early-B stars.

GK IV/V stars (Section 4), and *Kepler* EBs with F3V–K3V primaries (Section 5). Based on the Raghavan et al. (2010) volume-limited sample of solar-type stars, we also showed in Section 2 that the binary fraction below $\log P(\text{days}) < 6$ ($a \lesssim 200$ au) is $50\% \pm 8\%$ across $-0.9 <$ [Fe/H] < -0.4 and $25\% \pm 2\%$ across $-0.3 <$ [Fe/H] < 0.4. According to our adopted lognormal period distribution, 55% of binaries below $\log P(\text{days}) < 6$ are close binaries with $\log P(\text{days}) < 4$. This provides close binary fractions of $F_{\rm close} = 28\% \pm 5\%$ and $14\% \pm 2\%$ across $-0.9 <$ [Fe/H] < -0.4 and $-0.3 <$ [Fe/H] < 0.4, respectively, which we also show in Figure 18.

All five samples/methods presented in Figure 18 exhibit a quantitatively consistent anticorrelation between $F_{\rm close}$ and [Fe/H]. Because of the different methods used to identify binaries in the various samples, it is difficult for them to conspire to produce consistent results erroneously. The error bars for each of the data points in Figure 18 incorporate not only the measurement uncertainties according to their respective sample sizes but also the systematic uncertainties in transforming the observed (incomplete) close binary fractions into intrinsic bias-corrected close binary fractions. Attempting to fit a constant $F_{\rm close}$ to the 23 independent measurements in Figure 18 results in a reduced $\chi^2/\nu = 6.2$ with $\nu = 22$ degrees of freedom. Even after considering systematic uncertainties, we can reject the null hypothesis that the close binary fraction of solar-type stars is invariant with respect to metallicity at the 8.7σ significance level ($p = 2.2 \times 10^{-18}$).

We instead adopt a weighted moving average for $F_{\rm close}$([Fe/H]) that can be accurately fitted by two line segments. The corrected close binary fraction of solar-type stars decreases from $F_{\rm close} = 53\% \pm 12\%$ at [Fe/H] $= -3.0$ to $F_{\rm close} = 40\% \pm 6\%$ at [Fe/H] $= -1.0$ and then to $F_{\rm close} = 10\% \pm 3\%$ at [Fe/H] $= +0.5$. We display our two-segment fit to the various observations in Figure 18. Across the full metallicity interval $-3.0 <$ [Fe/H] < 0.5, the close binary fraction of solar-type stars decreases by a factor of ≈ 5. Metal-poor halo stars clearly have a higher close binary fraction than metal-rich disk stars. Most of the variation in $F_{\rm close}$ occurs across the narrower interval $-1.0 <$ [Fe/H] < 0.5, whereby the close binary fraction decreases by a factor of ≈ 4. Even within the galactic disk, the close binary fraction of solar-type stars decreases dramatically with metallicity. By interpolating our fit at the mean metallicity of the field, i.e., [Fe/H] ≈ -0.2, we measure a close binary fraction of $F_{\rm close} = 24\% \pm 4\%$. This matches the close binary fraction inferred from volume-limited samples of solar-type stars in the solar neighborhood (Duquennoy & Mayor 1991; Raghavan et al. 2010; Tokovinin 2014; Moe & Di Stefano 2017).

6.2. Binary Period Distributions

Solar-type binaries in the field follow a lognormal companion period distribution that peaks at $\log P(\text{days}) = 4.9$ ($a_{\rm peak} \approx 40$ au) with a dispersion of $\sigma_{\log P} = 2.3$ (Duquennoy & Mayor 1991; Raghavan et al. 2010; Tokovinin 2014). After making small corrections for incompleteness (Chini et al. 2014; Moe & Di Stefano 2017), the single-, binary-, triple-, and quadruple-star fractions are $F_{\rm single} \approx 51\%$, $F_{\rm binary} \approx 34\%$, $F_{\rm triple} \approx 12\%$, and $F_{\rm quadruple} \approx 3\%$, respectively. These fractions provide the average multiplicity frequency of companions per primary of $f_{\rm mult} = F_{\rm binary} + 2F_{\rm triple} + 3F_{\rm quadruple} = 0.67 \pm 0.05$. We define the frequency $f_{\log P}$ of stellar companions per decade of orbital period such that

$$f_{\rm mult} = \int_0^9 f_{\log P}\, d\log P. \quad (3)$$

In Figure 19, we plot the lognormal period distribution $f_{\log P}$ of solar-type multiples in the solar neighborhood scaled to $f_{\rm mult} = 0.67$ across $\log P(\text{days}) = 0$–9 (black line).

We found five lines of evidence that the period distribution of solar-type binaries across $\log P(\mathrm{days}) = 0$–4 ($a < 10$ au) is relatively independent of metallicity but simply scales according to F_{close}. First, the anticorrelation between the SB fraction and metallicity occurs across a broad range of periods, $P = 20$–2000 days (Figure 2). Second, the RV variability fraction decreases with metallicity at the same rate for both close companions to GK dwarfs and wide companions orbiting giants (see Figure 8 and Badenes et al. 2018). Third, the observed distribution of RV amplitudes across $\Delta \mathrm{RV}_{\mathrm{max}} = 1$–$10\,\mathrm{km\,s^{-1}}$ is independent of metallicity and consistent with the short-period tail of our adopted lognormal period distribution (Section 4). Fourth, the same anticorrelation between the *Kepler* EB fraction and metallicity is observed across a wide range of periods, $P \approx 1$–1000 days (Figure 14). Finally, both metal-poor and metal-rich *Kepler* EBs have the same period and eclipse depth distributions, suggesting that the period and mass-ratio distributions of close solar-type binaries are metallicity invariant (Figure 15). In Figure 19, we display the short-period tail ($\log P = 0$–4) of our adopted lognormal period distribution scaled to F_{close} for the four metallicities [Fe/H] $= -3.0$, -1.0, -0.2, and $+0.5$ evaluated above (solid colored curves).

Meanwhile, as discussed in Section 2, observations of visual and common proper motion binaries demonstrate that the wide binary fraction of solar-type stars is relatively independent of metallicity (Chanamé & Gould 2004; Zapatero Osorio & Martín 2004; El-Badry & Rix 2019). We also showed in Section 2 that the frequency of wide companions with $\log P$ (days) > 6 ($a \gtrsim 200$ au) in the Raghavan et al. (2010) sample is independent of metallicity. Based on volume-limited samples of solar-type stars (Duquennoy & Mayor 1991; Raghavan et al. 2010; Tokovinin 2014), and after making small corrections for incompleteness (Chini et al. 2014; Moe & Di Stefano 2017), we estimate that the frequency of companions across $\log P$ (days) $= 6$–9 ($a = 200$–20,000 au) is $f_{\mathrm{wide}} = 0.21 \pm 0.03$. As shown in Figure 19, the long-period tail of companions to solar-type stars follows our adopted lognormal period distribution scaled to $f_{\mathrm{wide}} = 0.21$ across $\log P(\mathrm{days}) = 6$–9, independent of metallicity.

There is a transition region across intermediate periods of $\log P(\mathrm{days}) = 4$–6 ($a \approx 10$–200 au). For simplicity, we linearly interpolate the period distribution with respect to $\log P$ between close binaries ($\log P < 4$) that exhibit a strong metallicity dependence and very wide binaries ($\log P > 6$) that are metallicity invariant. Our distribution for [Fe/H] $= -0.2$ in Figure 19 nearly coincides with the lognormal distribution of solar-type binaries in the solar neighborhood, which also have $\langle$[Fe/H]$\rangle \approx -0.2$. Metal-poor solar-type binaries peak at $\log P(\mathrm{day}) \approx 4$ ($a_{\mathrm{peak}} \approx 10$ au), while solar-type binaries with supersolar metallicity peak at $\log P(\mathrm{day}) \approx 6$ ($a_{\mathrm{peak}} \approx 200$ au). This is consistent with the results in Rastegaev (2010), who also found that metal-poor solar-type binaries peak at shorter separations compared to solar-type binaries in the solar neighborhood. El-Badry & Rix (2019) also recently demonstrated that an anticorrelation between metallicity and the solar-type binary fraction begins to emerge below $a \lesssim 200$ au. Specifically, they measured that the ratio in the binary fraction for [Fe/H] $= -1.0$ versus [Fe/H] $= 0.5$ solar-type stars increases from $R = F([\mathrm{Fe/H}] = -1.0)/F([\mathrm{Fe/H}] = 0.5) \approx 1$ beyond $a > 250$ au, i.e., no metallicity dependence, to $R \approx 3$ at $a \approx 50$ au. These measurements are consistent with our metallicity-dependent period distributions, where we find $R = 1.0$ beyond $a > 200$ au, $R = 2.4$ at $a = 50$ au, and $R = 4.0$ inside of $a < 10$ au.

By integrating $f_{\log P}$, we measure multiplicity frequencies of $f_{\mathrm{mult}} = 1.11$, 0.92, 0.66, and 0.47 for solar-type primaries with [Fe/H] $= -3.0$, -1.0, -0.2, and $+0.5$, respectively. Our [Fe/H] $= -0.2$ multiplicity frequency of $f_{\mathrm{mult}} = 0.66$ nearly matches the measured value of $f_{\mathrm{mult}} = 0.67 \pm 0.05$ for solar-type systems in the field. As the close binary fraction of solar-type stars increases toward smaller metallicities, the triple-star fraction also increases. For solar-type stars in the field, about half of the wide companions are outer tertiaries in hierarchical triples, and the overall triple-/quadruple-star fraction is $F_{\mathrm{triple}} + F_{\mathrm{quadruple}} \approx 15\%$ (Raghavan et al. 2010; Chini et al. 2014; Tokovinin 2014; Moe & Di Stefano 2017). Considering that the close binary fraction doubles toward decreasing metallicity compared to the field population, nearly all wide companions to metal-poor stars are outer tertiaries. A similar effect is observed for massive OB stars, which also have a large close binary fraction (see below), whereby nearly all wide companions ($a \gtrsim 100$ au) are outer tertiaries in triples (Sana et al. 2014; Moe & Di Stefano 2017). Not only are half of the extremely metal-poor solar-type stars in close binaries ($F_{\mathrm{close}} \approx 50\%$), but a substantial fraction are also in triples and quadruples, i.e., $F_{\mathrm{triple}} + F_{\mathrm{quadruple}} \approx 35\%$.

The wide binary fraction of late-type stars depends on age and environment. For example, embedded Class 0 and I protostars exhibit a factor of ≈2–3 excess of wide companions with $a \gtrsim 200$ au compared to the field population (Duchêne et al. 2007; Connelley et al. 2008; Tobin et al. 2016b; Moe & Di Stefano 2017). It is presumed that a significant fraction of such young, wide pairs are dynamically disrupted by the time they reach the zero-age MS. Similarly, T Tauri stars, i.e., slightly older Class II and III protostars, in various star-forming environments such as Taurus, Upper Scorpius, Ophiuchus, and Orion exhibit a factor of ≈2 binary excess across intermediate separations $a \approx 10$–100 au (Ghez et al. 1993; Kraus et al. 2008, 2011; Duchêne et al. 2018). As discussed in Duchêne et al. (2018), a binary excess across such intermediate separations cannot be readily explained in the context of dynamical evolution. Metallicity cannot account for the excess either, as nearby star-forming regions with [Fe/H] ≈ 0.0 have only a marginally higher metallicity than the field ([Fe/H] ≈ -0.2). We would therefore expect young star-forming environments to have an ≈10%–20% deficit of binaries with intermediate separations due to metallicity effects, not a factor of ≈2 excess. The apparent binary excess across $a \approx 10$–100 au in most of the nearby star-forming environments remains a mystery and is the subject of a future study. In contrast, the close ($a < 10$ au) binary fractions of solar-type stars in the field, clusters, and young star-forming environments are all consistent with each other (Mathieu 1994; Melo 2003; Geller & Mathieu 2012; Leiner et al. 2015; Moe & Di Stefano 2017). The close binary fraction therefore depends strictly on primary mass and metallicity, which are inextricably linked to the accretion rates and opacities of their primordial disks (see Section 7).

6.3. Comparison to Massive Binaries

We next investigate the multiplicity properties of early-B stars with $M_1 \approx 6$–$17\,M_\odot$ ($\langle M_1 \rangle \approx 10\,M_\odot$). Moe & Di Stefano (2017) compiled several surveys of early-B MS stars in the

MW and Magellanic Clouds ($-0.7 \lesssim$ [Fe/H] $\lesssim 0.1$) to fit $f_{\log P}$ across all periods (see green and blue data points in their Figure 37). The measured companion frequency is $f_{\log P} \approx 0.15$–0.20 across $\log P(\mathrm{days}) = 0$–$2$, according to observations of spectroscopic (Levato et al. 1987; Abt et al. 1990; Kobulnicky et al. 2014) and eclipsing (Moe & Di Stefano 2013, 2015) early-B binaries. The period distribution then peaks across $\log P(\mathrm{days}) = 3$–$4$ ($a \approx 10$ au) at $f_{\log P} \approx 0.25$–0.30 based on long-baseline interferometry of early-B primaries (Rizzuto et al. 2013) and spectroscopic RV observations of Cepheids, which evolved from early-B primaries (Evans et al. 2015). The frequency then declines to $f_{\log P} \approx 0.10$–0.20 across $\log P(\mathrm{days}) = 5$–$7$ according to adaptive optics, speckle imaging, visual observations, and common proper motion astrometry of wide companions to early-B stars (Abt et al. 1990; Duchêne et al. 2001; Shatsky & Tokovinin 2002; Peter et al. 2012). The dashed magenta curve in Figure 19 is consistent with all of these observational constraints.

Integrating the dashed magenta curve in Figure 19 yields a multiplicity frequency of $f_{\mathrm{mult}} = 1.62$ for $M_1 = 10\,M_\odot$. This is consistent with the value of $f_{\mathrm{mult}} = 1.6 \pm 0.2$ reported in Moe & Di Stefano (2017) for early-B primaries (see their Table 13). Integrating $f_{\log P}$ across $0 < \log P(\mathrm{days}) < 4$ results in a close-companion frequency of $f_{\mathrm{close}} = 0.85$. The majority of these companions are in close binaries; i.e., $F_{\mathrm{close}} = 70\% \pm 11\%$ of $M_1 = 10\,M_\odot$ primaries have stellar companions below $\log P$ (days) < 4. The remaining companions are outer tertiaries in compact triples; i.e., $\approx$15% of $M_1 = 10\,M_\odot$ primaries are in compact triples in which the outer tertiary is below $\log P_{\mathrm{outer}}(\mathrm{days}) < 4$ (see Moe & Di Stefano 2017).

The close binary fraction of early-B primaries ($F_{\mathrm{close}} = 70\% \pm 11\%$) is considerably larger than that of solar-type stars in the field with $\langle$[Fe/H]$\rangle \approx -0.2$ ($24\% \pm 4\%$) but only slightly larger than that of extremely metal-poor FGK stars with [Fe/H] ≈ -3.0 ($53\% \pm 12\%$). The separation distribution of companions to early-B primaries peaks at $a_{\mathrm{peak}} \approx 10$ au (Rizzuto et al. 2013; Evans et al. 2015; Moe & Di Stefano 2017). This is shorter than the peak in the field solar-type binary period distribution ($a_{\mathrm{peak}} \approx 40$ au) but consistent with the peak for metal-poor solar-type binaries ($a_{\mathrm{peak}} \approx 10$ au). As solar-type stars decrease in metallicity, both their binary fraction and binary period distribution approach that of early-B stars (see Figure 19).

We divided our APOGEE RV and *Kepler* EB samples according to spectral type, and we found the same degree of anticorrelation between the close binary fraction and metallicity across a broad range of primary masses $M_1 \approx 0.6$–$1.5\,M_\odot$. Meanwhile, as discussed in Section 2, the multiplicity properties of massive stars are relatively independent of metallicity (Moe & Di Stefano 2013; Dunstall et al. 2015; Almeida et al. 2017). In particular, Moe & Di Stefano (2013) found that the close binary fraction of early-B primaries with $M_1 \approx 6$–$16\,M_\odot$ decreases by less than $\Delta F_{\mathrm{close}}/F_{\mathrm{close}} < 20\%$ across $-0.7 <$ [Fe/H] < 0.1. Across this same metallicity interval, the close binary fraction of solar-type stars decreases by a factor of $\approx$1.9 from $F_{\mathrm{close}} = 34\% \pm 5\%$ to $18\% \pm 4\%$ (see Figure 18). In Section 7, we discuss disk fragmentation models that explain why the close binary fraction of solar-type stars is strongly anticorrelated with metallicity, while the close binary fraction of massive stars is higher but relatively insensitive to metallicity.

6.4. Implications for Binary Evolution

The anticorrelation between metallicity and the close binary fraction of solar-type stars has profound implications for binary evolution. All close solar-type binaries with $P < 10^4$ days ($a \lesssim 10$ au) will interact in some manner, either through Roche-lobe overflow or wind accretion. Companions to blue stragglers have been observed up to $P \approx 3000$ days ($a \approx 5$ au; Mathieu & Geller 2009), companions to barium stars extend to $P \approx 20{,}000$ days ($a \approx 20$ au; Jorissen et al. 1998; Van der Swaelmen et al. 2017), and the widest known symbiotic, Mira, has an orbital period of $P \approx 500$ yr ($a \approx 80$ au; Prieur et al. 2002; Sokoloski & Bildsten 2010). Future studies of blue stragglers, barium stars, cataclysmic variables, novae, and symbiotics must consider the effects of a metallicity-dependent close binary fraction. The merger rate of binary WDs is likely larger in metal-poor environments such as the halo. This predicted variation may possibly be measured by the future gravitational-wave detector *LISA*. The metallicity trend likely extends to intermediate masses of $M_1 \approx 2$–$5\,M_\odot$ (at least to some extent) and therefore is also important for SNe Ia.

More than half of solar-type stars with [Fe/H] $\lesssim -1.0$ will interact with a stellar companion. The fraction of solar-type stars that experience significant binary evolution in metal-poor environments, e.g., the galactic halo, dwarf galaxies, and high-redshift universe, is more than double the fraction in the field. About 20% of stars in the galactic bulge (Ness & Freeman 2016; García Pérez et al. 2018) and most of the stars in the thick disk (Ruchti et al. 2011; Beers et al. 2014) also have [Fe/H] $\lesssim -1.0$ and therefore higher rates of binary interactions. Although the binary fraction in dense globular clusters has significantly evolved due to dynamical interactions, the initial close binary fraction of metal-poor solar-type stars in globular clusters must have been large, consistent with the results of *N*-body simulations (Ivanova et al. 2005). The metallicity distribution of all stars that have ever formed, including the progenitors of compact remnants, are weighted toward lower metallicities than systematically younger stars still on the MS. The number of compact remnants in binaries is therefore larger than previously anticipated due to the larger binary fraction at lower metallicities. For example, $\approx$20% of close solar-type binaries contain WD secondaries (Moe & Di Stefano 2017; Murphy et al. 2018), which is larger than what is predicted by population synthesis studies.

A substantial fraction of metal-poor stars that have recently evolved off the MS, e.g., giants and planetary nebulae (PNe), have been influenced by binary interactions. The IMF is significantly weighted toward low-mass stars (Bastian et al. 2010; Kroupa et al. 2013), and the MW star formation rate was $\approx$3 times larger $\approx$10 Gyr ago than it is now (Governato et al. 2007; De Lucia et al. 2014). Based on the measured IMF and modeled galactic star formation history, we estimate that $\approx$55% of MW giants and PNe have old, solar-type progenitors ($\tau_* > 7$ Gyr, $M \approx 0.8$–$1.2\,M_\odot$). Such old, low-mass giants tend to be metal-poor (Ratnatunga & Yoss 1991; Carollo et al. 2010; Mackereth et al. 2017). The metallicity trend therefore dramatically affects the properties of low-mass evolved stars. For example, the enhanced close binary fraction of metal-poor solar-type stars substantially strengthens the conclusion that the shaping of PN morphologies is the result of binary interactions (Moe & De Marco 2006; De Marco 2009; Jones & Boffin 2017). Providing further corroboration, Badenes et al. (2015) measured the delay-time distribution of bright PNe in

the LMC and discovered two distinct populations of PN progenitors: an old channel ($\tau_* = 5$–8 Gyr) deriving from solar-type stars ($M \approx 1.0$–$1.2\,M_\odot$) and a young channel (35–800 Myr) evolving from late-B/early-A stars (≈ 2–$8\,M_\odot$). According to the measured age–metallicity relation of the LMC (Olszewski et al. 1991; Pagel & Tautvaisiene 1998; Cole et al. 2005; Carrera et al. 2011; Piatti & Geisler 2013), the old, solar-type progenitors are metal-poor ([Fe/H] $\lesssim -1.0$) and hence have a large close binary fraction of $F_{\rm close} = 40\%$–50%. The young progenitors have a higher metallicity of [Fe/H] ≈ -0.4 but are sufficiently massive so that they also have a large close binary fraction of $F_{\rm close} = 40\%$–60%. Meanwhile, evolved stars with intermediate masses ($M \approx 1.2$–$2.0\,M_\odot$) in the LMC have intermediate metallicities and therefore a smaller close binary fraction of $F_{\rm close} \approx 30\%$. If PNe derive from interactions in close binaries, then the variations in $F_{\rm close}$ with respect to mass and metallicity can explain the observed bimodal mass/age distribution of PN progenitors in the LMC.

7. Fragmentation Models

Binary star formation is thought to occur through two primary channels. On large scales, turbulent core fragmentation creates binaries originally separated by 1000 s of au (Fisher 2004; Bate 2009b; Offner et al. 2010). On smaller scales, individual disks around young stars can become unstable due to strong self-gravity and fragment into multiple stellar or sub-stellar mass objects on scales of 10–100 s of au (Adams et al. 1989; Bonnell 1994). Previous work has shown that the enhanced multiplicity of higher-mass stars, particularly at close separations, likely derives from the increased likelihood of disk fragmentation (Kratter & Matzner 2006; Krumholz et al. 2007; Kratter et al. 2008; Moe & Di Stefano 2017; Moe & Kratter 2018). The observed close binary fraction–versus–metallicity anticorrelation (Figure 18) suggests that disk fragmentation should occur more frequently for solar-type protostars as the metallicity decreases. Since the IMF and wide binary fraction do not change within the measurement uncertainties, we expect core fragmentation to be relatively independent of metallicity. We review previous models of the metallicity dependence below and subsequently present a simple argument as to why enhanced disk fragmentation in low-mass protostars should be a consequence of low metallicity.

7.1. Previous Models of Fragmentation at Low Metallicity

Previous models are in tension regarding the effect of metallicity on stellar populations. Given the same initial conditions but varying the metallicity across $-2.0 < \log(Z/Z_\odot) < 0.5$, Bate (2005, 2014) simulated the same IMF, binary fraction, period distribution, and mass-ratio distribution. They concluded that the differences in opacity arising from differences in metallicity have a negligible effect on the processes of protobinary fragmentation and accretion. However, the hydrodynamic simulations conducted by Bate (2005, 2014) had a resolution limit of $\approx$1 au, so they could not directly probe trends with metallicity at very short separations. Moreover, their low-metallicity simulations produced significantly more binary mergers, which might be unresolved close binaries. Most importantly (see below), these papers only changed the opacity from one calculation to the next, not the initial conditions. These simulations also neglected the intrinsic stellar and accretion luminosity of stars, which affects the temperatures, disk masses, and radii at which disk fragmentation occurs (Kratter & Murray-Clay 2011).

Glover & Clark (2012) explored the onset of star formation in molecular clouds across $-2 < \log(Z/Z_\odot) < 0$. As expected, they found that gas temperatures in optically thin cores rise as metallicity declines, thereby increasing the typical Jeans mass. However, they did not report substantial changes in the star formation outcome on large scales. Dopcke et al. (2011, 2013) followed the thermal evolution and fragmentation of collapsing cores as a function of metallicity and concluded that differences only became pronounced at $Z < 10^{-5}\,Z_\odot$. Myers et al. (2011) included the effects of radiative feedback and still found that dust opacity negligibly affects the temperatures and fragmentations of cores as they collapse. Myers et al. (2011) also presented simple analytic models illustrating why the IMF is insensitive to metallicity. Like the Bate (2014) models, the simulations by Myers et al. (2011) and Dopcke et al. (2013) are limited by resolution and therefore cannot reliably characterize disk properties on small scales. Nevertheless, we conclude that their results are robust on large scales. Core fragmentation is relatively independent of metallicity, which is why the observed IMF and wide binary fraction are invariant across $-1.5 \lesssim \log(Z/Z_\odot) < 0.5$.

Machida (2008) and Machida et al. (2009) argued that the alteration of the cloud initial conditions does affect fragmentation on smaller scales. In their low-metallicity models, hotter cloud temperatures translate to larger mass accretion rates, making the disks more susceptible to fragmentation. In their simulations, which cover a broad range of metallicities, $-6 < \log(Z/Z_\odot) < 0$, Machida et al. (2009) found that the binary fraction measurably decreases with metallicity. They also found that the peak in the fragmentation separation transitions from $a_{\rm peak} \approx 1$ au for $Z = 10^{-6}\,Z_\odot$ to $a_{\rm peak} \approx 100$ au for $Z = Z_\odot$.

More recently, Tanaka & Omukai (2014) expanded on these models by studying the changes in protostellar disk properties as a function of metallicity and primary mass. They found that disks of massive protostars ($M_1 \approx 10\,M_\odot$) are gravitationally unstable and susceptible to fragmentation, even at solar metallicity (see their Figure 7). This is consistent with previous models that showed that the likelihood of disk fragmentation increases with final stellar mass as a result of the higher mass accretion rates (Kratter & Matzner 2006; Krumholz et al. 2007; Kratter et al. 2008). At solar metallicity, the observed binary fraction of massive stars is already large, i.e., $\approx$70% below $a < 10$ au and nearly 100% within $a < 100$ au (Sana et al. 2012, 2014; Moe & Di Stefano 2017; Section 6). Decreasing the metallicity can only marginally increase the close binary fraction of massive stars.

For low-mass stars, Tanaka & Omukai (2014) showed that solar-metallicity disks are unlikely to fragment, consistent with previous results (Kratter et al. 2008). Below $Z < 10^{-3}\,Z_\odot$, Tanaka & Omukai (2014) also found that disk fragmentation is more probable due to both increasing infall rates and more efficient disk cooling (see their Figure 7). Similarly, Clark et al. (2011a, 2011b) demonstrated that the disks of primordial Population III stars are highly susceptible to fragmentation. The Machida et al. (2009) and Tanaka & Omukai (2014) models of disk fragmentation are qualitatively consistent with two observed trends: (1) the anticorrelation between the close binary fraction and metallicity of solar-type stars (Figure 18)

and (2) the shift in the binary period distribution toward smaller separations as the metallicity decreases (Figure 19).

Quantitatively, however, there is a large disagreement between the observations and previous simulations. Tanaka & Omukai (2014) found that only extremely metal-poor solar-type stars with $\log(Z/Z_{\odot}) < -3$ are more likely to have experienced disk fragmentation. Meanwhile, we found that the close binary fraction increases by a factor of ≈4 from [Fe/H] = +0.5 to −1.0 and then only slightly increases below [Fe/H] < −1.0 (see Figure 18). We note that Tanaka & Omukai (2014) neglected the impact of protostellar luminosity on disk temperatures and assumed that core radii, and thus disk radii, decrease with decreasing metallicity. For the parameters chosen in their models, low-mass solar-metallicity stars have disk radii of order ≈1000 au, which is large compared to our best observational constraints of ≈100–300 au (Ansdell et al. 2018). In the following, we address these concerns and present our own toy model of disk fragmentation for solar-type stars as a function of metallicity.

7.2. A Simple Model for Disk Fragmentation

Stellar binary formation via disk fragmentation requires the attainment of two conditions. First, the disk must be driven to be strongly self-gravitating, with a Toomre parameter $Q = c_s\Omega/\pi G\Sigma \approx 1$. Second, for gravitational instability to lead to the formation of bound clumps, gas must cool quickly so that the instability does not saturate in a gravitoturbulent state (Kratter & Lodato 2016). We can understand how decreased metallicity leads to enhanced disk fragmentation through the examination of a single dimensionless number,

$$\xi = \frac{G\dot{M}_{\rm in}}{c_{\rm s,d}^3}, \tag{4}$$

where $\dot{M}_{\rm in}$ is the infall rate onto the disk and $c_{\rm s,d}$ is the sound speed in the disk. Kratter et al. (2010a) showed that disk fragmentation becomes prevalent when $\xi \gtrsim 1$, with a weak dependence on cloud angular momentum. In the following, we show that as the metallicity decreases, ξ increases due to the differential influence of metallicity on gas cooling in the optically thin cores versus optically thick disks.

First, consider the scaling of the numerator, $\dot{M}_{\rm in}$. It should scale with the core temperature roughly as $c_{\rm s,c}^3/G$, or core sound speed cubed, which is the characteristic infall rate of an isothermal sphere (Larson 1969; Shu 1977). While real infall rates are not constant in time, the sound speed sets the scale parameter around which excursions of order a few are expected. The ratio $c_{\rm s,d}^3/G$ in Equation (4) parameterizes accretion through a self-gravitating disk. For a steady-state, α-disk model,

$$\dot{M} = 3\pi\nu\Sigma = \frac{3\alpha c_{s,d}^3}{GQ}, \tag{5}$$

where $\nu = \alpha c_s H$. Even when global transport through spiral arm torques is poorly described by simple viscous α models, one still expects that the above equation, evaluated as $\alpha \rightarrow 1$, represents an upper limit to the rate at which material can be processed through the accretion disk. With all other parameters held fixed, we see that $\xi \propto c_{\rm s,c}^3/c_{\rm s,d}^3$. Thus, ξ will increase if core temperatures rise or disk temperatures fall. Lowering the metallicity induces both effects simultaneously.

Metallicity affects star formation by altering the cooling rates of gas. In low-density, optically thin gas, e.g., cores, the removal of metals decreases the cooling rates, leading to systematically higher cloud temperatures and thus infall rates. In contrast, protostellar disks are often optically thick to their own cooling radiation when $Q \sim 1$, at least at metallicities near $Z_{\odot}$. In this limit, gas cools predominantly through coupling with the dust, which radiates efficiently. Reducing the metallicity reduces the dust opacity by changing the gas-to-dust ratio. Thus, when $\tau > 1$, lowering the metallicity reduces the optical depth and thus enhances the disk cooling rates at fixed temperatures and surface densities. In this regime, $c_{\rm s,c}$ rises while $c_{\rm s,d}$ falls, driving ξ to higher values and increasing the propensity of disks to fragmentation.

There is a complication, however, which is that for sufficiently low metallicities, the disk becomes optically thin; therefore, further decreasing the metallicity would have the opposite effect. Even though core temperatures, and thus infall rates, continue to rise, disk temperatures should also rise. Thus, at some metallicity, disk fragmentation should level off. In fact, the observed solar-type close binary fraction in Figure 18 dramatically increases by a factor of ≈4 from [Fe/H] = +0.5 to −1.0 and then increases only by an additional ≈20% toward smaller metallicities, [Fe/H] < −1.0. We partially attribute this break to the metallicity at which disk fragmentation transitions from the optically thick ([Fe/H] $\gtrsim -1.0$) to optically thin ([Fe/H] $\lesssim -1.0$) regimes. We now present a simple model in which the combination of these effects can explain the rapid increase in the close binary fraction via disk fragmentation down to metallicities of $Z \sim 0.1\,Z_{\odot}$.

7.3. Limitations on Fragmentation as a Function of Metallicity

We construct a quantitative model for when disk fragmentation should occur at a range of metallicities for forming solar-mass stars. We can place limits on disk fragmentation by constructing self-consistent models for self-gravitating disks undergoing rapid infall. We begin with an expression for the disk midplane equilibrium temperature (see Kratter et al. 2008, 2010b),

$$\sigma T^4 = F_{\rm visc}\left(\frac{3\tau}{8} + \frac{1}{2\tau}\right) + F_{\rm irrad}, \tag{6}$$

where

$$F_{\rm visc} = \frac{3\dot{M}\Omega^2}{4\pi}, \tag{7}$$

$$F_{\rm irrad} = \sigma\left[\left(\frac{k_b}{G^3 M_* \mu}\right)^{1/7}\left(\frac{L_*}{4\pi}\right)^{2/7}\frac{1}{r^{3/7}}\right]^4, \tag{8}$$

$$L_* = \frac{1}{2}\frac{GM\dot{M}}{R_*}, \text{ and} \tag{9}$$

$$\tau = \frac{\kappa\Sigma}{2}. \tag{10}$$

We set L_* to be the accretion luminosity, which dominates over gravitational contraction during the earliest phases of star formation. In order to determine the opacities as a function of temperature, we fit a polynomial to the Semenov et al. (2003) opacities in the range of 10–400 K and adopt a constant value of $\kappa = 9.5\,{\rm cm^2\,g^{-1}}$ above >400 K for solar metallicity. We decrease the opacity $\kappa \propto Z$ in direct proportion to the

metallicity, as done in Bate (2014). Our results are only weakly dependent on the exact fit used for the opacities.

We do not expect magnetic fields to significantly affect the hydrodynamics of disk fragmentation. While the inner regions ($a \lesssim 1$ au) and surface layers of the disk tend to be ionized and well-coupled to the magnetic fields, the strongly self-gravitating parts across $a \approx 10$–100 au, which are subject to fragmentation, have large surface densities, low temperatures, and therefore predominantly neutral atoms. Tanaka & Omukai (2014) included an effective $\alpha = \alpha_{\rm GI} + \alpha_{\rm MRI}$ due to both gravitational and magnetorotational instabilities (MRIs) in their models and concluded that MRI negligibly affects their results. They argued for a relatively small $\alpha_{\rm MRI} = 0.01$, possibly even $\alpha_{\rm MRI} = 0$ in the "dead zone" of the disk where the ion density is too small to activate MRI. There are two competing effects as to whether $a_{\rm MRI}$ varies slightly with metallicity: while fewer metals will result in fewer ions and electrons, fewer metals will also reduce the dust content, which efficiently soaks up free electrons. In any case, $\alpha_{\rm GI} \approx 0.1$–$1$ is substantially larger in regions of the disk that are marginally stable or unstable, i.e., $Q \lesssim 1.4$ (Kratter et al. 2008, 2010a; Tanaka & Omukai 2014). Because the expected transport rates via MRI are small compared to gravitational instability, their inclusion shifts the fragmentation boundary only marginally.

We now proceed to solve Equation (6) under a series of constraints.

1. $Q = 1$. This ensures that the disk is susceptible to fragmentation.
2. $\dot{M} = 3\,\alpha c_{c,s}^3/(GQ)$, where $\alpha = 0.2$. We set the accretion rate through the disk to be consistent with the values expected for a strongly self-gravitating disk (Kratter et al. 2010a). Because disks are driven unstable by rapid infall with $\xi \geqslant 1$, we expect an unstable disk to process material at roughly this rate. This relationship is the standard viscous accretion rate expressed as a function of sound speed and Q.
3. $t_{\rm cool}\Omega \leqslant 7$. We require that the disk be able to radiate efficiently so that gravitational instability can lead to fragmentation, rather than gravitoturbulence or spiral mode saturation (Gammie 2001; Kratter & Lodato 2016). The cooling time indicates how long it takes a perturbation in temperature to radiatively cool from the midplane (Kratter et al. 2010b):

$$t_{\rm cool} = \frac{3\gamma\Sigma c_s^2}{32(\gamma-1)}\left(\tau + \frac{1}{\tau}\right)\sigma T^4. \quad (11)$$

We consider a solar-type protostar with mass $M_* = 0.75\,M_\odot$ and radius $R_* = 4\,R_\odot$. Equation (6) can therefore be written as a function of accretion rate, disk radius, and metallicity. We solve for the critical accretion rate $\dot{M}_{\rm crit}$ at which all of the above constraints are satisfied simultaneously for a wide range of disk radii $r_d = 10$–300 au and metallicities $-3.0 < \log(Z/Z_\odot) < 0.5$. We do not assume a scaling of the size of disks with metallicity and therefore leave it as a free parameter in our model. Because disks are most unstable at their outer edge, our models are described by a single number rather than a disk profile. This solution provides viable combinations of T, Σ, $\dot{M}$, Z, and r_d that could describe fragmenting disks. There is no guarantee of solutions for arbitrary combinations of temperature and metallicity. Moreover, the existence of a solution does not guarantee that real astrophysical disks will achieve such disk properties in a given environment.

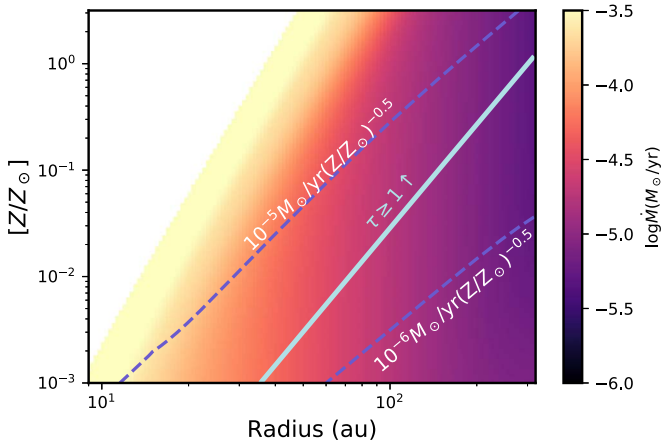

Figure 20. The color scale indicates the critical accretion rate, $\dot{M}_{\rm crit}$, required to drive a solar-type disk of a given radius and metallicity to fragment. In our model, fragmentation requires that the disk reach $Q = 1$ and $t_{\rm cool}\Omega < 7$, assuming that gravitational instability processes material at $\alpha \approx 0.2$. The white line indicates the point at which disks transition from optically thick to thin. The bottom dashed line indicates the expected mass-weighted average infall rate $\langle\dot{M}_{\rm in}\rangle$ as a function of metallicity from Tanaka & Omukai (2014), and the top dashed line represents a factor of 10 excursion higher due to stochastic variations. All disks achieve accretion rates of $\dot{M} = \langle\dot{M}_{\rm in}\rangle$, while only a small fraction reach $10\langle\dot{M}_{\rm in}\rangle$. Given a maximum disk size of $r_d \lesssim 300$ au, the propensity for disk fragmentation increases, especially at smaller separations, as the metallicity decreases.

In Figure 20, we show the critical mass accretion rates $\dot{M}_{\rm crit}$ that satisfy $Q = 1$ and $t_{\rm cool}\Omega \leqslant 7$ as a function of r_d and Z for our self-consistent models. We also demarcate the radius at which $Q = 1$ coincides with an optical depth of $\tau = 1$, which decreases from $r_d = 300$ au near $Z = Z_\odot$ to $r_d = 40$ au near $Z = 10^{-3}\,Z_\odot$. For solar metallicity, no solution exists below $r_d < 40$ au because the disks are too optically thick; therefore, the disk cooling timescale according to Equation (11) is longer than $t_{\rm cool} > 7/\Omega$. Meanwhile, metal-poor disks, in principle, can fragment at slightly smaller separations, but only down to $r_d \approx 10$ au at $Z = 10^{-3}\,Z_\odot$. The inability to directly fragment at small separations is consistent with previous studies that demonstrated that close binaries ($a < 10$ au) could not have formed in situ (Boss 1986; Bate 1998, 2009a). Instead, close binaries initially fragmented on larger scales and then migrated inward, probably via interactions with the disk and/or external companions (Artymowicz 1983; Artymowicz et al. 1991; Bate et al. 1995, 2002; Bate & Bonnell 1997; Moe & Kratter 2018).

To estimate the parameter space that disks might inhabit, we consider the expected infall rates from cores of different metallicities. Following Tanaka & Omukai (2014), we consider

$$\langle\dot{M}_{\rm in}\rangle = 10^{-6} M_\odot\ {\rm yr}^{-1}\left(\frac{Z}{Z_\odot}\right)^{-1/2}. \quad (12)$$

We display the combination of metallicities and disk radii that satisfy this mass accretion rate as the bottom dashed line in Figure 20. For solar-type stars with solar metallicity, an accretion rate of $10^{-6}\,M_\odot\,{\rm yr}^{-1}$ is consistent with the mass-weighted average accretion rate during the earliest phases of growth. However, the typical accretion rates are likely variable during the first $\approx$0.5 Myr, and thus most objects experience excursions above (or well above) $\langle\dot{M}_{\rm in}\rangle$ (Hartmann et al. 2001, 2016;

Evans et al. 2009; Offner & McKee 2011). Moreover, because accretion is likely stochastic, driven by nonuniform turbulent molecular clouds, not all solar-type stars of the same metallicity experienced the same accretion history (Nguyen et al. 2009; Cody et al. 2014; Bate 2018). An increase in infall to even a few times the average accretion rate can greatly increase the propensity for disk fragmentation. We therefore display the solution for $\dot{M}_{\rm crit} = 10\,\langle \dot{M}_{\rm in} \rangle$ as the top dashed line in Figure 20. Note that a very brief increase in the accretion rate above some threshold may not always trigger fragmentation, as the disk in some cases can quickly redistribute mass to remain stable.

According to Figure 20, it is quite difficult for metal-rich solar-type stars with $Z = 3\,Z_{\odot}$ to have formed close binaries via disk fragmentation. If such stars accrete constantly at their mass-weighted average rates and the sizes of their gaseous disks extend only to $r_d \approx 100$–300 au (Ansdell et al. 2018), then disk fragmentation would be impossible. Instead, the small fraction of metal-rich solar-type protostars that undergo significant stochastic excursions up to $\dot{M} \approx 20\langle \dot{M}_{\rm in} \rangle \approx 10^{-5}$ $M_{\odot}\,{\rm yr}^{-1}$ are capable of disk fragmentation. Even then, their disks are likely to fragment at large separations of $r_d \approx 200$ au. Meanwhile, disk fragmentation is much more probable with decreasing metallicity, especially at smaller separations. For $Z = 10^{-3}\,Z_{\odot}$, disks can fragment at $r_d \approx 60$ au, given their average infall rate of $\langle \dot{M}_{\rm in} \rangle$. If the disks accrete at $10\langle \dot{M}_{\rm in} \rangle$, then fragmentation can occur at separations as small as $r_d \approx 10$ au. The shift in the minimum allowed fragmentation radius with decreasing metallicity is consistent with the inward shift in the peak of the binary distribution; metal-poor binaries peak at separations of only $a_{\rm peak} \approx 10$ au, while metal-rich binaries peak at wide separations of $a_{\rm peak} \approx 200$ au (Figure 19). Although the location at which fragmentation occurs does not dictate the final binary period, correlations are to be expected (Moe & Kratter 2018).

Considering most disks will achieve at least a few times $\langle \dot{M}_{\rm in} \rangle$ at some time in their accretion history, the majority of solar-type stars with intermediate metallicity $Z = 10^{-1}\,Z_{\odot}$ should experience disk fragmentation. We therefore expect a rapid change in the probability of disk fragmentation across $-1.0 < [{\rm Fe/H}] < 0.5$, consistent with the observed factor of $\approx$4 change in the close binary fraction across this same metallicity interval. Below $[{\rm Fe/H}] < -1.0$, the observed flattening in the slope of the close binary fraction–versus–metallicity anticorrelation (Figure 18) is due to two effects. First, as the fraction of disks undergoing fragmentation increases, at some point nearly all disks experience fragmentation. According to Figure 20, essentially all disks with $\log(Z/Z_{\odot}) \approx -2.0$ will experience disk fragmentation. Further decreasing the metallicity can only slightly increase the close binary fraction. The universality of disk fragmentation at higher stellar masses, even at $Z_{\odot}$, may similarly explain the insensitivity of the close massive binary fraction to metallicity (see above).

Second, depending on the variation in disk size with metallicity, disk optical depth may also contribute to the slope change. Across the interval $-0.5 \lesssim \log(Z/Z_{\odot}) < 0.5$, fragmentation likely occurs in the optically thick regime (see Figure 20). Thus, decreasing the metallicity decreases the disk temperatures and cooling rates, which increases the probability of disk fragmentation. If disk sizes remain large across $-3 < \log(Z/Z_{\odot}) \lesssim -1.5$ (contrary to the models of Tanaka & Omukai 2014), fragmentation instead occurs in the optically thin regime, wherein the decline in disk metallicity tends to stabilize disks. Thus, one might expect this shift from optically thick to thin disks to temper the increase in binary formation.

The consistency between the period distribution of early-B stars and low-metallicity solar-type stars also supports a model in which enhanced disk fragmentation is responsible for the increase in close binaries (see Figure 19). Disk fragmentation is thought to become more prominent for higher masses due to the increased infall rates and correspondingly higher ξ associated with high-mass star formation (Kratter & Matzner 2006; Kratter et al. 2010a). We note that our models are substantially in agreement with those of Tanaka & Omukai (2014) in terms of the critical accretion rates $\dot{M}_{\rm crit}$ required to drive disks unstable. Our conclusions regarding the metallicity at which disk fragmentation occurs for solar-type binaries differ because we account for the expected stochastic excursions in infall rate above $\langle \dot{M}_{\rm in} \rangle$. These fluctuations are responsible for the instability across a wide range of metallicites in our model. There is now compelling observational evidence that disk fragmentation may occur for low-mass stars near solar metallicity (Tobin et al. 2016a), which boosts our confidence in this interpretation.

The increased probability for metal-poor disks to fragment must alter the IMF, at least to some extent. The IMF can actually describe three different parameters: (1) the total IMF, $f(M)$, of all stars, including all companions in multiple systems; (2) the primary star IMF, $f(M_1)$; and (3) the system IMF, $f(M_1{+}M_2{+}...{+}M_n)$. Chabrier (2003) and Kroupa et al. (2013) discussed the differences in these distributions, noting that the primary star IMF derives most directly from the observations. At least one, possibly all three, of these distributions change with metallicity. Nevertheless, the effect is relatively small. According to Figure 19, the solar-type binary fraction below $a < 100$ au is $\approx$90% for $[{\rm Fe/H}] = -3.0$ and $\approx$30% for $[{\rm Fe/H}] = +0.5$, a net change of $\approx$60%. The average mass ratio of solar-type binaries is $q \approx 0.5$, relatively independent of metallicity (Section 6). Hence, extremely metal-poor systems are, on average, $\approx$30% more massive than their metal-rich counterparts. Such a small change in the characteristic system mass is well within the observational measurement uncertainties and the resolution limit of simulations. We therefore do not expect the system IMF to vary significantly across $-1.5 \lesssim [{\rm Fe/H}] < 0.5$. The effect of a metallicity-dependent close binary fraction on the three different IMFs needs to be studied in more detail.

8. Conclusions

We have thoroughly examined the selection biases in various samples of solar-type stars and measured the intrinsic close binary fraction ($a < 10$ au) as a continuous function of metallicity. We investigated multiple samples of SBs (Section 3), APOGEE RV variables (Section 4), and *Kepler* EBs (Section 5), all of which exhibit the same anticorrelation between $F_{\rm close}$ and [Fe/H] (Section 6). We discussed and presented our own analytic models of fragmentation that reconcile the observed trends in binary properties as a function of mass, period, and metallicity (Section 7). We summarize the main results in the following.

SBs. Although the observed SB fraction appears to be constant with metallicity, metal-poor stars have weaker

absorption lines, making it more difficult to identify SBs (Figure 1). After correcting the Latham et al. (2002) sample of high proper motion FGK stars for incompleteness, the intrinsic close binary fraction decreases from $F_{\rm close} = 54\% \pm 12\%$ near $[{\rm m/H}] = -2.7$ to $F_{\rm close} = 17\% \pm 6\%$ at $[{\rm m/H}] = +0.5$ (Figure 3). Considering only the Carney–Latham SBs with $P = 20$–2000 days and $K_1 > 6\,{\rm km\,s^{-1}}$, where their survey is relatively complete (Figure 2), the SB fraction of metal-poor halo stars ($[{\rm m/H}] < -1.0$) is ≈1.9 times higher than that of metal-rich disk stars ($[{\rm m/H}] > -0.5$). Similarly, the observed SB companions to metal-poor giants ($-3.5 \lesssim [{\rm Fe/H}] \lesssim -1.5$) in the Carney et al. (2003) and Hansen et al. (2015, 2016a) samples are concentrated toward $K_1 > 7\,{\rm km\,s^{-1}}$ and $P = 35$–3000 days (Figure 4), implying that the bias-corrected close binary fraction of metal-poor solar-type dwarfs is $F_{\rm close} \approx 40\%$–$60\%$.

APOGEE RV variables. The APOGEE RV variability fraction of GK stars decreases by a factor of 4.0 ± 0.5 across $0.9 < [{\rm Fe/H}] < 0.5$ at the 22σ significance level (Figure 8), consistent with the conclusions of Badenes et al. (2018). We measure the same trend independent of spectral type, surface gravity, and RV threshold, indicating that both metal-poor and metal-rich binaries with $M_1 \approx 0.6$–$1.5\,M_\odot$ follow the same short-end tail of a lognormal period distribution. After correcting the APOGEE RV variability survey of GK IV/V stars for incompleteness, the intrinsic close binary fraction decreases from $F_{\rm close} = 41\% \pm 7\%$ at $[{\rm Fe/H}] = -0.8$ to $F_{\rm close} = 11\% \pm 2\%$ at $[{\rm Fe/H}] = +0.4$ (Figure 11). The median metallicities of close solar-type binaries are $\Delta[{\rm Fe/H}] = -0.13 \pm 0.03$ dex lower than those of single stars (Figure 9).

Kepler EBs. For a large sample of *Kepler* solar-type dwarfs in which the metallicities have been measured photometrically to $\delta[{\rm Fe/H}] \approx 0.3$ dex precision, the observed EB fraction decreases by a factor of 3.4 ± 0.5 across $-0.9 < [{\rm Fe/H}] < 0.3$ at the 9σ confidence level (Figure 14). For a smaller subsample in which the metallicities have been measured spectroscopically to $\delta[{\rm Fe/H}] \approx 0.1$ dex precision, the observed EB fraction also decreases by a factor of ≈3.5 across the narrower interval $-0.6 < [{\rm Fe/H}] < 0.4$ to 3σ significance. Metal-poor and metal-rich EBs both have the same period and eclipse depth distributions (Figure 15), implying that the period and mass-ratio distributions of close solar-type binaries are metallicity invariant. After accounting for various selection biases, the corrected solar-type close binary fraction decreases from $F_{\rm close} = 52\% \pm 14\%$ across $1.7 < [{\rm Fe/H}] < -1.1$ to $F_{\rm close} = 13\% \pm 3\%$ across $0.1 < [{\rm Fe/H}] < 0.5$ (Figure 17).

Combined observational constraints. After correcting for incompleteness, all five samples of solar-type stars exhibit a quantitatively consistent anticorrelation: $F_{\rm close} = 53\% \pm 12\%$, $40\% \pm 6\%$, $24\% \pm 4\%$, and $10\% \pm 3\%$ at $[{\rm Fe/H}] = -3.0$, -1.0, -0.2 (mean field metallicity), and $+0.5$, respectively (Figure 18). It is highly improbable that each of the different methods, with different biases, could conspire to produce consistent results. In contrast to close binaries, the wide binary fraction ($a \gtrsim 200$ au) of solar-type stars is relatively independent of metallicity. The close binary fraction of $M_1 \approx 10\,M_\odot$ primaries is quite high ($F_{\rm close} = 70\% \pm 11\%$) and does not vary significantly with metallicity. As solar-type stars decrease in metallicity to $[{\rm Fe/H}] \lesssim -1.0$, their close binary fraction ($F_{\rm close} \approx 50\%$), overall binary fraction ($F_{\rm binary} \approx 90\%$), triple-/quadruple-star fraction ($F_{\rm triple} + F_{\rm quadruple} \approx 35\%$), and companion period distribution ($a_{\rm peak} \approx 10$ au) all approach that of early-B stars (Figure 19).

Fragmentation models. Turbulent fragmentation of molecular cores on large spatial scales is relatively independent of metallicity, which is why the overall IMF and wide binary fraction are constant across $-1.5 \lesssim [{\rm Fe/H}] < 0.5$. Even at solar metallicity, the disks of massive protostars are highly unstable and prone to fragmentation, explaining the high close binary fraction of massive stars. Decreasing the metallicity of massive protostars can only marginally further increase the likelihood for disk fragmentation. For solar-type protostars with $\log(Z/Z_\odot) = 0.5$, only the small fraction of disks that attain stochastic excursions to accretion rates $\dot{M} \approx 20\langle\dot{M}_{\rm in}\rangle$ well above the mass-weighted average infall rates are capable of fragmentation at large radii of $r_d \approx 200$ au. With decreasing metallicity, (1) the expected infall rates from hotter cores increase, and (2) the temperatures of the optically thick disks decrease, which both simultaneously drive the disk toward instability. For solar-type protostars, the probability of disk fragmentation dramatically increases from $\log(Z/Z_\odot) = +0.5$ to -1.0, consistent with the observed increase in the close binary fraction. Metal-poor low-mass disks tend to fragment on smaller scales, possibly as small as $r_d = 10$ au, which is consistent with the observed shift in the peak of the overall solar-type binary period distribution.

Implications for binary evolution. Most solar-type stars with $[{\rm Fe/H}] < -1.0$ will interact with a close binary companion through either Roche-lobe overflow or wind accretion. This has important consequences for binary evolution in old and metal-poor environments such as the galactic halo, bulge, thick disk, globular clusters, dwarf galaxies, and high-redshift universe. Future studies must consider the effect of a close binary fraction–versus–metallicity anticorrelation on the inferred rates, properties, and progenitors of blue stragglers, barium stars, PNe, evolved giants, symbiotics, cataclysmic variables, novae, gravitational waves from binary WD mergers, and SNe Ia.

M.M. acknowledges financial support from NASA's Einstein Postdoctoral Fellowship program PF5-160139. K.M.K. acknowledges financial support from the National Science Foundation under grant No. AST-1410174 and NASA under grant Nos. ATP-140078 and ATP-170070. We thank Andrei Tokovinin and Kevin Schlaufman for enlightening discussions that helped motivate our analysis.

ORCID iDs

Kaitlin M. Kratter https://orcid.org/0000-0001-5253-1338
Carles Badenes https://orcid.org/0000-0003-3494-343X

References

Abt, H. A., Gomez, A. E., & Levy, S. G. 1990, ApJS, 74, 551
Abt, H. A., & Willmarth, D. W. 1987, ApJ, 318, 786
Adams, F. C., Ruden, S. P., & Shu, F. H. 1989, ApJ, 347, 959
Albareti, F. D., Allende Prieto, C., Almeida, A., et al. 2017, ApJS, 233, 25
Almeida, L. A., Sana, H., Taylor, W., et al. 2017, A&A, 598, A84
Ansdell, M., Williams, J. P., Trapman, L., et al. 2018, ApJ, 859, 21
Aoki, W., Suda, T., Beers, T. C., & Honda, S. 2015, AJ, 149, 39
Artymowicz, P. 1983, AcA, 33, 223
Artymowicz, P., Clarke, C. J., Lubow, S. H., & Pringle, J. E. 1991, ApJL, 370, L35
Badenes, C., Maoz, D., & Ciardullo, R. 2015, ApJL, 804, L25
Badenes, C., Mazzola, C., Thompson, T. A., et al. 2018, ApJ, 854, 147
Bastian, N., Covey, K. R., & Meyer, M. R. 2010, ARA&A, 48, 339
Bate, M. R. 1998, ApJL, 508, L95

Bate, M. R. 2005, MNRAS, 363, 363
Bate, M. R. 2009a, MNRAS, 392, 590
Bate, M. R. 2009b, MNRAS, 392, 1363
Bate, M. R. 2014, MNRAS, 442, 285
Bate, M. R. 2018, MNRAS, 475, 5618
Bate, M. R., & Bonnell, I. A. 1997, MNRAS, 285, 33
Bate, M. R., Bonnell, I. A., & Bromm, V. 2002, MNRAS, 336, 705
Bate, M. R., Bonnell, I. A., & Price, N. M. 1995, MNRAS, 277, 362
Beers, T. C., Norris, J. E., Placco, V. M., et al. 2014, ApJ, 794, 58
Belczynski, K., Kalogera, V., Rasio, F. A., et al. 2008, ApJS, 174, 223
Berger, T. A., Huber, D., Gaidos, E., & van Saders, J. L. 2018, ApJ, 866, 99
Bonnell, I. A. 1994, MNRAS, 269, 837
Boss, A. P. 1986, ApJS, 62, 519
Branch, D. 1976, ApJ, 210, 392
Brown, T. M., Latham, D. W., Everett, M. E., & Esquerdo, G. A. 2011, AJ, 142, 112
Carney, B. W. 1983, AJ, 88, 623
Carney, B. W., Aguilar, L. A., Latham, D. W., & Laird, J. B. 2005, AJ, 129, 1886
Carney, B. W., Latham, D. W., Laird, J. B., & Aguilar, L. A. 1994, AJ, 107, 2240
Carney, B. W., Latham, D. W., Stefanik, R. P., Laird, J. B., & Morse, J. A. 2003, AJ, 125, 293
Carollo, D., Beers, T. C., Chiba, M., et al. 2010, ApJ, 712, 692
Carrera, R., Gallart, C., Aparicio, A., & Hardy, E. 2011, AJ, 142, 61
Castelli, F., & Kurucz, R. L. 2004, arXiv:astro-ph/0405087
Chabrier, G. 2003, PASP, 115, 763
Chanamé, J., & Gould, A. 2004, ApJ, 601, 289
Chini, R., Fuhrmann, K., Barr, A., et al. 2014, MNRAS, 437, 879
Clark, B. M., Blake, C. H., & Knapp, G. R. 2012, ApJ, 744, 119
Clark, P. C., Glover, S. C. O., Klessen, R. S., & Bromm, V. 2011a, ApJ, 727, 110
Clark, P. C., Glover, S. C. O., Smith, R. J., et al. 2011b, Sci, 331, 1040
Cody, A. M., Stauffer, J., Baglin, A., et al. 2014, AJ, 147, 82
Cole, A. A., Tolstoy, E., Gallagher, J. S., III, & Smecker-Hane, T. A. 2005, AJ, 129, 1465
Connelley, M. S., Reipurth, B., & Tokunaga, A. T. 2008, AJ, 135, 2526
Da Rio, N., Gouliermis, D. A., & Henning, T. 2009, ApJ, 696, 528
De Cat, P., Fu, J. N., Ren, A. B., et al. 2015, ApJS, 220, 19
De Lucia, G., Tornatore, L., Frenk, C. S., et al. 2014, MNRAS, 445, 970
De Marchi, G., Paresce, F., & Portegies Zwart, S. 2010, ApJ, 718, 105
De Marco, O. 2009, PASP, 121, 316
De Marco, O., & Izzard, R. G. 2017, PASA, 34, e001
Dieterich, S. B., Henry, T. J., Golimowski, D. A., Krist, J. E., & Tanner, A. M. 2012, AJ, 144, 64
Dong, S., Zheng, Z., Zhu, Z., et al. 2014, ApJL, 789, L3
Dopcke, G., Glover, S. C. O., Clark, P. C., & Klessen, R. S. 2011, ApJL, 729, L3
Dopcke, G., Glover, S. C. O., Clark, P. C., & Klessen, R. S. 2013, ApJ, 766, 103
Dotter, A., Chaboyer, B., Jevremović, D., et al. 2008, ApJS, 178, 89
Duchêne, G., Bontemps, S., Bouvier, J., et al. 2007, A&A, 476, 229
Duchêne, G., & Kraus, A. 2013, ARA&A, 51, 269
Duchêne, G., Lacour, S., Moraux, E., Goodwin, S., & Bouvier, J. 2018, MNRAS, 478, 1825
Duchêne, G., Simon, T., Eislöffel, J., & Bouvier, J. 2001, A&A, 379, 147
Dunstall, P. R., Dufton, P. L., Sana, H., et al. 2015, A&A, 580, A93
Duquennoy, A., & Mayor, M. 1991, A&A, 248, 485
Eggleton, P. 2006, Evolutionary Processes in Binary and Multiple Stars (Cambridge: Cambridge Univ. Press)
Eggleton, P. P. 1983, ApJ, 268, 368
El-Badry, K., & Rix, H.-W. 2019, MNRAS, 482, L139
El-Badry, K., Ting, Y.-S., Rix, H.-W., et al. 2018, MNRAS, 476, 528
Evans, N. R., Berdnikov, L., Lauer, J., et al. 2015, AJ, 150, 13
Evans, N. J., II, Dunham, M. M., Jørgensen, J. K., et al. 2009, ApJS, 181, 321
Fischer, D. A., & Marcy, G. W. 1992, ApJ, 396, 178
Fischer, D. A., & Valenti, J. 2005, ApJ, 622, 1102
Fisher, R. T. 2004, ApJ, 600, 769
Frasca, A., Molenda-Żakowicz, J., De Cat, P., et al. 2016, A&A, 594, A39
Gammie, C. F. 2001, ApJ, 553, 174
Gao, S., Liu, C., Zhang, X., et al. 2014, ApJL, 788, L37
Gao, S., Zhao, H., Yang, H., & Gao, R. 2017, MNRAS, 469, L68
García Pérez, A. E., Ness, M., Robin, A. C., et al. 2018, ApJ, 852, 91
Geha, M., Brown, T. M., Tumlinson, J., et al. 2013, ApJ, 771, 29
Geller, A. M., & Mathieu, R. D. 2012, AJ, 144, 54
Ghez, A. M., Neugebauer, G., & Matthews, K. 1993, AJ, 106, 2005
Glover, S. C. O., & Clark, P. C. 2012, MNRAS, 426, 377
Goldberg, D., Mazeh, T., Latham, D. W., et al. 2002, AJ, 124, 1132
Governato, F., Willman, B., Mayer, L., et al. 2007, MNRAS, 374, 1479
Grether, D., & Lineweaver, C. H. 2007, ApJ, 669, 1220
Hansen, T. T., Andersen, J., Nordström, B., et al. 2015, A&A, 583, A49
Hansen, T. T., Andersen, J., Nordström, B., et al. 2016a, A&A, 586, A160
Hansen, T. T., Andersen, J., Nordström, B., et al. 2016b, A&A, 588, A3
Hartmann, L., Ballesteros-Paredes, J., & Bergin, E. A. 2001, ApJ, 562, 852
Hartmann, L., Herczeg, G., & Calvet, N. 2016, ARA&A, 54, 135
Heggie, D. C. 1975, MNRAS, 173, 729
Hekker, S., Snellen, I. A. G., Aerts, C., et al. 2008, A&A, 480, 215
Hettinger, T., Badenes, C., Strader, J., Bickerton, S. J., & Beers, T. C. 2015, ApJL, 806, L2
Holtzman, J. A., Shetrone, M., Johnson, J. A., et al. 2015, AJ, 150, 148
Huber, D., Silva Aguirre, V., Matthews, J. M., et al. 2014, ApJS, 211, 2
Hurley, J. R., Tout, C. A., & Pols, O. R. 2002, MNRAS, 329, 897
Ivanova, N., Belczynski, K., Fregeau, J. M., & Rasio, F. A. 2005, MNRAS, 358, 572
Janson, M., Hormuth, F., Bergfors, C., et al. 2012, ApJ, 754, 44
Jao, W.-C., Mason, B. D., Hartkopf, W. I., Henry, T. J., & Ramos, S. N. 2009, AJ, 137, 3800
Jones, D., & Boffin, H. M. J. 2017, NatAs, 1, 0117
Jorissen, A., Van Eck, S., Mayor, M., & Udry, S. 1998, A&A, 332, 877
Kirk, B., Conroy, K., Prša, A., et al. 2016, AJ, 151, 68
Kobulnicky, H. A., Kiminki, D. C., Lundquist, M. J., et al. 2014, ApJS, 213, 34
Kratter, K., & Lodato, G. 2016, ARA&A, 54, 271
Kratter, K. M., & Matzner, C. D. 2006, MNRAS, 373, 1563
Kratter, K. M., Matzner, C. D., & Krumholz, M. R. 2008, ApJ, 681, 375
Kratter, K. M., Matzner, C. D., Krumholz, M. R., & Klein, R. I. 2010a, ApJ, 708, 1585
Kratter, K. M., & Murray-Clay, R. A. 2011, ApJ, 740, 1
Kratter, K. M., Murray-Clay, R. A., & Youdin, A. N. 2010b, ApJ, 710, 1375
Kraus, A. L., Ireland, M. J., Martinache, F., & Hillenbrand, L. A. 2011, ApJ, 731, 8
Kraus, A. L., Ireland, M. J., Martinache, F., & Lloyd, J. P. 2008, ApJ, 679, 762
Kroupa, P., Weidner, C., Pflamm-Altenburg, J., et al. 2013, The Stellar and Sub-Stellar Initial Mass Function of Simple and Composite Populations (Dordrecht: Springer Science+Business Media), 115
Krumholz, M. R., Klein, R. I., & McKee, C. F. 2007, ApJ, 665, 478
Laird, J. B., Carney, B. W., & Latham, D. W. 1988, AJ, 95, 1843
Larson, R. B. 1969, MNRAS, 145, 271
Latham, D. W., Stefanik, R. P., Torres, G., et al. 2002, AJ, 124, 1144
Leiner, E. M., Mathieu, R. D., Gosnell, N. M., & Geller, A. M. 2015, AJ, 150, 10
Levato, H., Malaroda, S., Morrell, N., & Solivella, G. 1987, ApJS, 64, 487
Lodieu, N., Zapatero Osorio, M. R., & Martín, E. L. 2009, A&A, 499, 729
Lucatello, S., Tsangarides, S., Beers, T. C., et al. 2005, ApJ, 625, 825
Machida, M. N. 2008, ApJL, 682, L1
Machida, M. N., Omukai, K., Matsumoto, T., & Inutsuka, S.-I. 2009, MNRAS, 399, 1255
Mackereth, J. T., Bovy, J., Schiavon, R. P., et al. 2017, MNRAS, 471, 3057
Marks, M., Kroupa, P., Dabringhausen, J., & Pawlowski, M. S. 2012, MNRAS, 422, 2246
Mathieu, R. D. 1994, ARA&A, 32, 465
Mathieu, R. D., & Geller, A. M. 2009, Natur, 462, 1032
Mathur, S., Huber, D., Batalha, N. M., et al. 2017, ApJS, 229, 30
Meibom, S., & Mathieu, R. D. 2005, ApJ, 620, 970
Melo, C. H. F. 2003, A&A, 410, 269
Moe, M., & De Marco, O. 2006, ApJ, 650, 916
Moe, M., & Di Stefano, R. 2013, ApJ, 778, 95
Moe, M., & Di Stefano, R. 2015, ApJ, 810, 61
Moe, M., & Di Stefano, R. 2017, ApJS, 230, 15
Moe, M., & Kratter, K. M. 2018, ApJ, 854, 44
Mulders, G. D., Pascucci, I., Apai, D., Frasca, A., & Molenda-Żakowicz, J. 2016, AJ, 152, 187
Murphy, S. J., Moe, M., Kurtz, D. W., et al. 2018, MNRAS, 474, 4322
Myers, A. T., Krumholz, M. R., Klein, R. I., & McKee, C. F. 2011, ApJ, 735, 49
Ness, M., & Freeman, K. 2016, PASA, 33, e022
Nguyen, D. C., Scholz, A., van Kerkwijk, M. H., Jayawardhana, R., & Brandeker, A. 2009, ApJL, 694, L153
Nidever, D. L., Holtzman, J. A., Allende Prieto, C., et al. 2015, AJ, 150, 173
Offner, S. S. R., Kratter, K. M., Matzner, C. D., Krumholz, M. R., & Klein, R. I. 2010, ApJ, 725, 1485

Offner, S. S. R., & McKee, C. F. 2011, ApJ, 736, 53
Olszewski, E. W., Schommer, R. A., Suntzeff, N. B., & Harris, H. C. 1991, AJ, 101, 515
Owen, J. E., & Murray-Clay, R. 2018, MNRAS, 480, 2206
Pagel, B. E. J., & Tautvaisiene, G. 1998, MNRAS, 299, 535
Peter, D., Feldt, M., Henning, T., & Hormuth, F. 2012, A&A, 538, A74
Petigura, E. A., Marcy, G. W., Winn, J. N., et al. 2018, AJ, 155, 89
Piatti, A. E., & Geisler, D. 2013, AJ, 145, 17
Prieur, J. L., Aristidi, E., Lopez, B., et al. 2002, ApJS, 139, 249
Prša, A., Batalha, N., Slawson, R. W., et al. 2011, AJ, 141, 83
Raghavan, D., McAlister, H. A., Henry, T. J., et al. 2010, ApJS, 190, 1
Rastegaev, D. A. 2010, AJ, 140, 2013
Ratnatunga, K. U., & Yoss, K. M. 1991, ApJ, 377, 442
Ren, A., Fu, J., De Cat, P., et al. 2016, ApJS, 225, 28
Riaz, B., Gizis, J. E., & Samaddar, D. 2008, ApJ, 672, 1153
Rizzuto, A. C., Ireland, M. J., Robertson, J. G., et al. 2013, MNRAS, 436, 1694
Ruchti, G. R., Fulbright, J. P., Wyse, R. F. G., et al. 2011, ApJ, 737, 9
Ryan, S. G. 1992, AJ, 104, 1144
Sana, H., de Mink, S. E., de Koter, A., et al. 2012, Sci, 337, 444
Sana, H., Le Bouquin, J.-B., Lacour, S., et al. 2014, ApJS, 215, 15
Schlafly, E. F., & Finkbeiner, D. P. 2011, ApJ, 737, 103
Schmalzl, M., Gouliermis, D. A., Dolphin, A. E., & Henning, T. 2008, ApJ, 681, 290
Semenov, D., Henning, T., Helling, C., Ilgner, M., & Sedlmayr, E. 2003, A&A, 410, 611
Shatsky, N., & Tokovinin, A. 2002, A&A, 382, 92
Shporer, A., Fuller, J., Isaacson, H., et al. 2016, ApJ, 829, 34
Shu, F. H. 1977, ApJ, 214, 488
Sirianni, M., Nota, A., De Marchi, G., Leitherer, C., & Clampin, M. 2002, ApJ, 579, 275
Sokoloski, J. L., & Bildsten, L. 2010, ApJ, 723, 1188
Stryker, L. L., Hesser, J. E., Hill, G., Garlick, G. S., & Okeefe, L. M. 1985, PASP, 97, 247
Tanaka, K. E. I., & Omukai, K. 2014, MNRAS, 439, 1884
Thompson, S. E., Everett, M., Mullally, F., et al. 2012, ApJ, 753, 86
Tian, Z., Liu, X., Yuan, H., et al. 2018, RAA, 18, 52
Tobin, J. J., Kratter, K. M., Persson, M. V., et al. 2016a, Natur, 538, 483
Tobin, J. J., Looney, L. W., Li, Z.-Y., et al. 2016b, ApJ, 818, 73
Tokovinin, A. 2014, AJ, 147, 87
Tokovinin, A., Thomas, S., Sterzik, M., & Udry, S. 2006, A&A, 450, 681
Tokovinin, A. A. 2000, A&A, 360, 997
Van der Swaelmen, M., Boffin, H. M. J., Jorissen, A., & Van Eck, S. 2017, A&A, 597, A68
von Hippel, T., Gilmore, G., Tanvir, N., Robinson, D., & Jones, D. H. P. 1996, AJ, 112, 192
Yasui, C., Kobayashi, N., Saito, M., & Izumi, N. 2016a, AJ, 151, 115
Yasui, C., Kobayashi, N., Tokunaga, A. T., Saito, M., & Izumi, N. 2016b, AJ, 151, 50
Yuan, H., Liu, X., Xiang, M., et al. 2015, ApJ, 799, 135
Zapatero Osorio, M. R., & Martín, E. L. 2004, A&A, 419, 167
Zasowski, G., Johnson, J. A., Frinchaboy, P. M., et al. 2013, AJ, 146, 81
Ziegler, C., Law, N. M., Baranec, C., Riddle, R. L., & Fuchs, J. T. 2015, ApJ, 804, 30